Doctoral Thesis

Wireless Power Transfer System for Battery-Less Body Implantable Devices

Hyunggun Ma

Department of Electrical Engineering

Graduate School of UNIST

2019

Wireless Power Transfer System for Battery-Less Body Implantable Devices

Hyunggun Ma

Department of Electrical Engineering
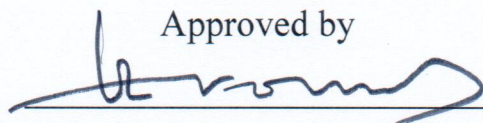
Graduate School of UNIST

Wireless Power Transfer System for

Battery-Less Body Implantable Devices

A thesis/dissertation

submitted to the Graduate School of UNIST

in partial fulfillment of the

requirements for the degree of

Doctor of Philosophy

Hyunggun Ma

12/12/2018

Approved by

_____

Advisor

Franklin Bien

Wireless Power Transfer System for
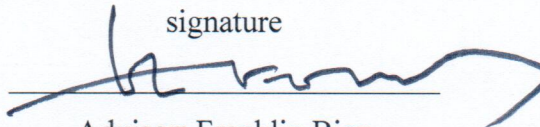
Battery-Less Body Implantable Devices

Hyunggun Ma

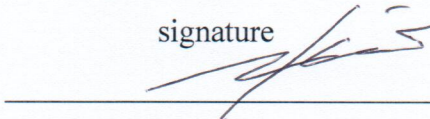This certifies that the thesis/dissertation of Hyunggun Ma is approved.
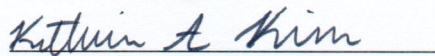
12/12/2018
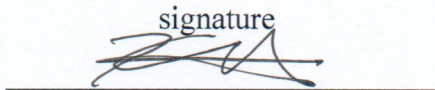
signature

Advisor: Franklin Bien

signature
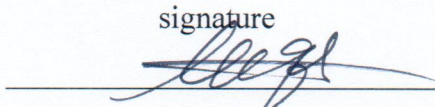
Jaehyouk Choi: Thesis Committee Member #1

signature

Katherine A. Kim: Thesis Committee Member #2

signature

Kyuho Lee: Thesis Committee Member #3

signature

Ockgoo Lee: Thesis Committee Member #4;

Abstract

As the life expectancy is increased and the welfare is promoted, researches on the body implantable medical devices (BIMD) are actively being carried out, and products providing more various functions are being released. On the other hand, due to these various functions, the power consumption of the BIMD is also increased, so that the primary battery alone cannot provide sufficient power for the devices. The limited capacity and life time of batteries force patients to make an additional payment and suffering for the power supply of the BIMD.

Wireless power transfer technology is the technology which has been making remarkable progress mainly in wireless charging for personal portable devices and electric vehicles. Convergence of wireless power transfer technology (WPT) and rechargeable battery can extend the life time of the BIMD and reduce the suffering and the cost for battery replacements. Furthermore, WPT enables the devices which do not need to operate consistently such as body implantable sensor devices to be used without batteries. In this dissertation, techniques to support WPT for BIMD are introduced and proposed.

First, basic researches on magnetic coupled WPT are presented. The basics which are important factors to analyze power transmission are introduced. In addition, circuits that make up the WPT system are described. There are three common technical challenges in WPT. Those are efficiency degradation on coil geometry, voltage gain variation with coil geometry, and power losses in WPT. The common challenges are discussed in chapter II. Moreover, additional challenges which are arisen in WPT for BIMD and approaches to resolve the challenges are addressed in chapter II.

Then, efficiency improvement techniques and control techniques in WPT are presented in chapter III. The presented techniques to improve efficiency are applied in coil parts and circuit parts. In coil parts, efficiency enhancement technique by geometric variation is proposed. In circuit parts, instantaneous power consuming technique for step-down converter is suggested. Li-ion battery charger is also discussed in chapter III. Additionally, the wireless controlled constant current / constant voltage charging mode and the proposed step charging method are described.

After that, WPT system for BIMD is discussed one by one with the proposed techniques for each part in chapter IV. A load transformation is suggested to improve efficiency in weak coupling, and suppress voltage gain variation under coil displacement. Power conversion efficiency improvement techniques for rectifier and converter are also proposed. By using the proposed technique for the converter, we can remove the bootstrap capacitors, and reduce the overall size of power circuits.

In conclusion, techniques in coil parts and circuit parts to handle challenges in WPT for BIMD are fully investigated in this thesis in addition to the efficiency improvement and control techniques in common WPT. All the techniques are verified through simulations or experiments. The approaches realized in the thesis can be applied to other applications employing the WPT.

Contents

List of figures

List of tables

Nomenclature

BIMD	Body Implantable Medical Device
WPT	Wireless Power Transfer
PWM	Pulse-Width-Modulation
MOSFET	Metal-oxide-semiconductor Field-effect-transistor
CC	Constant Current
CV	Constant Voltage
SAR	Specific Absorption Rate
IEEE	Institute of Electrical and Electronics Engineers
MPE	Maximum Permissible Exposure
BR	Basic SAR Restriction
IC	Integrated Circuit
WBAN	Wireless Body Area Network
GI	Gastrointestinal
LED	Light Emitting Diode
MR-WPT	Magnetic Resonance Wireless Power Transfer
ADS	Advanced Design System
HFSS	High Frequency Structure Simulator
ISM	Industrial, Scientific, and Medical
EM	Electro Magnetic
IPT	Inductive Power Transfer
FM	Frequency Modulation
SS	Series-series
SP	Series-parallel
PP	Parallel-parallel
PS	Parallel-series
ZPA	Zero Phase Angle
MCU	Micro Controller Unit
DSP	Digital Signal Processor
DCM	Discontinuous Mode
PCE	Power Conversion Efficiency
ZVS	Zero Voltage Switching
VCR	Voltage Conversion Ratio
PVT	Process, Voltage, and Temperature
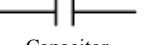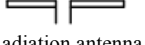
SBAOG	Sampling-based adaptive offset generator
EA	Error Amplifier
PFM	Pulse Frequency Modulation
MPC	Momentary Power Consuming
DOCC	Dead-time-based Off-time Calibration Circuit
COT	Constant-on-time
VOT	Variable-on-time
CCLS	Capacitively Coupled Level Shifter
DTDC	Dead-time to DC converter
PFD	Phase Frequency Detector

Chapter I

Introduction

Wireless power transfer (WPT) is a technology that is widely known to the public by making remarkable progress mainly in wireless charging for personal portable devices and wireless charging of electric vehicles. WPT transfers electrical energy to a load wirelessly. This technology converts electrical energy into electromagnetic waves to transfer energy. Depending on the characteristics of the energy to be transmitted, it is divided into electric field type, magnetic field type, and electromagnetic wave type. Comparison of characteristics of each WPT is shown in Table 1.1. Electric filed type basically uses capacitive coupling phenomenon for energy transfer. The energy is transferred in voltage. Magnetic field type uses electromagnetic induction phenomenon for energy transfer. Theory of magnetic WPT is based on Faraday's law of electromagnetic induction. The energy is transferred in current. Mechanism of electromagnetic field type is identical to wireless data communication but different in radiated power. To meet the demanded power at the receiver, increased power is radiated than wireless data communication. The energy is transferred in power. Among the three types, the magnetic field type is widely used because the magnetic field is less harmful to human than the electric field and energy transfer efficiency is the best in moderate distance.

Table 1.1. Comparison of characteristics of wireless power transfer technologies

	Electric field		Magnetic field		Electromagnetic field
	Coupling	Resonance	Induction	Resonance	Radiation
	Capacitive coupling	Electric resonance	Electromagnetic induction	Magnetic resonance	Radiation antenna
Feature	• Short distance • Low frequency~ High Frequency	• Middle distance • High frequency • Thin & Light	• Short distance • Low frequency	• Middle distance • Low frequency~ High frequency	• Long distance • Ultra high frequency
Component	Capacitor		Inductor		Radiation antenna
Energy Source	Voltage		Current		Power
Power Transmission	$P_E = \frac{1}{2} C_m V^2 f$		$P_M = \frac{1}{2} L_m I^2 f$		$P_R = \left(\frac{\lambda}{4\pi l}\right)^2 G_T G_R P_T$
Field	Electrostatic field (Divergent field)		Induction field (Rotation field)		Radiation field
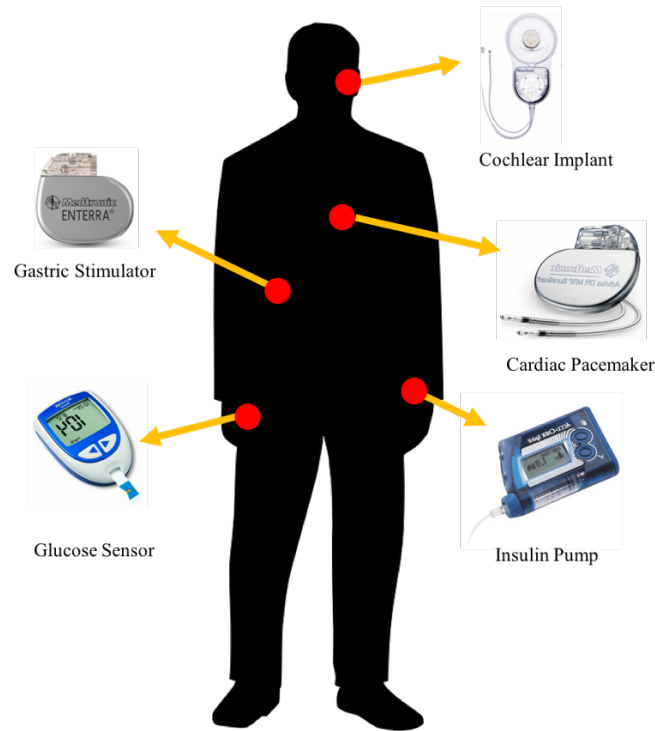
Fig.1.1 Example of body implantable medical device applications.

As the population is aging, and the interest of health is increasing, researches on body implantable medical device (BIMD) are going along, actively. A representative device in BIMD is cardiac pacemaker [1.1]. The body-implantable system such as cardiac pacemaker uses the primary battery as power supply. As the device evolves, more functions are provided, which increases the power consumption of the device. The battery need to be replaced in case of low battery charged capacity. Since surgery should be done for replacing the battery, a large capacity battery is employed to reduce frequency of surgery. However, large volume of battery is hard to implant in body because of limited space. So that the primary battery alone cannot supply enough power and the limited lifetime will incur additional costs and suffering for the battery replacement. Therefore, a sustainable power supply via WPT is required to resolve the problem with BIMD's primary battery. Fig. 1.1 shows BIMD where WPT can be applied.

Chapter II

Basic Research on Magnetically Coupled Wireless Power Transfer

2.1 Principle
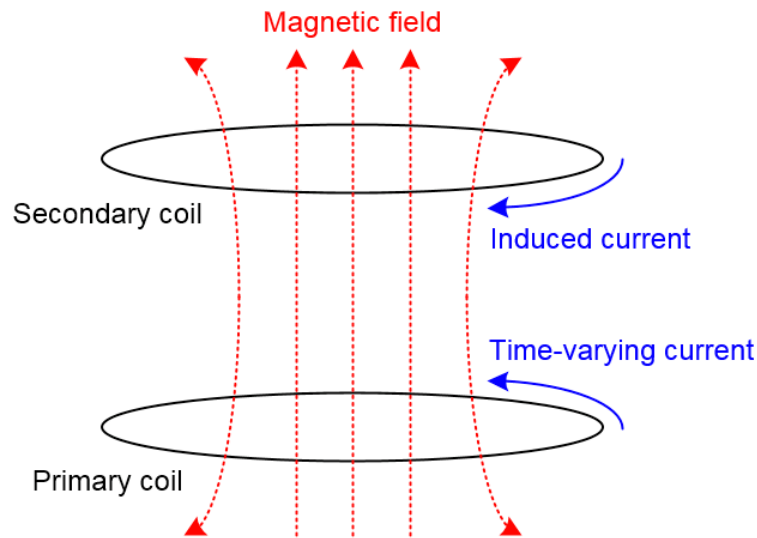
Fig.2.1 Concept of magnetic coupled wireless power transfer.

The basic principle of WPT is the 'electromagnetic induction' phenomenon discovered by British physicist Faraday in the 19th century. The time-varying magnetic field around the wire induces a current in the wire. The voltage of the induced current is proportional to the magnitude of the change in the magnetic field. The Faraday's law of induction is defined as

$$\nabla \times E = -\frac{\partial B}{\partial t} \tag{2.1}$$

where $\nabla \times$ is curl operator, E is electric field (in V/m), and B is magnetic flux density (in T). It is also known as 3rd law of Maxwell's equation. The Faraday's law of induction only mentions magnitude of the induced current. The negative sign in Faraday's law was referred by Lenz's law. According to Lenz's law, the induced electromotive force generated in the electric circuit is generated in a direction that hinders the change of the magnetic flux passing through the closed circuit. The Faraday's law is related to power reception.

For power transmission, Ampère's circuital law is applied to give explanation. French physicist André-Marie Ampère discovered it incompletely, and James Clerk Maxwell revised it to the present form. Ampère's circuital law is defined as

$$\nabla \times H = J + \frac{\partial D}{\partial t} \tag{2.2}$$

where H is magnetic field strength (in A/m), J is current density (in A/m^2), and D is displacement current. The induced magnetic field around the closed loop is proportional to the current density plus the time-varying current.

The magnetic coupled WPT is based on the Faraday's law of induction and Ampère's law. The time-varying current in primary coil induces magnetic field and the time-varying magnetic field induces current which turns into electromotive force in secondary coil.

2.2 Parameters

2.2.1 Quality factor

The quality factor (Q factor) is a parameter that characterizes the relationship between center frequency to the bandwidth of resonator. It also describes the rate of energy use relative to stored energy, which also means efficiency. High Q factor in WPT involves that the power can be transferred efficiently than low Q factor system. Therefore, Q factor is a representative parameter of WPT coils. The Q factor is defined as

$$Q_s = \frac{1}{R}\sqrt{\frac{L}{C}} = \frac{R}{\omega L} = \frac{1}{\omega RC} \qquad \text{(series)} \qquad (2.3)$$

$$Q_p = R\sqrt{\frac{C}{L}} = \frac{\omega L}{R} = \omega RC \qquad \text{(parallel)} \qquad (2.4)$$

where Q is quality factor, L is inductance, C is capacitance, R is resistance, and ω is angular frequency. From (1.1) and (1.2), Q factor is dependent on load resistance. Therefore, in order to have a high Q factor, the RLC structure should be determined according to the value of the load resistance. Fig.2.1 shows characteristic of quality factor between frequency and average power dissipation. It illustrates that high Q factor system can transfer higher power than low Q factor. Therefore, low Q is used in short distance applications such as charger for personal portable devices, and high Q is used in long distance applications such as wireless charger of electric vehicles and BIMD.
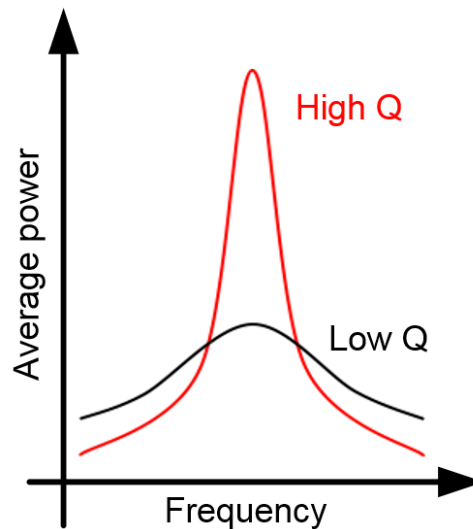
Fig.2.2 Characteristics of quality factor: frequency vs. average power dissipation.

2.2.2 Coupling coefficient and mutual inductance

The coupling coefficient, k, is a parameter expressing how much the magnetic field generated in one coil affects the other coils. Alternatively, it is a parameter that determines how well the two coils are coupled to the magnetic field. The coupling coefficient is described from '0' to '1', where '0' is the magnetic field of the primary coil that has no effect on the secondary coil. In other words, it can be seen that the two coils are isolated and not linked by a magnetic field. Coupling coefficient '1' can be seen that the magnetic field of the primary coil is completely linked to the secondary coil. For some data, the coupling coefficient is expressed as -1 <k <1, where the negative value involves the opposite direction of the induced current [2.1] or the opposite direction of the coil winding [2.2]. The coupling coefficient is expressed as

$$k = \frac{M}{\sqrt{L_p L_s}} \tag{2.5}$$

where L_p is the inductance of the primary coil, L_s is the inductance of the secondary coil, and M is the mutual inductance.

Mutual inductance is the degree to which inductors in different circuits are affected by the induced magnetic field. When the current on primary side varies, the induced current is generated on primary side by the induced magnetic field at the secondary side. At this time, mutual inductance is the relationship between original energy and induced energy. The equation for mutual inductance is normally expressed with magnetic flux. In [2.3], the mutual inductance is expressed with geometric term to give simple understanding with WPT coil. The mutual inductance is expressed as

$$M = \frac{\mu_0 \pi r_p^2 r_s^2}{2(r_p^2 + Z^2)^{\frac{3}{2}}} \tag{2.6}$$

where μ_0 is permeability, r_p is radius of primary coil, r_s is radius of secondary coil, and Z is distance between primary coil and secondary coil in Fig.2.3.
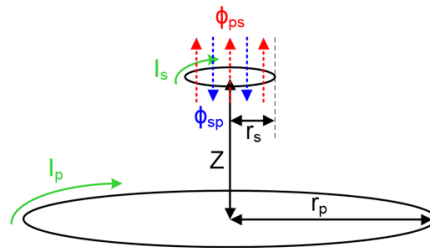
Fig.2.3 Simple WPT coil with electrical and geometric factors.

2.3 Types of magnetically coupled WPT

2.3.1 Magnetic inductive

The magnetic inductive method transfers the power with induced magnetic field. A current which flows through transmitting coil induces magnetic field. The induced magnetic field penetrates receiver coil. The penetrating magnetic field induces current to supply power to the load. This phenomenon is almost same as transformer. The principle of magnetic inductive method is followed by faraday's law of electromagnetic induction. The inductive method uses wide frequency range for power transfer. It uses from 100 kHz to 205 kHz. To cover wide frequency range, the antenna coil is made differently than ordinary antenna. The ordinary antenna has high quality factor to enhance frequency selection quality. However, the antenna for magnetic inductive WPT has low quality factor. Since the antenna for magnetic inductive has low quality factor, distance of power transfer is proportional to size of the antenna. The magnetic inductive aims to support device within several watts. It aims to transfers power no more than distance of centimeters.

2.3.2 Magnetic resonance

The principle of power transfer for magnetic resonant method is same as magnetic inductive method. The mechanism of magnetic resonant method is different from magnetic inductive method. It exploits resonance mode to transfer power. Assume transmitter and receiver antenna are identically designed. When transmitters transfers power in resonance frequency, the transmitter and receiver coil enters resonance mode. In resonance mode, the impedance of each coil is minimized, and the power is easily transferred. The quality factor in resonant system is effect of electrical resistance. Therefore, the antenna for magnetic resonant method has very high quality factor to make extremely low electrical resistance at resonance frequency. The magnetic resonant method uses specific frequency such as 6.78 MHz, and 13.56 MHz. At other frequency, transmitting power efficiency is considerably low. The magnetic resonant aims to support device within tens of watts. It aims to transfer power within several meters.

2.4 Circuit description

2.4.1 Overall system architecture of wireless power transfer

The wireless power transfer is performed by employing induced magnetic field. The magnetic inductive, and the magnetic resonant method is differentiated by power transferring principle. If the power is transferred by penetrated magnetic field, the method is called magnetic inductive. If the power is transferred by resonated magnetic field, the method is called magnetic resonant. According to the principle of power transfer, transfer power, distance, and frequency are determined. However, even though the principle is different, the fundamental operating scheme is identical.

Both types of wireless power transfer method have same operating scheme as transformer. The wireless power transfer system is composed of transmitter driver, transmitter coil, receiver coil, rectifier, DC-DC converter, linear regulator, and the load. A transmitter driver generates AC signal to induce magnetic field from transmitter coil. The induced magnetic field induces current at receiver coil. And the transferred AC power is converted into DC power by a rectifier. After the rectifier, DC-DC converter is needed to converted DC power into the level of desired DC power. Lastly, a linear regulator is used to regulate DC voltage in any circumstances. The regulated DC voltage supplies power to an electronic system such as sensor interface. In Fig.2.4, overall system architecture of wireless power transfer is shown.
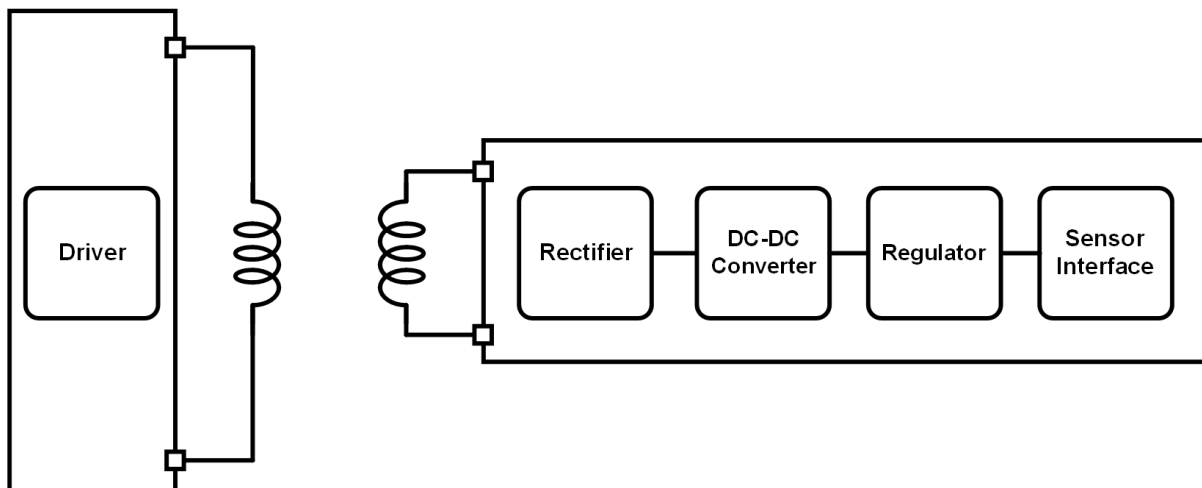
Fig.2.4. System architecture of wireless power transfer.

2.4.2 Transmitting coil driver

To transfer power wirelessly, AC power generator is essential. A single phase inverter is commonly used in wireless power transfer system. There are two types of inverter in the single phase inverter which are half-bridge inverter, and full-bridge inverter.

Fig.2.5 shows a circuit diagram of half-bridge inverter. The half-bridge inverter is used in low power application [2.4]. It is made up with two power transistors as switches, two diodes, and pulse-width-modulation (PWM) driver. If metal-oxide-semiconductor field-effect-transistor (MOSFET) is used for power transistor, an intrinsic body diode is used for anti-parallel diode. The PWM driver generates complementary pulse signal to control M_1, and M_2. By controlling M_1, and M_2, DC power is converted into AC power. If the driver drives resistive load, phase of voltage and current is identical. The parallel diodes do not have any role with resistive load. In inductive loads, there are phase difference between voltage, and current. Sometimes, reverse current is conducted through the parallel diode, because of the characteristic of inductive loads.

Fig.2.6 shows the operation state of half-bridge inverter with inductive load. High-side switch is turned on in Fig.2.6 (a). In this phase, current from power source conducts from the source to the load. When high-side switch is turned off, the current flows through parallel diode of low-side switch, which is shown in Fig.2.6 (b). The current flows in reverse when low-side switch is turned on, and after low-side switch is turned off, which is shown in Fig.2.6 (c), and (d), respectively.
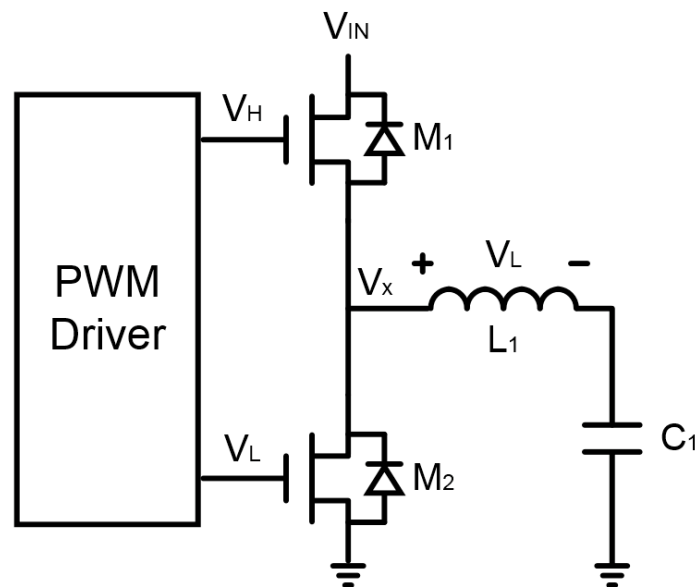
Fig.2.5. Circuit diagram of half-bridge inverter.
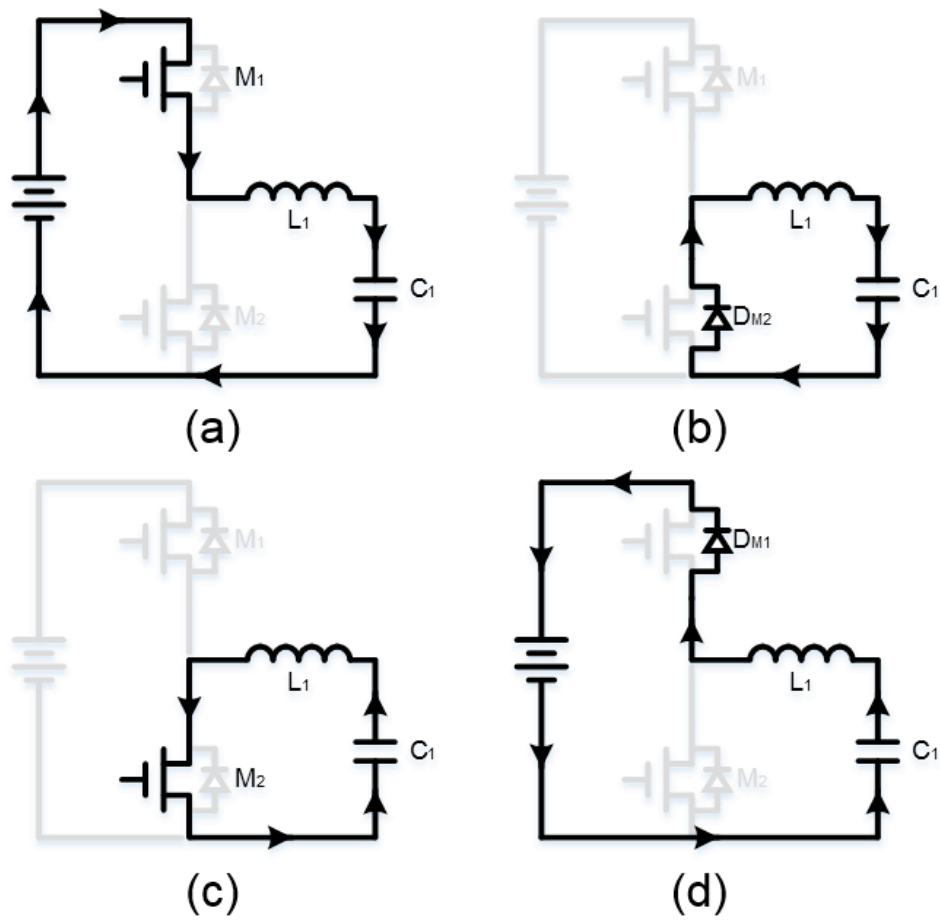
Fig.2.6. Operation states of half-bridge inverter with inductive load.
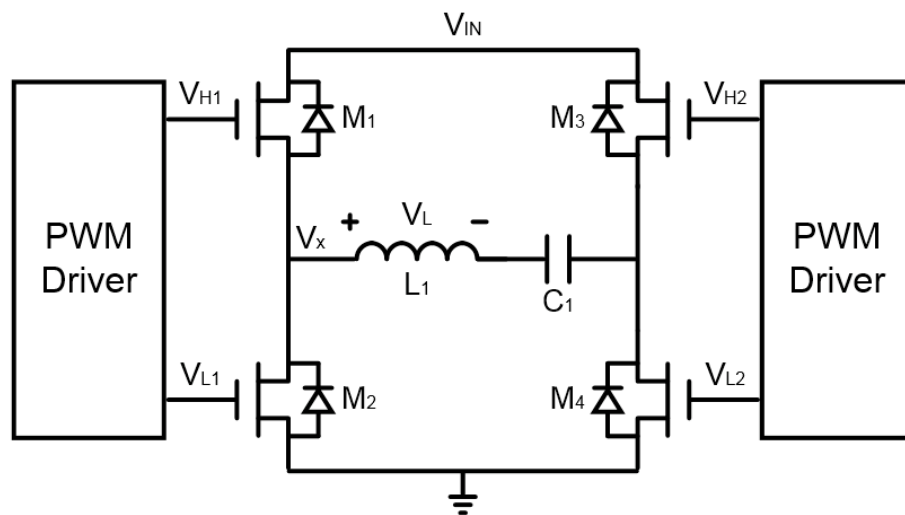
Fig.2.7. Circuit diagram of full-bridge inverter with inductive load.

Fig.2.7 shows a circuit diagram of full-bridge inverter. Full-bridge inverter is made up with four power transistors as switches, four diodes, and PWM driver. Intrinsic body diodes in MOSFET are used for anti-parallel diode. The operating mechanism for generating AC power is same as half-bridge inverter. The performance difference between half-bridge and full-bridge is ratio of voltage and current of output power. Full-bridge has twice larger output voltage than half-bridge in same input voltage. Therefore, full-bridge has lower current than half-bridge in generating same power. This implies that small heat sink is needed for full-bridge inverter, and high power can be generated in full-bridge topology.

Fig.2.8 shows the operation state of full-bridge inverter with inductive load. Same as half-bridge inverter, the operation state is divided into four phase. As shown in Fig.2.8 (a), and (b), the current is conducted from L_1 to C_1. And, the current is negatively flowed from C_1 to L_1 in Fig.2.8 (c), and (d). Current flowing direction is same as half-bridge inverter. However, connected voltage source is different. Left node of L_1, and right node of C_1 are connected to V_{DD}, and GND by turns. This operation generates twice larger output voltage than half-bridge inverter.
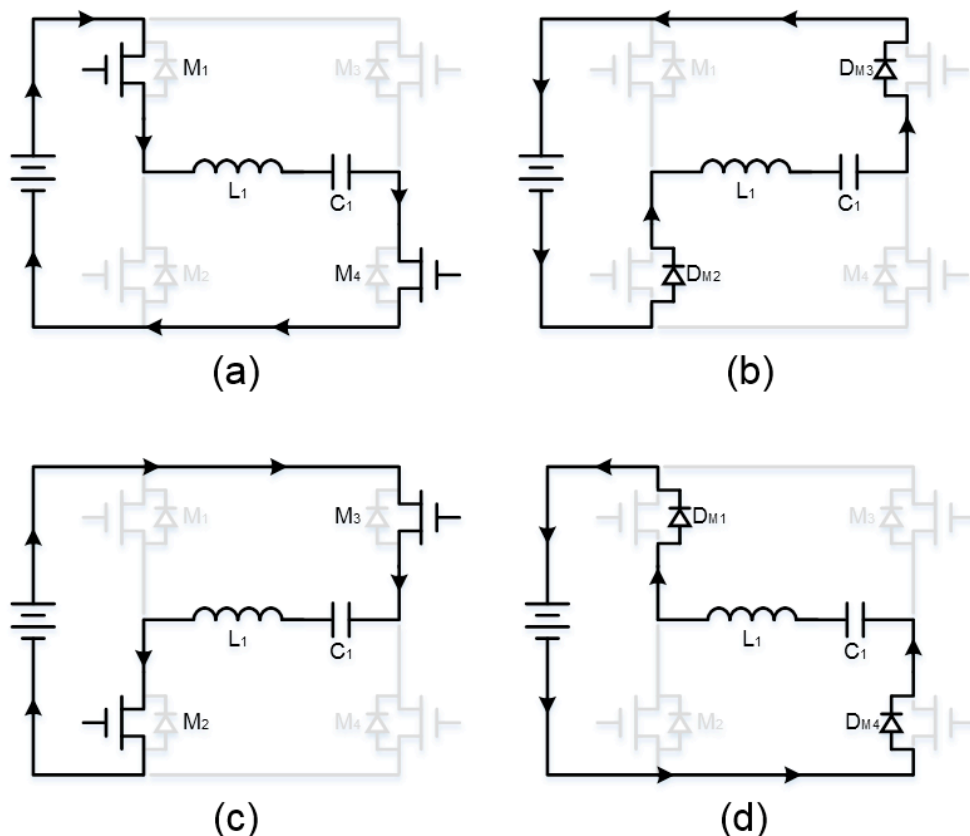
Fig.2.8. Operation states of full-bridge inverter with inductive load.

28
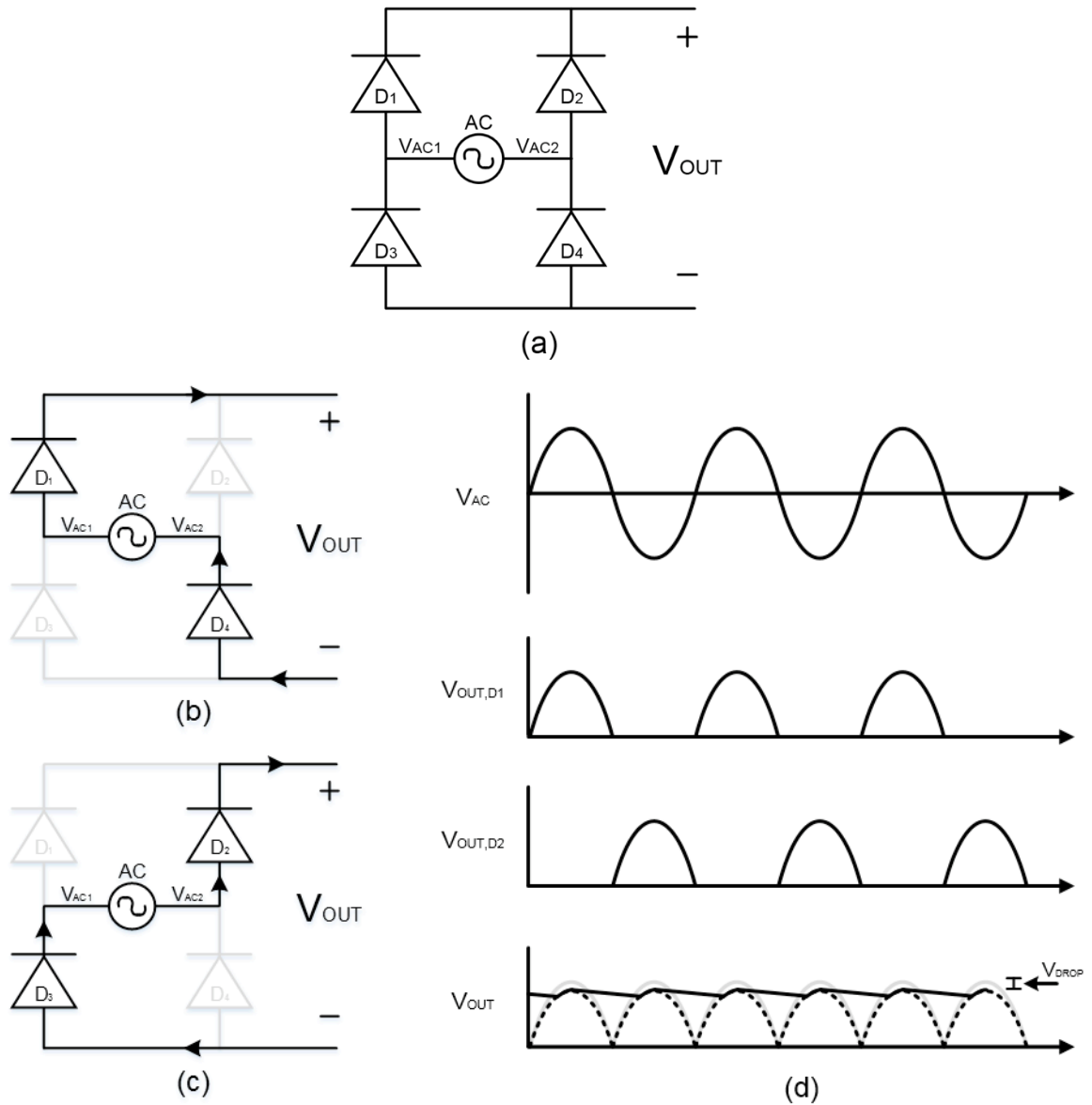
2.4.3 Rectifier

Fig.2.9. Passive rectifier with diodes: (a) circuit diagram, (b, c) operation state, and (d) waveforms.

Transferred power through the air is obtained in AC power. Electric loads are operated by DC power. Hence, AC-DC converter such as rectifier is needed. Conventional rectifier consists of four diodes as shown in Fig.2.9 (a). The diodes are operated in pair of two. As shown in Fig.2.9 (b), D_1 and D_4 are conducting current when V_{AC1} is high than V_{AC2}. The output voltage is illustrated in second column of Fig.2.9 (d). In opposite situation, D_2 and D_3 are operated in pair which is shown in Fig.2.9 (c). Also, the output voltage is illustrated in third column of Fig.2.9 (d). By adding those two waveform, total output voltage is achieved in fourth column of Fig.2.9 (d). The ideally added waveform is mentioned in gray line. If rectifier has capacitor in the load, output voltage becomes flat which is illustrate in black solid line. There is a voltage drop between ideal output voltage, and reality

output. This is caused by diodes. The diode has around 0.7 V drop when it is forward biased. As diode in passive rectifier operates in pair of two, output voltage has around 1.4 V drop. The waveform of output voltage which have voltage drop is shown in Fig.2.9 (d) with black dot line.

An inherent characteristic of diode makes perfect rectification. However, forward biased voltage of diode occurs power dissipation. The power dissipation becomes much critical feature in high current application. Thus, a method using MOSFET rather than diode is introduced. This is called active rectifier. Every diode is replaced into MOSFET. It still uses intrinsic body diode for conducting current, but the current is mostly conducted through MOSFET. There are three types of active rectifier as shown in Fig.2.10 [2.5]-[2.13]. Structure is a little different but controlling mechanism is same. MOSFET is controlled by comparator with sensed voltage across drain and source of MOSFET. A relatively small on-resistance of MOSFET reduces voltage drop. In result, power dissipation in current conducting device is reduced.
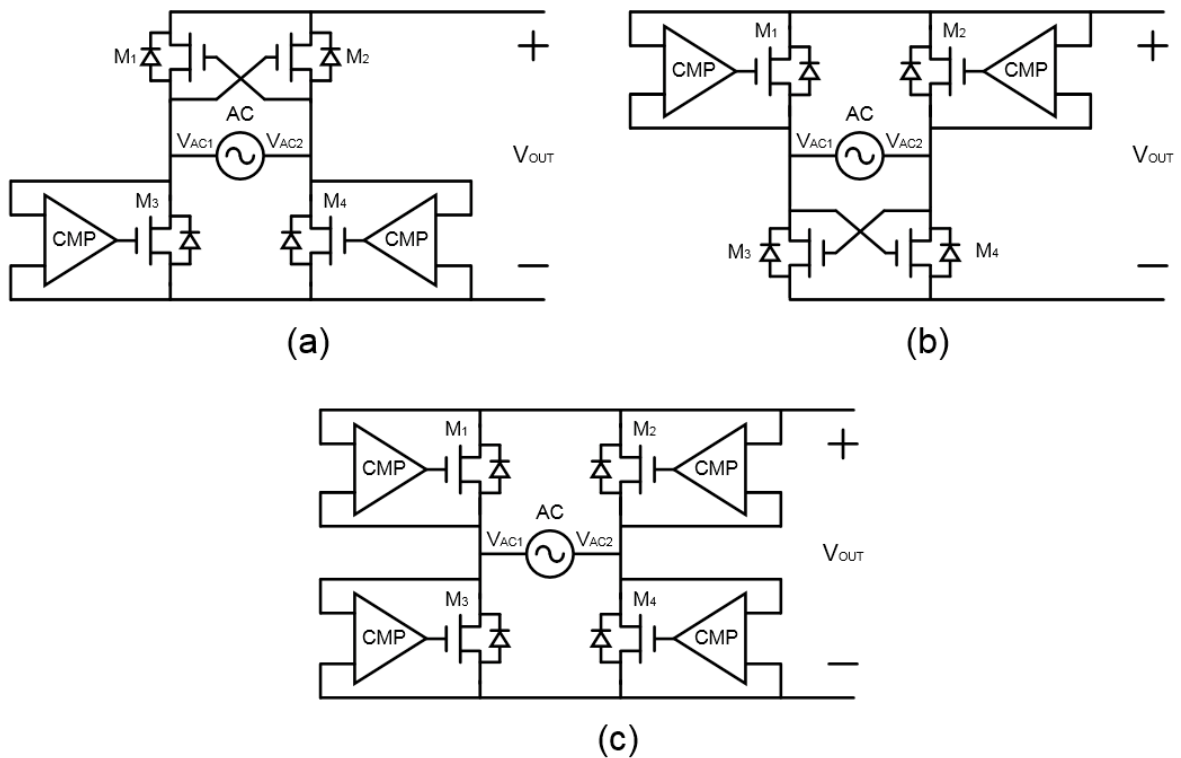
Fig.2.10. Active rectifiers: (a) with cross-coupled PMOS, (b) with cross-coupled NMOS, and (c) fully controlled synchronous active rectifier.

2.4.4 DC-DC converter

The DC-DC converter is popularly used in DC power supplies. There are two types of converter which are linear converter, and switch mode converter. Both has advantage in such applications, but switch mode converter will be discussed in this section. Only non-isolated converter will be handled. The linear convert is discussed in next section as regulator. In switch mode converter, there are switched capacitor converter, and buck converter.

Fig.2.11 shows circuit diagram of basic switched capacitor converter. It has four switches, a flying capacitor, and a load. The voltage conversion is done by charging and discharging mechanism of flying capacitor. Operation state, and waveform are shown in Fig.2.12. C_{fly} is on charge when s1 is on. Voltage across C_{fly} increases in charging phase. In discharging phase, s_1 is off, and s_2 is on. The charges in C_{fly} supply current to load. Periodic operation makes a DC voltage with relatively small voltage ripple. With combination of capacitor and switches, various output voltage can be achieved. However, fixed conversion ratio is achieved because the ratio is decided by topology. Switched-capacitor converter is widely used in low voltage application. MOSFET is used as switch in integrated switched-capacitor converter. Gate voltage is under 5 V for reliability. If gate voltage goes higher than 5 V, MOSFET will be broken. Some manufacture company provides 12 V as a maximum input voltage, but it has to use special process which is much expensive than normal process. Therefore, most of switched-capacitor converter has 5 V as maximum input voltage.
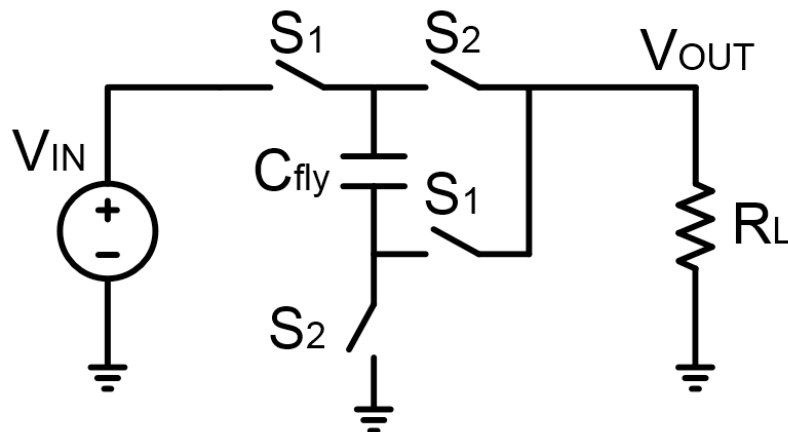
Fig.2.11. Circuit diagram of switched-capacitor DC-DC converter.
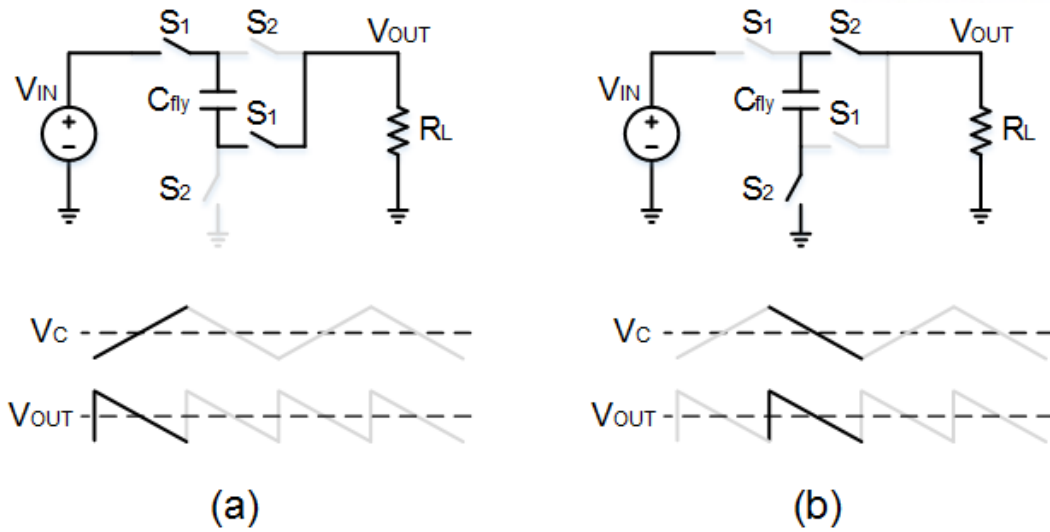
Fig.2.12. Operation states and waveforms of switched-capacitor DC-DC converter (a) charging, and (b) discharging.
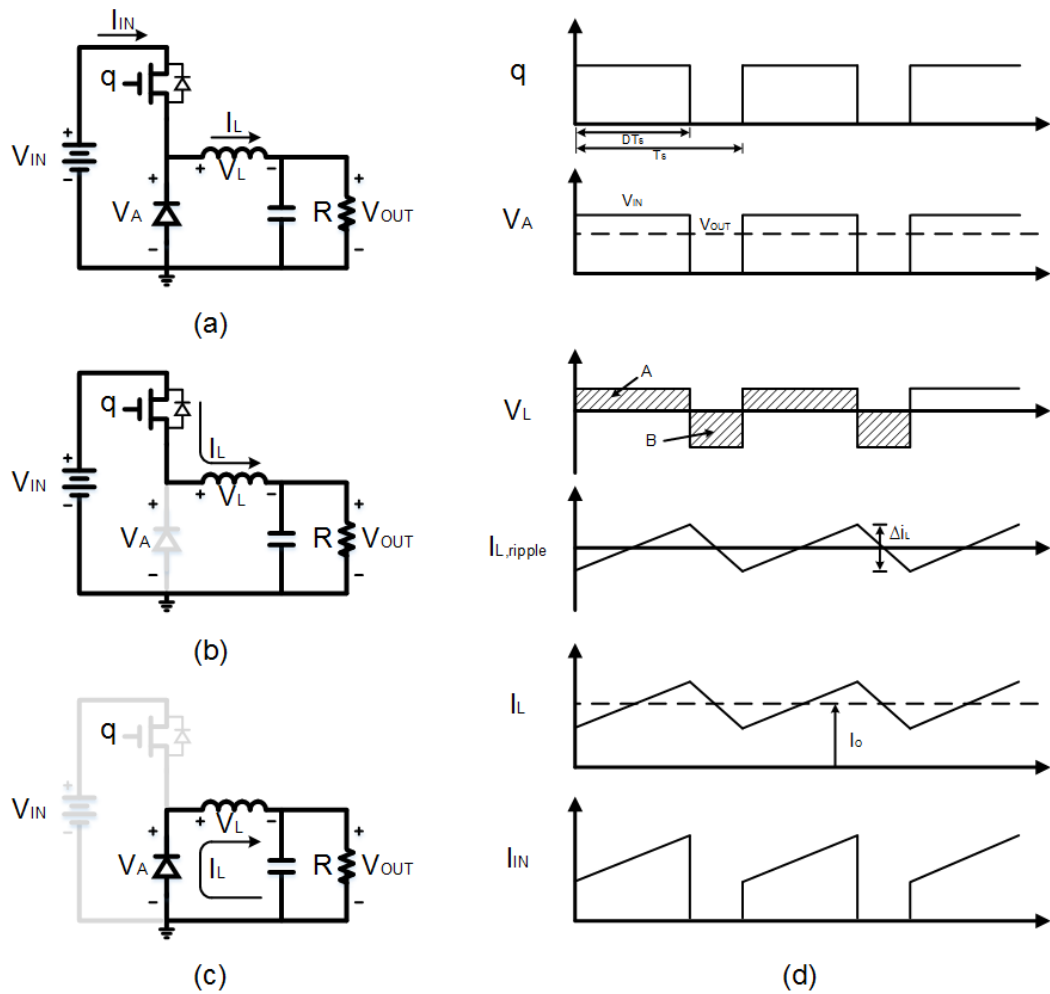
Fig.2.13. Buck converter: (a) circuit diagram, (b, c) operation state, and (d) waveform.

The most popular DC-DC converter in switch mode is buck converter [2.14]-[2.19]. It uses inductor and capacitor, which is called power stage, to convert DC voltage. By changing position of inductor, step up conversion can be performed. In this section, buck converter which is as known as step down converter is discussed. Converting mechanism is identical in every converting mode. Fig.2.13 (a) shows circuit diagram of buck converter. It has a switch with MOSFET, a diode, an inductor, a storage capacitor, and a load. Fig.2.13 (b) shows current charging phase. MOSFET switch is turned on, and it conducts current from power source to inductor. Inductor current, I_L, increase until switch is turned off. Then, stored power in power stage supplies current to the load. Fig.2.13 (c) shows that current is supplied from power stage, and flows through load and diode. It is current discharging phase. In this phase, the I_L decreases until switch is turned on. Fig.2.13 (d) shows waveforms of buck converter. The switch control signal, q, has duty cycle, D. A pulse signal with duty cycle, V_A, flows to LC filter, and becomes DC signal with small ripple. The LC filter act as low pass filter. Average voltage of the pulse signal is output voltage, V_{OUT}. Based on inductor voltage-second balance theory, area of A and B in V_L is equal. Current flowing through inductor is shown as I_L, and average of ripple current, $I_{L,ripple}$, is '0'. If ripple of I_L, Δi_L, is extremely small, I_L can be approximated as DC current. Thus output current, I_O, is achieved. As shown in last column of Fig.2.13 (d), input current, I_{IN}, flows only in charging phase.

2.4.5 Regulator

In previous section, switch mode converters are discussed. Advantage of switch mode converter is high power conversion efficiency in any conversion ratio. However, output voltage regulating speed is very slow. The regulating speed is determined by switching frequency. Switch mode converter uses hundreds of KHz for switching frequency. For high speed system and digital system, the regulating speed must be fast enough to track load variation.

Fig.2.14 shows circuit diagram of linear regulator [2.20]. The linear regulator consists of a path transistor, an error amplifier, resistor for voltage divider, a storage capacitor, and reference voltage. The linear regulator convert voltage with ratio of voltage divider. It employs special characteristic of negative feedback for converting and regulating voltage. The error amplifier is powered by input voltage. Error amplifier has reference voltage as an input. Assume open loop gain of the amplifier is high, another input of the amplifier will be equal to reference voltage. Then ratio of voltage divider, R_1 and R_2, make output voltage, V_{OUT}. If V_{OUT} changes because of load variation, output of the amplifier controls path transistor, M_1, to regulated V_{OUT}. Hence regulating speed is determined by speed of the error amplifier. A storage capacitor is used to compensate stability of negative feedback, and store power for load variation. In linear regulator, there is a significant weakness which is voltage drop between input and output. Difference of input and output voltage is applied to path transistor and make large conduction power loss. Thus, the linear regulator cannot be used for large converting ratio.
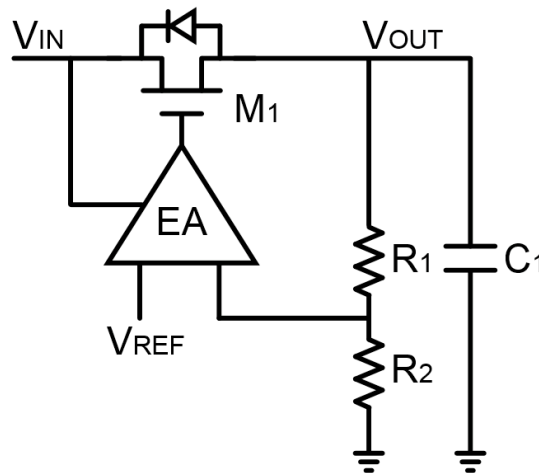
Fig.2.14. Circuit diagram of linear regulator.

2.5 Technical challenges in WPT

2.5.1 Efficiency degradation by coil geometry variation

The magnetically coupled WPT uses two coil to transfer power through the air based on Faraday's law of induction. The intensity of coupling is determined by geometries and arrangement of two coils. Distance between two coils, size difference, angular misalignment, and axial misalignment are the factors that affects the intensity of coupling. Fig.2.15 show typical arrangement of magnetically coupled WPT system. D is diameter of primary coil, D_2 is diameter of secondary coil, L and L_2 are inductance of each coil. Z is distance between primary coil and secondary coil. Based on aforementioned dimension, Fig.2.16 shows efficiency variation that affected by size difference of two coils and distance variation between two coils. The power transfer efficiency between the two coils is determined by a combination of factors. If the two coils are the same size, the efficiency decreases sharply from the moment when the distance between the coils becomes larger than the diameter of the coil. If the two coils are different size, the efficiency decreases sharply from the moment when the distance between the coils becomes larger than the size ratio of two coils. And the efficiency decreases when the difference in the size of two coils become larger.

The intensity of coupling is varied by distance between two coils and axial misalignment of two coils. The arrangement when axial misalignment is occurred is shown in Fig.2.17. Z is distance between two coils, and d is degree of axial misalignment. The coupling coefficient variation by axial misalignment is shown in Fig.2.18 when distance of coils is changed from 0.2 mm to 10 mm. Basically, coupling coefficient is low when distance between two coils are long. And, coupling coefficient becomes low when axial misalignment becomes large. The power transfer efficiency is proportional to the coupling coefficient. Therefore, the power transfer efficiency is low when the coupling coefficient is low.
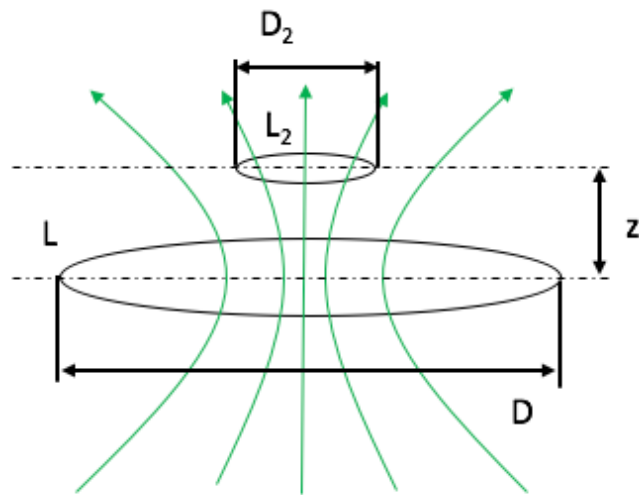
Fig.2.15. Basic arrangement of magnetically coupled wireless power transfer system.
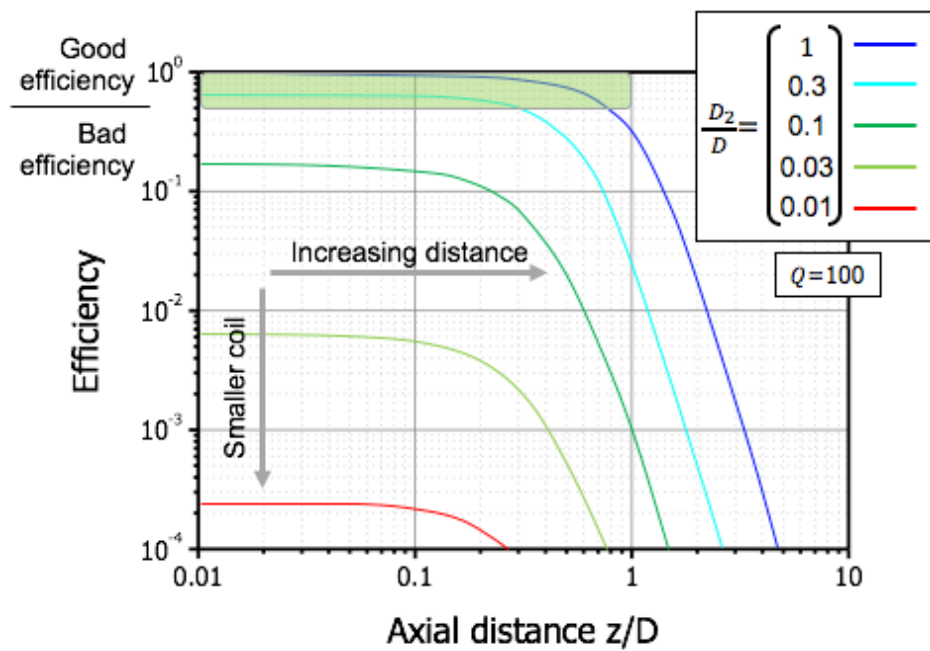
Fig.2.16. Efficiency of magnetically coupled WPT dependence on the relative geometries and distance of coupled coils.
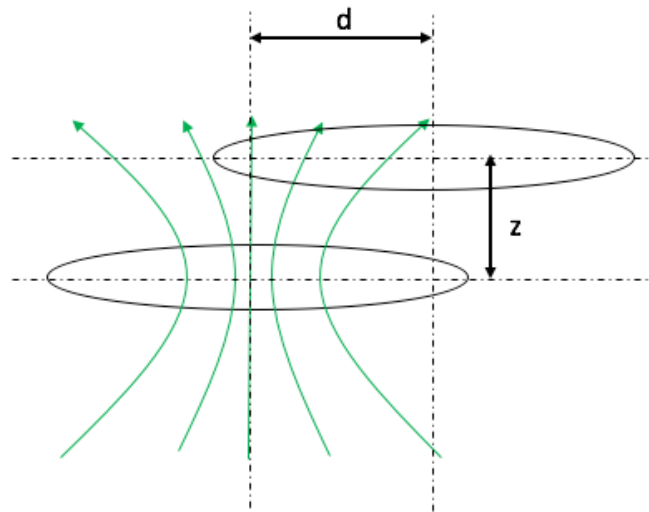
Fig.2.17. Basic arrangement of magnetically coupled wireless power transfer system.
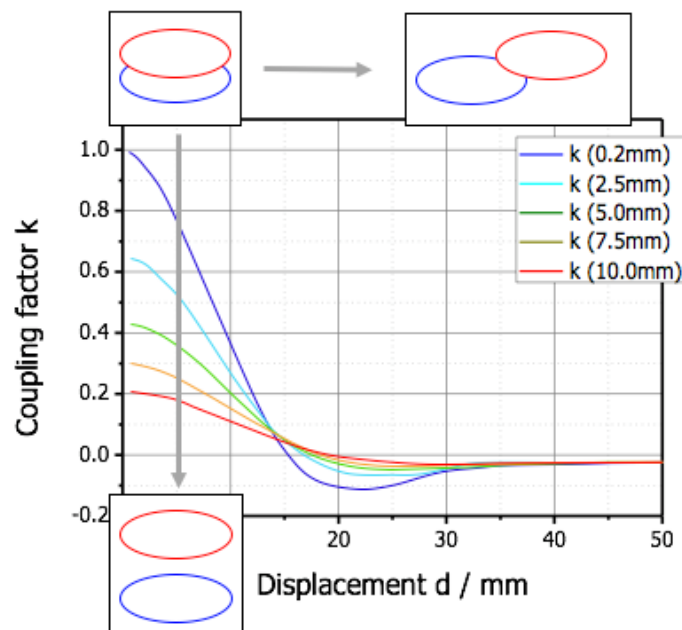
Fig.2.18. Coupling factor dependence on the distance of coupled coils and axial misalignment of coils.

2.5.2 Voltage gain variation with coil geometry

In the previous section, power conversion efficiency variation due to coil geometry variation is discussed. The coil geometry variation changed the efficiency by changing the intensity of coupling. Changes in the coupling result in changes in voltage gain or current gain as well as efficiency. The degree of change of voltage gain or current gain differs depending on the coil topology. It also depends on the size of the load. It is necessary to design a stable system with constant voltage gain with in the situation of the load variation, or the position variation of the receiver. A constant voltage (CV) techniques were introduced in various ways for a strong coupled system with a high coupling coefficient. Changes in transmission frequency or frequency bifurcation are used to provide CV for variation in coupling coefficient or variation in load [2.21]-[2.25]. In the case of weak or loosely coupled system, frequency bifurcation does not occur and a method of varying the frequency has been introduced [2.26]. Generally, magnetic induction is strongly coupled system and magnetic resonance is weak or loosely coupled system. Many techniques to provide CV for the magnetic induction method are introduced, but it still needs more research for magnetic resonance method. Fig.2.19 shows the simulation result of voltage gain changes when coupling coefficient is changed from weak to loosely. The series/parallel topology is used for simulation. The highest voltage gain is achieved when k is around 0.1, but it changes by various parameters such as coil size and the load. However, voltage gain variation in weak coupling coefficient is similar to Fig.2.19. Therefore, a technique to provide CV or technique to suppress the change of voltage gain or a circuit that operates safely within a wide voltage gain is necessary.
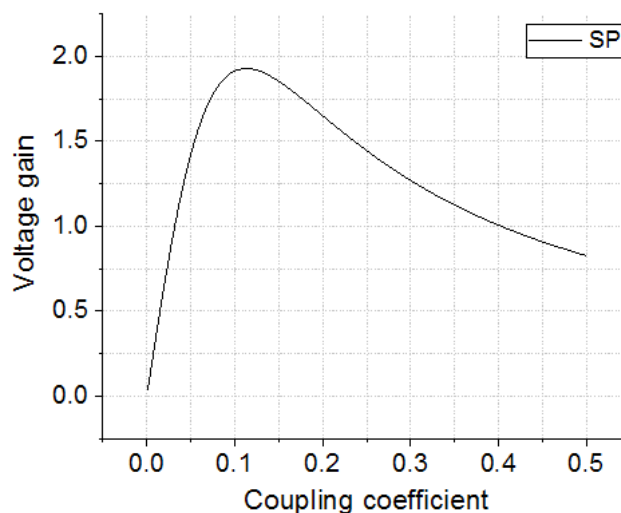
Fig.2.19. Voltage gain vs. coupling coefficient.

2.5.3 Power loss in receiver circuits

The power loss in circuits of wireless power transfer system contributes to degradation in total power conversion ratio from the power supply to the load. Although each of circuit has good power conversion characteristics, the amount of power loss can be significant because power conversion ratio of circuits keeps being multiplied. Since circuits in receiver for wireless power transfer system has identical types of power loss, power loss in buck converter is analyzed. Fig.2.20 shows the switch stage of synchronous buck converter. The main power loss arises due to the power MOSFET switches. The power loss in the switches can be described as combination of the switching loss (P_{SW}) and the MOSFET's conduction loss (P_{COND}) :

$$P_{MOSFET} = P_{SW} + P_{COND} \tag{2.7}$$

where P_{MOSFET} is total power loss in MOSFET. Conduction loss is caused when switch is on. The current which is conducted through on-resistor of MOSFET occurs conduction loss. To reduce conduction loss, on-resistance need to be reduced. The on-resistance of MOSFET is inversely proportional to the size of the MOSFET. Therefore, conduction loss can be reduced by increasing size of MOSFET.
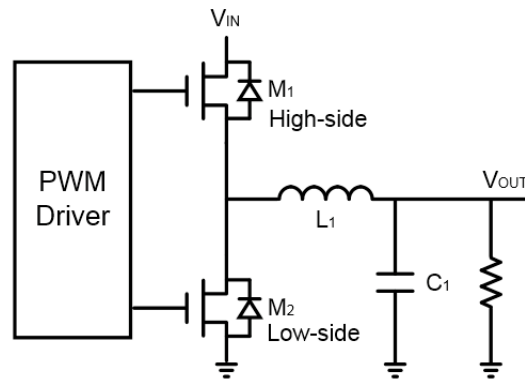
Fig.2.20. Switch stage of synchronous buck converter.
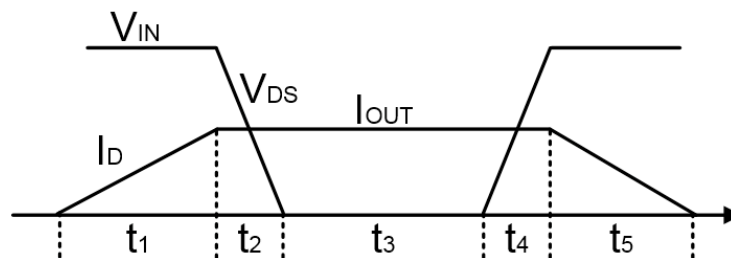
Fig.2.21. Timing diagram of high-side switch.

39

Switching loss occurs during switching transitions. During the transitions of the MOSFET switches, its parasitic capacitance is charged and discharged continuously. Since the parasitic capacitance is dependent on the size of the MOSFET, the switching losses are proportional to the size of the MOSFET. A timing diagram of drain-to-source voltage and current over a period is shown in Fig.2.21. In the timing diagrams, conduction loss occurs in t_3 whereas switching loss occurs in $t_1 + t_2$, and $t_4 + t_5$. Since voltage characteristic for high-side and low-side MOSFET are different, their loss derivation should be calculated separately.

High-side losses is comprised of switching loss and conduction loss as mentioned. The high-side conduction loss is derived as

$$P_{COND} = I_{OUT}^2 \times R_{DS(ON)} \times \frac{V_{OUT}}{V_{IN}} \tag{2.8}$$

where I_{OUT} is output current, V_{OUT} is output voltage, V_{IN} is input voltage, $R_{DS(ON)}$ is the on-time drain-to-source resistance of the high side MOSFET and V_{OUT}/V_{IN} is conversion ratio of buck converter. Switching loss is occurred in turn-on, and turn-off period. For the case of turning the MOSFET switch on, drain current (I_D) is rising linearly while voltage across the drain-to-source of MOSFET drops by the value determined by on-resistance. For the case of turning the MOSFET switch off, the current and the voltage are changed opposite as in turn-on phase. By combining turn-on and turn-off power losses, the total switching power loss in high-side MOSFET is derived as

$$P_{SW} = (\frac{V_{IN} \times I_{OUT}}{2})(f_{SW})(t_{S(rising)} + t_{S(falling)}) \tag{2.9}$$

where f_{SW} is switching frequency, $t_{S(rising)}$ is the rising time, and $t_{S(falling)}$ is the falling time. The transition time is proportional to the value of parasitic capacitance. Therefore, low switching loss is achieved in small size of switch. As we analyzed above, conduction loss and switching loss has opposite phenomenon. Thus, optimization between each loss is needed.

Likewise, total power loss in low-side MOSFET can be calculated with the same method from high-side MOSFET. Conduction loss for low-side MOSFET can be calculated as

$$P_{COND} = (1 - D) \times I_{OUT}^2 \times R_{DS(ON)} \tag{2.10}$$

where D is duty ratio. The equation is almost same as in high-side MOSFET. However, switching loss is a little different. A drain-source voltage (V_{DS}) is voltage drop across inherent diode when current is conducted. The forward biased diode voltage is under 0.7 V. It is relatively lower than input voltage.

Therefore, switching loss in low-side MOSFET can be neglected.

In addition to conduction loss and switching loss in MOSFET, there are few additional losses which is normally much smaller but should be taken into account in low power transfer system. The first additional loss is the power consumed in gate driver of MOSFET switch. Fig.2.22 shows simplified equivalent circuit of gate driver, and MOSFET switch. To calculate power loss in gate driver, the power required to charge the gate capacitance should be considered first :

$$P_{GATE} = Q_G \times V_{DD} \times f_{SW} \tag{2.11}$$

where P$_{GATE}$ is power consumption in the gate, Q_G is the amount of charges required to turn the MOSFET on or off, and V_{DD} is the supply voltage of gate driver. The driving loss occurs in transition period of MOSFET switch. The driving loss in rising transition (P$_{DR(rising)}$) can be derived as :

$$P_{DR(rising)} = \frac{P_{GATE} \times R_{DRIVER(PULL-UP)}}{2R_{TOTAL}} \tag{2.12}$$

where R$_{DRIVER(PULL-UP)}$ is resistance of pull-up resistor, and R$_{TOTAL}$ is resistance combination of driver output resistance (R$_{driver}$) and gate input resistance (R$_{gate}$). The driving loss in falling transition (P$_{DR(falling)}$) can be derived as :

$$P_{DR(falling)} = \frac{P_{GATE} \times R_{DRIVER(PULL-DOWN)}}{2R_{TOTAL}} \tag{2.13}$$

where R$_{DRIVER(PULL-DOWN)}$ is resistance of pull-down resistor.
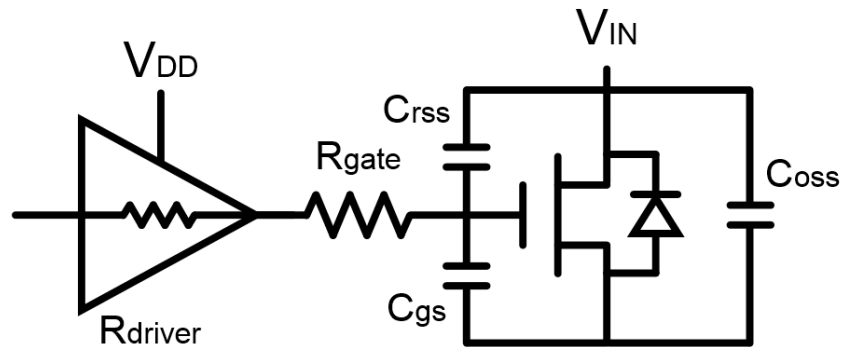
Fig.2.22. Equivalent circuit of gate driver, and MOSFET switch.

Therefore, the total power loss in the driver (P_{DRIVER}) is :

$$P_{DRIVER} = P_{DR(rising)} + P_{DR(falling)} \qquad (2.14)$$

The second additional loss is diode conduction loss. Under diode conduction condition, both MOSFETs are off. During this time, the inherent diode in MOSFET conducts current in forward biased condition. The diode conduction power loss (P_{DIODE}) caused during this time is:

$$P_{DIODE} = D \times f_{SW} \times V_F \times I_{OUT} \qquad (2.15)$$

where V_F is the forward biased voltage across the diode.

2.6 Challenges for body implantable medical devices

2.6.1 Space limitation

The performance of WPT is affected by the size of the system. The implant location of the BIMD is determined by the function of the device. In the case of a cardiac pacemaker, it is designed to be large because it is implanted in a large space. However, such devices like bio-sensors and the retina implant are implanted in very small space, which limits the size of the system. WPT can have a positive effect when it is applied to a bio-sensors and the retina implant that are difficult to insert a large capacity battery. Therefore, WPT for certain BIMD should be developed with the size limitation by the implantation space.

First of all, the size of the implanted power receiving coil is small. Since the size of the receiving coil is small and invisible, the power transmitting coil is designed to be larger than the receiving coil. The axial misalignment problem is resolve with larger transmitting coil. However, if the size of the coils is different, the coupling coefficient and power transfer efficiency are reduced in proportion to the coil size. Also, power transferring distance becomes shorter in proportion to the ratio of the size of the coils. In low coupling condition, the power transfer performance is sensitive to coil distance, which is equal to skin depth, and alignment changes.

The space constraint makes external components difficult to use. External component that are needed in WPT system are component for impedance matching, bootstrap capacitor, and component for charge storage. The use of many external components make the WPT system large. The effort should be made to reduce the number of external components.

2.6.2 Human health hazard

Electronic devices intended for medical devices or human body must meet the specific absorption rate (SAR) regulation. SAR is the measure of the rate that describes how much electromagnetic waves generated by electronic products are absorbed by the human body. SAR is used in units of W/kg and is standardized to the maximum allowable value. There are different SAR regulations for each part of the body. Table 2.1 is the SAR regulation provided by the Institute of Electrical and Electronics Engineers (IEEE) [2.27]. SAR regulation for those people in controlled environment is higher than for those people in normal environment. The average SAR is used for the whole body, and the localized SAR is used for part of the body. A sample volume of 1g or 10g is used in localized SAR.

Tables 2.2 and 2.3 show the maximum permissible exposure (MPE) data provided by the IEEE [2.27]. Table 2.2 applies to the people in controlled environment and Table 2.3 applies to the people in general environment. IEEE says that compliance with MPE is equivalent to basic SAR restriction (BR) compliance. However, lack of compliance with BR does not imply lack of compliance with MPE. Even if BR is satisfied, MPE can be exceeded. Therefore, it is recommended that an additional evaluation of MPE should be carried out when the BR is satisfactory. In conclusion, compliance with the whole-body BR or MPE is sufficient.

Table 2.4 shows the SAR standards of other international organizations and countries. Each country has specifications that are similar to each other. SAR restriction must be fulfilled because absorbing high electromagnetic wave can cause health disorder. Since the restrictions are listed with maximum value, commercial electronics should be made to hold values much lower than the restrictions.

Table 2.1. SAR restriction for frequency from 100 kHz to 3 GHz provided by IEEE

		Action level[a] SAR[b] (W/kg)	Person in controlled environments SAR[c] (W/kg)
Whole-body exposure	Whole-body average	0.08	0.04
Localized exposure	Localized (peak spatial-average)	2[c]	10[c]
	Extremities[d] and pinnae	4[c]	20[c]
[a]BR for the general public when an RF safety program is unavailable			
[b]SAR is averaged over the appropriate averaging times as shown in Table 3 and Table 4.			
[c]Averaged over an 10g tissue (defined as a tissue volume in the shape of a cube). *			
[d]The extremities are the arms and legs distal from the elbows and knees, respectively.			

*The volume of the cube is approximately 10 cm^3.

Table 2.2. MPE for people in controlled environments (for the upper tier)

Frequency range (MHz)	RMS electric field strength (E)[a] (V/m)	RMS magnetic field strength (H)[a] (A/m)	RMS power density (S) E-field, H-field (W/m^2)	Averaging time |E|^2, |H|^2 or S (min)
0.1-1.0	1842	$16.3/f_M$	$(9000, 100000/f_M^2)^{\text{b}}$	6
1.0-30	$4842/f_M$		$(9000/f_M^2, 100000/f_M^2)$	6
30-100	61.4		$(10, 100000/f_M^2)$	6
100-300	61.4	0.163	10	6
300-3000			$f_M/30$	6
3000-30000			100	$19.63/f_G^{1.079}$
30000-300000			100	$2.524/f_G^{0.476}$

NOTE—f_M is the frequency in MHz, f_G is the frequency in GHz.

[a]For exposures that are uniform over the dimensions of the body, such as certain far-field plane-wave exposures, the exposure field strengths and power densities are compared with the MPEs in the Table. For non-uniform exposures, the mean values of the exposure fields, as obtained by spatially averaging the squares of the field strengths or averaging the power densities over an area equivalent to the vertical cross section of the human body (projected area), or a smaller area depending on the frequency (see NOTES to Table 3 and Table 4 below), are compared with the MPEs in the Table.

[b]These plane-wave equivalent power density values are commonly used as a convenient comparison with MPEs at higher frequencies and are displayed on some instruments in use.

Table 2.3. MPE for general environment where a RF safety program is unavailable

Frequency range (MHz)	RMS electric field strength (E)[a] (V/m)	RMS magnetic field strength (H)[a] (A/m)	RMS power density (S) E-field, H-field (W/m^2)	Averaging time |E|^2, |H|^2 or S (min)	
0.1-1.34	614	$16.3/f_M$	$(1000, 100000/f_M^2)^{\text{c}}$	6	6
1.34-3	$823.8/f_M$	$16.3/f_M$	$(1800/f_M^2, 100000/f_M^2)$	$f_M^2/0.3$	6
3-30	$823.8/f_M$	$16.3/f_M$	$(1800/f_M^2, 100000/f_M^2)$	30	6
30-100	27.5	$158.3/f_M^{1.668}$	$(2, 9400000/f_M^{3.336})$	30	$0.0636f_M^{1.337}$
100-400	27.5	0.0729	2	30	30
400-2000			$f_M/200$	6	
2000-5000			10	$19.63/f_G^{1.079}$	
5000-30000			10	$2.524/f_G^{0.476}$	
30000-100000			10		
100000-300000			$(90f_G\text{-}7000)/200$		

NOTE—f_M is the frequency in MHz, f_G is the frequency in GHz.

[a]For exposures that are uniform over the dimensions of the body, such as certain far-field plane-wave exposures, the exposure field strengths and power densities are compared with the MPEs in the Table. For non-uniform exposures, the mean values of the exposure fields, as obtained by spatially averaging the squares of the field strengths or averaging the power densities over an area equivalent to the vertical cross section of the human body (projected area) or a smaller area depending on the frequency (see NOTES to Table 3 and Table 4 below), are compared with the MPEs in the Table.

[b]The left column is the averaging time for \|E\|^2, the right column is the averaging time for \|H\|^2. For frequencies greater than 400 MHz, the averaging time is for power density S.

[c]These plane-wave equivalent power density values are commonly used as a convenient comparison with MPEs at higher frequencies.

Table 2.4. SAR restriction of other international organizations and countries

Classification		Korea	Japan	USA	CENELEC[a]	ICNIRP[b]
Frequency range		100kHz~ 10GHz	100kHz~ 3GHz	100kHz~ 600MHz	10kHz~ 300GHz	100kHz~ 10GHz
General environment	Whole-body	0.08	0.08	0.08	0.08	0.08
	Head/Trunk	1.6	2	1.6	2	2
	Arm/Leg	4	4	4	4	4
People in controlled environment	Whole-body	0.4	0.4	0.4	0.4	0.4
	Head/Trunk	8	10	8	10	10
	Arm/Leg	20	20	20	20	20

[a]European Committee for Electrotechnical Standardization

[b]International Commission on Non-Ionizing Radiation Protection

2.6.3 Safe operation

Since BIMD is implanted into the human body, it cannot be seen by eyes. And the implantation depth is different for each person because the thickness of the skin is different. In WPT, the axis alignment and transmission distance have a large impact on performance. Usually, transmitter coil is made larger than receiver coil to avoid axis misalignment. The axis alignment problem is solved by using larger transmitter, but the power transfer performance drops due to the coil size difference. Power transfer efficiency is the main performance in WPT, but voltage gain for hardware fabrication is also important parameter to concern. Due to the difference in the size of the coils and the change in the transfer distance, the voltage gain changes proportional to the efficiency. Particularly in the field of very low coupling such as BIMD, the voltage gain variation is susceptible to the coil geometric.

In BIMD, safe operation is paramount. Not only lowing the damage to the human body by SAR is important in WPT, but also protecting implanted hardware from destruction in also important in WPT for BIMD. Transistors used in hardware fabrication have the maximum allowable voltage. If the voltage exceeds the maximum allowable voltage, the transistor burns or breaks. There is a package that surrounds the integrated circuit (IC). However, if the hardware fails or malfunction occurs, it may cause safety problems. Therefore, IC in the receiver implanted into the human body should be designed to operate safely in any geometric conditions or have tolerance to voltage gain variation.

Chapter III

Preliminary Research on Techniques for Improving Performance in WPT

3.1 Efficiency enhancement in coil geometric variation

3.1.1 Background

With the rapid development of wireless communication and semiconductor technologies, the area of sensor networks has grown significantly, with a range of applications that include medical and health care systems. A wireless body area network (WBAN) is a special-purpose sensor network designed to connect various medical sensors and appliances, located inside or outside the human body, which monitor temperature, blood pressure, heart rate, oxygen saturation (SpO_2)-level, glucose, gastrointestinal images, etc. A WBAN system can offer two significant advantages compared to the existing electronic patient monitoring systems. The first is the increased mobility of patients due to the portable or implanted monitoring devices, and the second is the location-independent monitoring facility [3.1]. Meanwhile, visualization of the human gastrointestinal (GI) tract, upper small intestine, and colon became possible after the development of optical fiber endoscopy. Generally, flexible wire endoscopy does not present significant problems. However, small intestine endoscopy, gastroscopy, and colonoscopy induce discomfort among patients due to the large-diameter flexible cables needed to withstand the push force, and which carry a video signal and power through optical fiber and wire. In addition, visualization in some GI tracts is still difficult using flexible wire endoscopy [3.2]. For this reason, through the rapid progress of semiconductor and communication technologies, capsule endoscopy has arisen as a new advanced technology to address the problems with flexible wire endoscopy, as illustrated in Fig.3.1 [3.3], [3.4]. In most biomedical sensor networks, the limit on the amount of power that can be supported by the embedded battery presents a problem. Implantable devices such as a glucose sensor, implantable defibrillator, retinal display, and gastric stimulator have to be taken out periodically via surgery to change the battery, causing patients great discomfort and the potential for complications, just as in other procedures. Recently, capsule endoscopy has also encountered the power shortage problem in the GI tract because of the demand for higher resolution video and the increase in the number of integrated functions [3.1], [3.5], [3.6]. Capsule endoscopy consists of several parts, including vision, control, and data transmission components, in a capsule that is typically 11 mm in diameter by 25 mm in length. Although different amounts of energy are

consumed, depending on the components, it is clear that each part consumes electrical energy. Vision processes, the first element of capsule endoscopy, utilize a CMOS image sensor, light-emitting diode (LED) illuminator, and processor. In the previously used capsule endoscopy products, the data rate of the images was a few Mbps because of the limitation of the technology in this field [3.7]. However, with increasing consumer demand and developing technologies, the frame rate and quality of images have improved. The HDCMOS image sensor provides up to 30 fps at 1920×1080 pixels per frame at a data rate of 78 Mb/s [3.8]. It consumes almost 40 mW of power. The LED illuminator should also turn on more frequently, and the processor consumes about 10 mW. With four LED illuminators in use, the total power consumption of the vision component is more than 95 mW. With respect to the control element, movement is an additional advanced function in demand. In terms of the current capsule endoscope market, the locomotion controls and actuators have not been commercialized. These locomotion controls and actuators are considered to be essential parts of future capsule endoscopes for fast and accurate diagnosis [3.9]–[3.11]. However, this increased benefit corresponds to increased power consumption. For example, locomotion requires more than 300 mW, while actuators consume more than 200 mW. Fortunately, these control features are only used during a short period, as opposed to being used for the entire operating time. Finally, the data transmission part consists of a transmitter and receiver. This part consumes approximately 5 mW, which is less than the other two parts. However, the transmitter is used during the entire procedure, and its total power consumption can accumulate to a significant number that is comparable to the locomotion control and actuators. The receiver is utilized less than the transmitter, but its power consumption is almost the same as that of the transmitter. Since the total power consumption greatly depends on the power consumed in the control parts, it is not trivial to estimate its exact value. A rough estimate is approximately 300 mW. This value is quite high considering the typical capacity of commercially available batteries [3.12]. Meanwhile, wireless power transfer (WPT) is a very suitable technology to improve the battery capacity limitation. It is a promising technology that can transfer power without wires. There are three types of WPT technologies: an inductive coupling system for very short distances of a few millimeters, a magnetic resonance system for midrange transmission from a few centimeters to a few meters [3.13], and an electromagnetic wave system for long-distance applications. The inductive coupling system is not good for biomedical applications because of the short transfer distance, and the electromagnetic wave system is also unsuitable because of the huge absorption rate in the human body, which causes safety issues and difficulty with alignment [3.14], [3.15]. The magnetic resonance-wireless power transfer (MR-WPT) system is the most suitable solution among the available types for medical implantable devices. However, a conventional MR-WPT system still suffers from efficiency degradation, due to changes in the position of the receiver. The capsule endoscopy receiver is always moving through the GI tract, which results in transfer efficiency degradation caused by the variations

in the distance, angle, and axial misalignment. Some researchers improved the WPT efficiency using ceramic filled cavity [3.16]. Yet the system was still not suitable under varying conditions. Hence, an MR-WPT system for a biomedical capsule endoscopy application must have additional methods to maintain a strong transfer efficiency under these dynamic circumstances. In previous research [3.17]-[3.20], an efficiency improvement was demonstrated, limited to a distance change with a symmetric coil WPT system. A multiple coil WPT system [3.12], [3.21] is introduced to further improve efficiency. However, it occupies large volume that is very difficult to implant with small volume suitable for capsule endoscopy. This section presents an adaptive technique to track the high transfer efficiency of an MR-WPT system with variations in the relative distance, angle, and axial misalignment between asymmetric transmitting and receiving parts

.
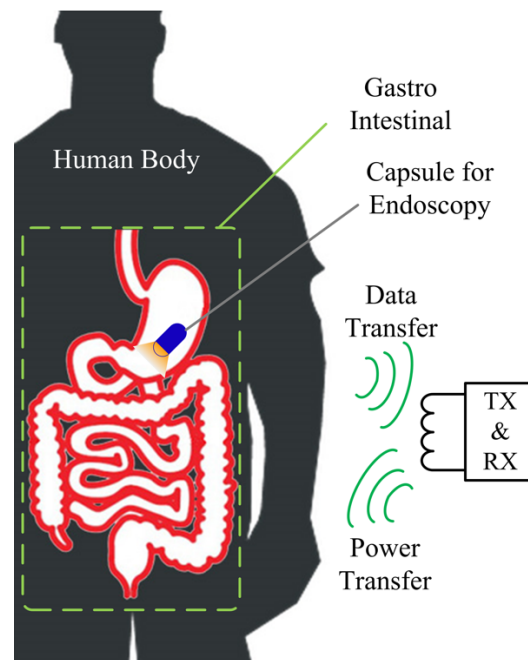
Fig.3.1. Concept of capsule endoscopy with wireless power transfer in gastrointestinal (GI) tract of human body.

3.1.2 MR-WPT model analysis

Prior to discussing the work to determine the optimal tracking efficiency of the MR-WPT system in biomedical capsule endoscopy applications, the fundamental transfer characteristics of a general MR-WPT system are analyzed. Then, the analysis is extended to model the biomedical capsule endoscopy environment. In biomedical capsule endoscopy applications, a receiver moves along the human GI tract, which causes variations in the distance, angle, and axial misalignment between the transmitter and receiver. This results in a degradation of the transfer efficiency. In this section, circuit and electromagnetic analyses are performed to define the essential model parameters for the design and present methods to overcome such issues. The circuit analysis focuses on the parameters affecting the coupling coefficient of the MR-WPT system. The electromagnetic analysis shows how the coupling coefficient is affected in terms of the dimensional parameters such as the distance and angle, which make the MR-WPT system controllable.

3.1.2.1 Power transfer characteristics, and analysis on geometric variation

A strongly coupled MR-WPT system consists of four coils. The proposed model of the MR-WPT system for capsule endoscopy, as illustrated in Fig. 3.2, consists of a power coil, transmitting coil (TX coil), receiving coil (RX coil), and load coil. The power coil is connected to a source outside of the human body. The load coil is connected to a capsule endoscopy system and provides additional power beyond the integrated battery. The TX and RX coils are called resonators, which are designed to resonate at the same frequency and have a high quality factor with high inductance and low capacitance.

Fig. 3.3 shows the equivalent circuit model of the four-coil MR-WPT system to analyze the maximum transfer efficiency condition. The circuit consists of four separate circuits. These circuits are connected via a magnetic field, which can be characterized by coupling coefficients k_{12}, k_{23}, and k_{34}. The coupling coefficient has a value between 0 and 1, which can be expressed as follows:

$$k_{xy} = \frac{M_{xy}}{\sqrt{L_x L_y}} \tag{3.1}$$

where M_{xy} is the mutual inductance between the "x" and "y" coils; and the parameters of each circuit are characterized by the resistance R_x, inductance L_x, and capacitance C_x.
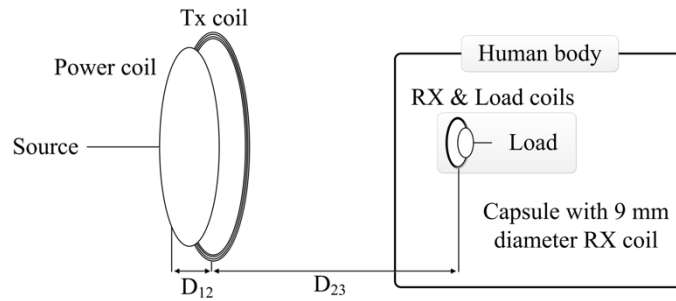
Fig.3.2. Diagram model of the wireless power transfer system for capsule endoscopy.
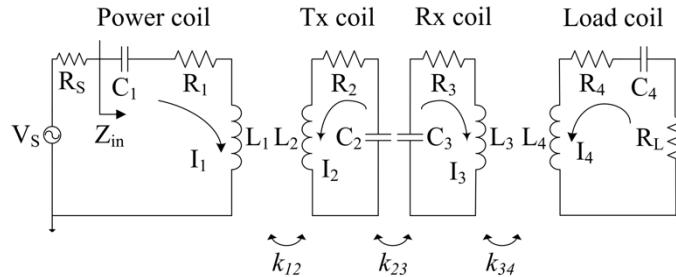
Fig.3.3. Equivalent circuit model of a magnetic resonance wireless power transfer(MR-WPT) system.

This circuit model offers an effective way to analyze the characteristics of the proposed system. First, by applying Kirchhoff's voltage law to this model, the relationship between the currents through each coil and the voltage applied to the power coil can be expressed using the following matrix:

$$
\begin{bmatrix} I_1 \\ I_2 \\ I_3 \\ I_4 \end{bmatrix} = \begin{bmatrix} Z_1 & j\omega M_{12} & 0 & 0 \\ j\omega M_{12} & Z_2 & j\omega M_{23} & 0 \\ 0 & j\omega M_{23} & Z_3 & j\omega M_{34} \\ 0 & 0 & j\omega M_{34} & Z_4 \end{bmatrix}^{-1} \begin{bmatrix} V_s \\ 0 \\ 0 \\ 0 \end{bmatrix}
\tag{3.2}
$$

where Z_1, Z_2, Z_3, and Z_4 are the loop impedances of the four coils. These terms can be expressed as follows:

$$
Z_1 = R_s + R_1 + j\left(\frac{\omega L_1 - 1}{\omega C_1}\right) \approx R_s
$$

$$
Z_2 = R_2 + j\left(\frac{\omega L_2 - 1}{\omega C_2}\right) = R_2
$$

$$
Z_3 = R_3 + j\left(\frac{\omega L_3 - 1}{\omega C_3}\right) = R_3
$$

$$
Z_4 = R_L + R_4 + j\left(\frac{\omega L_4 - 1}{\omega C_4}\right) \approx R_L
\tag{3.3}
$$

where $j\left(\omega L_x - \frac{1}{\omega C_x}\right)$ is zero at the resonance condition, and we assume that $R_s + R_1 \approx R_s$, and $R_L + R_4 \approx R_L$ because $R_s \ll R_1$ and $R_L \ll R_4$. The currents in the power and load coils are expressed by 3.4:

$$
I_4 = \frac{j\omega^3 k_{12} k_{23} k_{34} L_2 L_3 \sqrt{L_1 L_4}}{(R_s R_2 + \omega^2 k_{12}^2 L_1 L_2)(R_L R_3 + \omega^2 k_{34}^2 L_3 L_4) + R_s R_L \omega^2 k_{23}^2 L_2 L_3} V_s.
\tag{3.4}
$$

The efficiency of the WPT system can be expressed by the following equation:

$$
\eta = \frac{P_{out}}{P_{in}} = \frac{\frac{V_L^2}{R_L}}{\frac{V_s^2}{4R_s}} = |S_{41}|^2
\tag{3.5}
$$

where η is the efficiency of the MR-WPT system, and P_{in} and P_{out} are the source power from the power coil and delivered power at the load coil, respectively. V_L and V_s are the voltages applied to the load and source, respectively. R_L and R_s are the port reference impedances with 50Ω. This system model can be considered to be a two-port network. The S-parameter is a commonly used

figure of merit for a given WPT system. S_{21} indicates the power transfer efficiency, which is given by $|S_{21}|^2$, the square magnitude of S_{21}. The S_{21} parameter is calculated as follows:

$$S_{41} = 2\frac{V_L}{V_s}\sqrt{\frac{R_s}{R_L}}$$

(3.6)

The magnitude of S_{21} can be expressed by solving (3.4) and (3.6):

$$|S_{41}| = 2\frac{V_L}{V_s}\sqrt{\frac{R_s}{R_L}} = \frac{2\omega^3 k_{12}k_{23}k_{34}L_2L_3\sqrt{L_1L_4}\sqrt{R_sR_L}}{(R_sR_2+\omega^2 k_{12}^2 L_1L_2)(R_LR_3+\omega^2 k_{34}^2 L_3L_4)+R_sR_L\omega^2 k_{23}^2 L_2L_3}.$$

(3.7)

The relationship between the transfer efficiency and coupling coefficient is analyzed using the circuit models, and the following demonstration focuses on the relationship between the coupling coefficient and geometric factors. In Fig.3.4, a concentric resonator pair of single-turn loops with radii r_x and r_y $(r_x \ll r_y)$, vertical displacement z, and angle θ between the y loop surface plane and plane parallel to the loop is presented [3.22]. The Biot–Savart law leads to an expression for the magnetic flux density B_x at a field point r (at height z above the center of the loop axis) that is induced by the x loop

$$B_x = \int_x dB_x = \frac{\mu_0}{4\pi}I_x\int_x \frac{dl \times r}{|r|} = \frac{\mu_0 I_x r_x^2}{2(r_x^2+D_{xy}^2)^{\frac{3}{2}}}$$

(3.8)

where $I_x dl$ is the infinitesimal current source line on the x loop, and μ_0 is the permeability of the free space. Faraday's law and Lenz's law imply that a time-varying current in the x loop (I_x) results in a time variation of the magnetic flux through the y loop ($\Phi_{y,x}$). The minus sign in (3.9) is an indication that the EM field is in such a direction as to produce a current whose flux reduces the magnitude of the EM field:

$$\varepsilon_{y,x} = -\frac{d\Phi_{y,x}}{dt} = -\frac{d}{dt}\int_S B_x \cdot ds_y = -M\frac{dI_x}{dt}$$

(3.9)

where ds_y is the infinitesimal surface area element defined by the x loop, and M is the mutual inductance between coils.

54

Combining (3.1), (3.8), and (3.9) creates a new expression in geometric terms (coil radii r_x and r_y, vertical displacement factor D_{xy}, and angle θ) for the coupling coefficient:

$$k_{xy} = \frac{\mu_0 \pi r_x^2 r_y^2 \cos\theta}{2\sqrt{L_x L_y}(r_x^2 + D_{xy}^2)^{\frac{3}{2}}}$$

(3.10)

where μ_0 is the permeability of the medium, and r_x and r_y are the coil radii. L_x and L_y are the inductances of the coils. D_{xy} is the distance between the coils. This equation indicates that the coupling coefficient could be controlled using vertical displacement factor D_{xy} and angle θ.
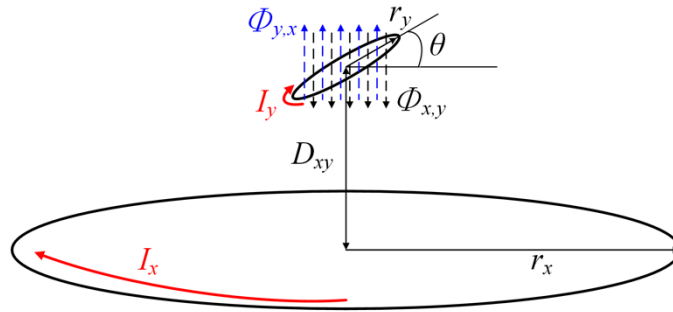
Fig.3.4. Proposed simple magnetic resonance wireless power transfer coils with geometric and electrical factor for capsule endoscopy.

55

3.1.2.2 Maximum power transfer conditions

Equation (3.7) expresses the power transfer efficiency of an MR-WPT system. When the relative positions of the TX and RX coils are changed, the modified k_{23} induces a degradation in $|S_{41}|$, which results in a reduced power transfer effi ciency for the MR-WPT system. $|S_{41}|$ has a maximum value at the peak value that could be found by the derivative of $|S_{41}|$ with respect to k_{12}. At $\frac{d|S_{41}|}{dk_{12}} = 0$, the maximum effi ciency condition of the given MR-WPT system is achieved by the careful control of the k_{12} value

$$k_{12} = \sqrt{\frac{R_S R_L R_2 R_3 + R_S R_2 \omega^2 k_{34}^2 L_3 L_4 + R_S R_L \omega^2 k_{23}^2 L_2 L_3}{\omega^4 k_{34}^2 L_1 L_2 L_3 L_4 + R_L R_3 \omega^2 L_1 L_2}} \ at \ \frac{d|S_{41}|}{dk_{12}} = 0. \tag{3.11}$$

Fig.3.5 shows an S_{41} graph of (3.7) and the relationship between k_{12} and k_{23}, where k_{12} is the controllable value, and k_{23} is given by the circumstances. To maximize the transfer efficiency, the optimal k_{12} value can be obtained depending on the k_{23} change caused by the movement of the receiver along the GI tract, as illustrated in (3.10). The coupling coefficient (k_{xy}) is a function of the distance and angle. The value of k_{12} can be optimized to achieve the maximum efficiency of the system by changing the vertical displacement (D_{12}) between the power and TX coils, along with angle between the power and TX coils. This new derivation for the MR-WPT system promises a strong power transfer system for biomedical capsule endoscopy applications.
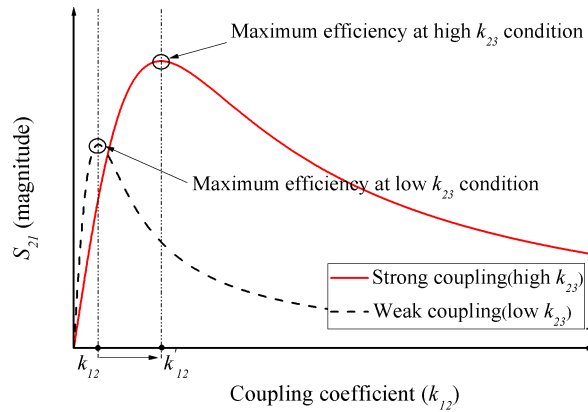
Fig.3.5. $|S_{41}|$ curves versus coupling coefficient k_{12}; red line: strong coupling (high k_{23}), black dot: weak coupling (low k_{23}).

3.1.2.3 Simulation results

With the circuit model of the MR-WPT system, the optimum value of k_{12} can be calculated for a given k_{23}. Fig.3.6 shows the improved system performance efficiency due to the proposed technique derived from the circuit model. This result is verified with an advanced design system (ADS) and high-frequency structure simulator (HFSS), which are appropriate simulation tools for a WPT system around the frequency of interest at 16.47 MHz [3.23]. In the HFSS simulation, the TX coil is a helical structure with a diameter of 8 cm, 10 turns, and a 0.4-mm pitch between lines. The RX coil is a helical structure with a diameter of 10 mm, 10 turns, and a 0.3-mm pitch between lines. Lumped capacitances of 17.5 pF and 75 pF are used for the TX and RX, respectively. Initially, resonant frequency for this research was chosen above 1 GHz for smaller inductor size benefit. Even though the initial system with resonant frequency beyond 1 GHz showed reasonable performance in the –parameter analysis with network analyzer [3.24], [3.25], it was not suitable for real power transfer required for capsule endoscopy applications. Because power devices operating near 1 GHz is nearly 10 times much costly than devices operating near 30 MHz. Moreover, passive devices that can operate near 1 GHz with 300 W of power have a much larger form factor size than of passive devices near 30 MHz with 300 W of power. Considering the device size and component price, it was considered much more practical to choose a frequency under 30 MHz. Hence, the resonance frequency for the proposed system is 16.47 MHz. This low frequency is chosen near industrial, scientific and medical (ISM) band of 13.567MHz, which is widely used in WPT technology, and is suitable for transmitting real power up to 300 W.

The maximum efficiency is optimized by changing D_{12}, and the coupling coefficient k_{12} is optimized to the most suitable value. The first setting of k_{12} the value is determined at a TX and RX coil distance (D_{23}) of 15 mm. The proposed MR-WPT system efficiency is improved by 0.67 dB at a distance (D_{23}) of 70 mm and resonance frequency of 16.47 MHz, compared to a non-adaptive MR-WPT system.

(a)   (b)
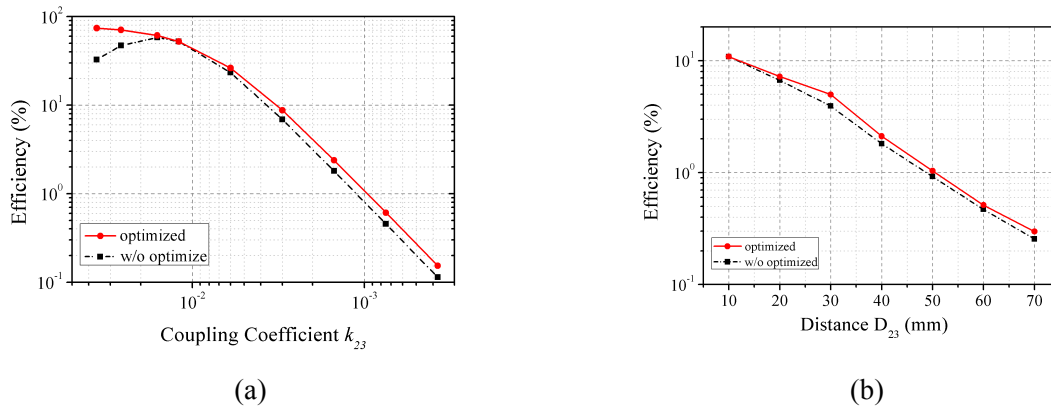
Fig.3.6. Performance of self-resonance coupled wireless power transfer system dependence on: (a) coupling coefficient (k_{23}) varying, and (b) distance between TX and RX coils (D_{23}).

3.1.3 Performance verification

3.1.3.1 Coil characteristics

The coils are made in the form of magnetic resonance structures. The proposed MR-WPT system consists of four coils: a power coil, transmitter coil, receiver coil, and load coil. The coils are made with copper wires. The cross-sectional diameter of the copper wire is 0.32 mm. Two types of transmitter coil structures are implemented. Both are helical structures, one with an 8-cm diameter and 9.5 turns, and the other with a 22-cm diameter and 6 turns. Both transmitters are designed for the same resonance frequency. In biomedical capsule endoscopy applications, minimizing the RX coil size is always the challenge. This is required because of the very limited volume of the capsule device size. The proposed receiver coil diameter is as small as 9 mm, as illustrated Fig.3.7. The RX coil also has a helical structure. Because of the stricter coil size requirement compared to that of the transmitter coil, the low-resonance frequency is not easily obtained by the self-resonance frequency of the coil. Thus, a surface-mounted capacitor of 12 pF is used for the receiver coil. This makes it possible to obtain the appropriate resonance frequency in the receiver coil at a sufficiently small form factor. The power coil is slightly smaller than the transmitter coil, with one turn, while the diameter of the load coil is 8 mm. The measured electrical properties of one of the proposed MR-WPT systems with an 8-cm diameter TX coil, a 9-mm diameter RX coil, a TX power coil, and an Rx load coil are summarized in Table 3.1.

(a)
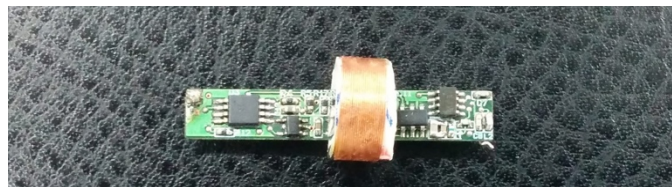
(b)

Fig.3.7. (a) Designed receiver coil with 9-mm diameter, and (b) proposed 9-mm WPT receiver paired with capsule endoscopy board.

Table 3.1. Measured electrical properties of proposed MR-WPT system

TX and power coils			RX and load coils		
Power coil	C_1	1 nF	RX coil	C_3	12 pF
	R_1	0.1 Ω		R_3	1.12 Ω
	L_1	221.5 nH		L_3	7.85 μH
Tx coils (8-cm)	C_2	5.48 pF	Load coil	C_4	1 pF
	R_2	0.9 Ω		R_4	0.11 Ω
	L_2	16.14 μH		L_4	30.5 nH

3.1.3.2 Experimental settings

In 3.1.2, the maximum power transfer condition was analyzed. The proposed method provides a way to track the optimal power transfer condition for the unpredictable movements of the receiver in a patient's GI tract. The coupling coefficient is altered by the distance, axial misalignment, and angle. In this experiment, the proposed method is used for measurements, which are verified over varying values for the distance, axial misalignment, and angle. The scattering parameter is measured using the PNA-X network analyzer N5242A from Agilent Technologies. Three parameters are shown in Fig.3.8: the distance between the TX and RX coils (D_{23}), angle between the vertical axes of the TX and RX coils (θ_{23}), and axial misalignment (A_{23}). The coupling coefficient of k_{23} is affected by these three parameters. With variable parameters, the coupling coefficient of k_{12} can be optimized using manual control. When the value of D_{23} becomes larger, the value of k_{23} becomes smaller. Under this condition, the optimal efficiency is obtained by increasing D_{12}.
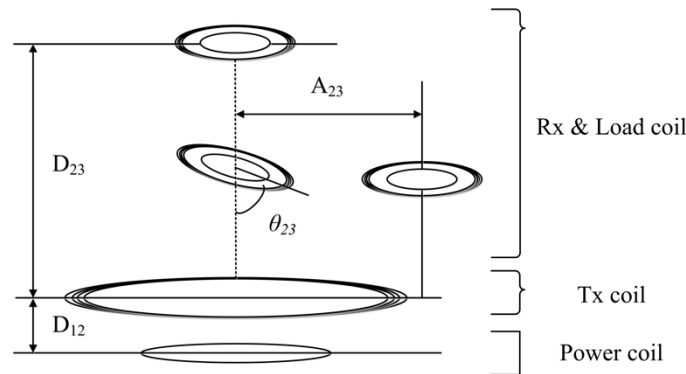
Fig.3.8. Impedance mismatched conditions: (1) between TX and RX coils (D_{23}), (2) angle between TX and RX's vertical axis (θ_{23}), and (3) the axial misalignment (A_{23}).

3.1.3.3 Experimental results

First, an actual power transfer to the load coil is demonstrated. The anterior abdominal wall thickness ranges from 3.5 mm to 62.5 mm, with a 16-mm median value. The gastrointestinal tract is positioned behind a thin part of the anterior abdominal wall, [3.26]. Hence, the distance for the vertical displacement of the proposed system is designed to cover up to 7 cm between the TX and RX coils in order to meet the requirements of conservative cases with an abdominal thickness of 62.5 mm. There is a distance of 7 cm between the human skin surface where the TX coil is located and the RX coil inside the GI tract. The resonance frequency of the TX and RX coils is designed to be 16.47 MHz. An LED is integrated at the end of the load coil. The transmitted power is 158 W, while the received power is measured at 26 mW, as illustrated in Fig.3.9.

In 3.1.2, it was shown that S_{41} is a function of the coupling coefficient k_{12}. The first experiment was performed by varying D_{23}. The S_{41} data were measured while D_{23} was varied from 10 to 100 mm, as illustrated in Fig.3.8. The overall efficiency was degraded with an increase in D_{23}. The fi rst optimized point was set at 10 mm. After a change in D_{23}, the optimum D_{12} was applied. Thus, the optimized point was found, as shown in Fig.3.10(a). The improvement in efficiency was increased from 27.79 to 32.43% (0.67 dB) at 20 mm. The improvement in efficiency was increased from 9.4×10^{-2} to 1.65×10^{-1}% (2.45 dB) at 100 mm. This experimental result is in agreement with the simulation result illustrated in Fig.3.6.

In Fig.3.10(b), the measured S_{41} data with θ_{23} varied from $-90°$ to $90°$ at a distance of 70 mm are demonstrated. The varied D_{12} was applied to track the optimal transfer efficiency. The improvement in efficiency was increased from 0.55 to 0.71% (1.1 dB) at $-15°$. The improvement in efficiency was increased from 3.6×10^{-3} to 8.1×10^{-3}% (4.69 dB) at $-90°$.

In Fig.3.10(c), the measured S_{41} data with the axial misalignment A_{23} varied from -50 mm to +50 mm at a 70-mm vertical displacement (D_{23}) are demonstrated. The improvement in efficiency was increased from 6.5×10^{-1} to 7.1×10^{-1}% (0.49 dB) at 10-mm. The improvement in efficiency was increased from 5.2×10^{-2} to 7.3×10^{-2}% (1.48 dB) at -50-mm axial misalignment.
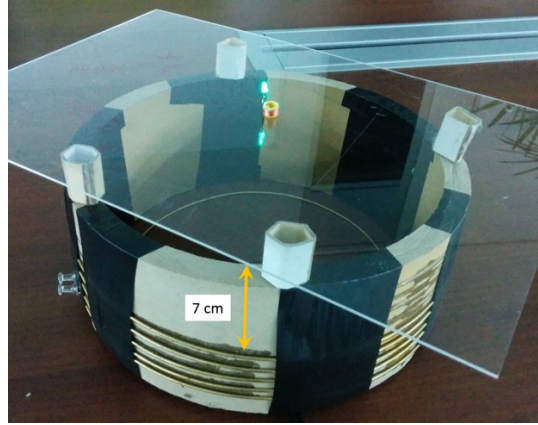
Fig.3.9. Working prototype demonstration: power transfer from power coil to 9-mm diameter load coil with LED at 7-cm distance.

(a)

(b)

(c)
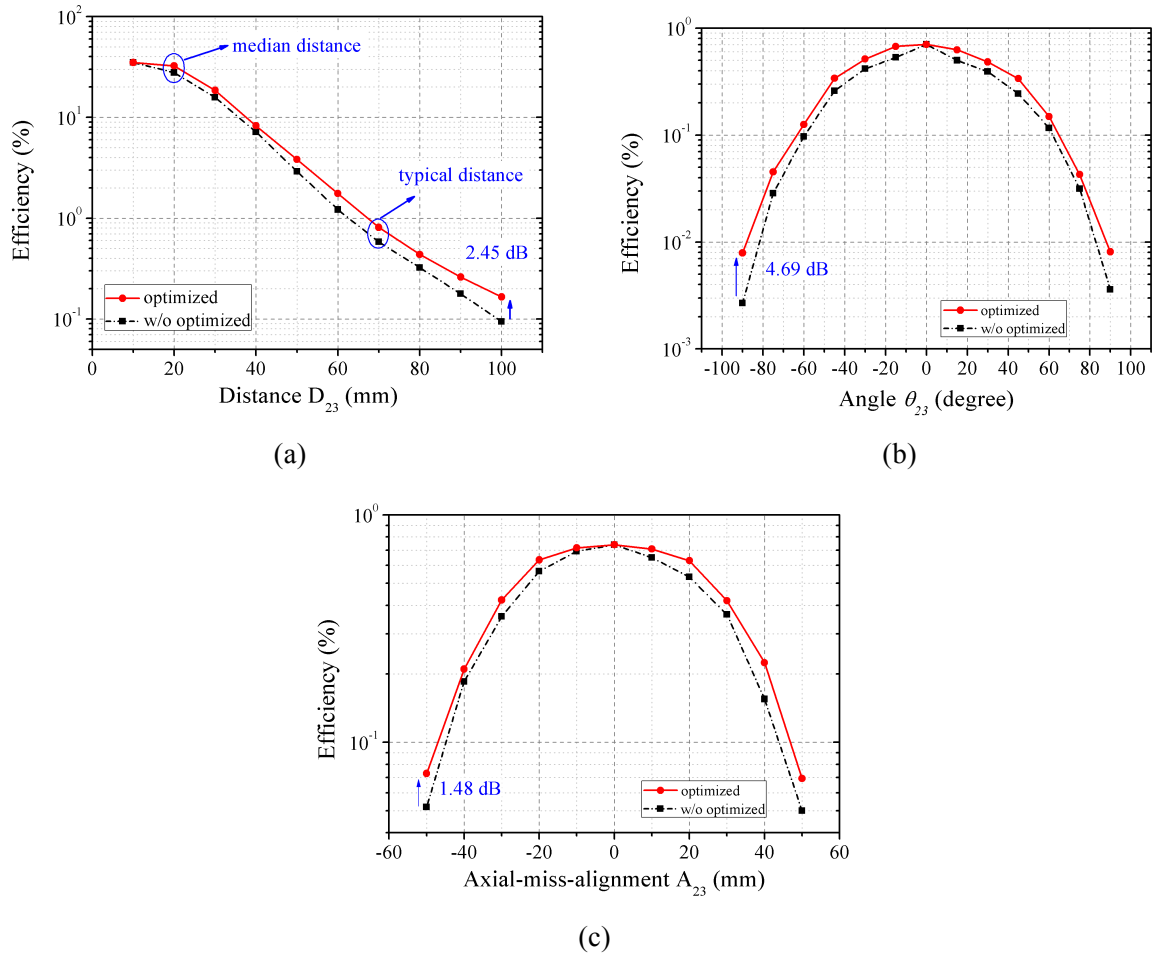
Fig.3.10. Measured performance of the proposed work: (a) D_{23} versus S_{41} graph w/o optimize and w/ optimize, (b) θ_{23} versus S_{41} graph w/o optimize and w/ optimize, and (c) A_{23} versus S_{41} graph w/o optimize and w/ optimize of resonance coupled wireless power transfer system.

3.1.4 Safety check

3.1.4.1 Experimental results of effect on real tissue

During the research on the MR-WPT system for biomedical applications, there were many issues regarding the transfer efficiency through real tissue. Based on the electromagnetic theory, a time-variant magnetic flux can induce a current through a conducting material. The conductivity of real tissue is negligible compared to metal, and hence should not affect the transfer efficiency. Fig.3.11 shows the human body channel model developed for a frequency range of 40 Hz to 110 MHz [3.27], along with the simulation results using this model. The results show a 0.394-dB difference at the maximum point, which is equivalent to a 6.4×10^{-2}% decrease. Fig.3.12 illustrates the experimental setup to determine the penetration through biological tissue using a pork chop. The distance between the TX and Rx coils was 7 cm. The RX coil was deep inside the pork chop, and there was no path without going through the pork tissue. Fig.3.13 shows the measured efficiency result of the penetration experiment through the pork chop at the same distance, angle, and axis-alignment. As shown in Fig.3.13, the maximum transfer efficiency was almost the same; it had only a 0.390-dB difference, which was equivalent to a 6.2×10^{-2}% decrease. This experimental result is consistent with the channel model simulation result.

In order to further demonstrate the safety to the human body, thermogram images were taken to check the energy loss dissipated as heat. Fig.3.14 shows the monitored temperature change in the biological tissue for the worst case scenario, which was measured with a 22-cm diameter TX. After a power transmission for 1 h at a distance of 0 cm, there was no change in the temperature of the biological tissue, which was well below the 1.0 ℃ safety guideline. These results show the possibility of using the proposed MR-WPT system for biomedical applications.
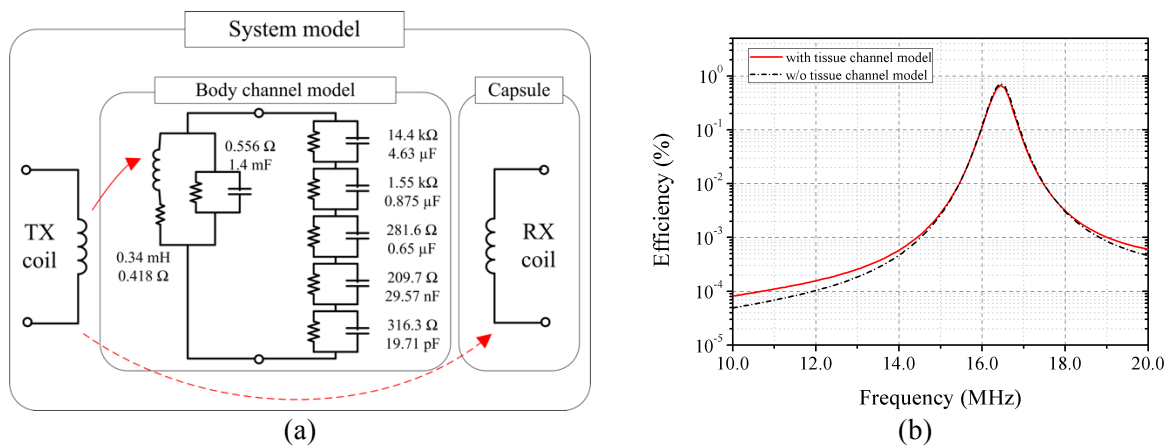
Fig.3.11. (a) Human body channel model, and (b) simulation results.
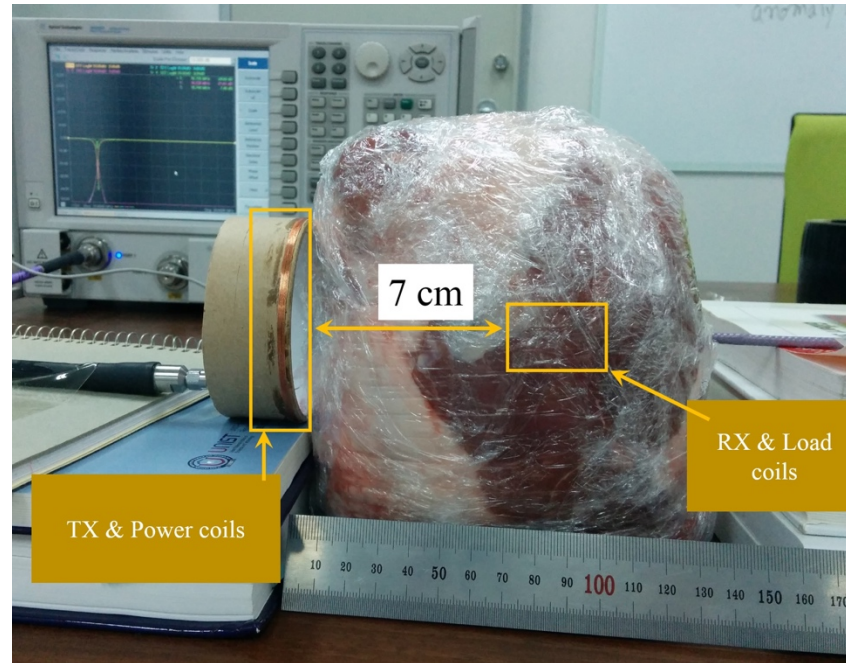
Fig.3.12. Penetration experiment setting with pork chop.
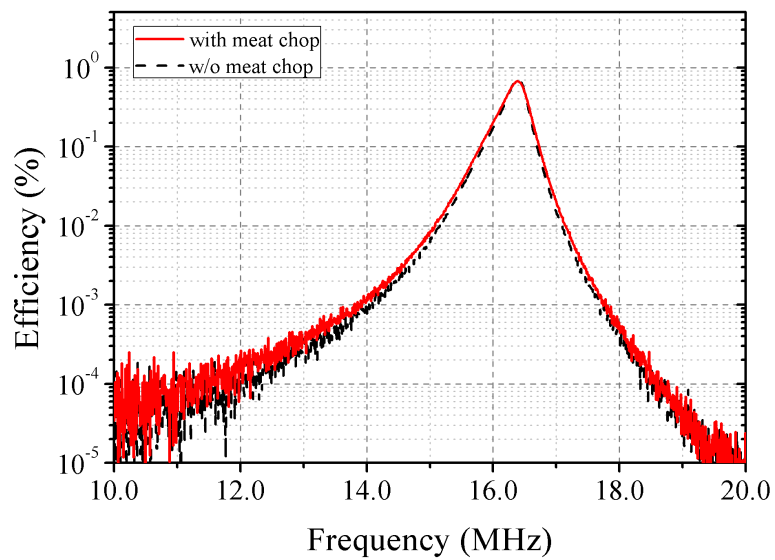
Fig.3.13. Measurement results of penetration experiments through real biological tissue at 7-cm distance.

(a)
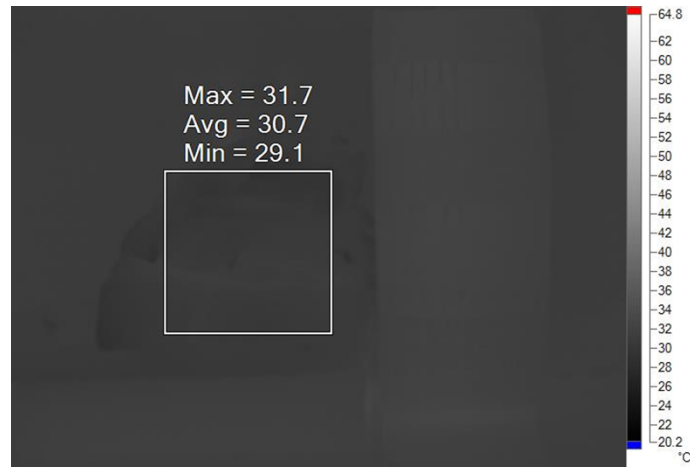
(b)

(c)

Fig.3.14. Thermogram of 22-cm diameter TX with 7-cm distance to biological tissue: (a) visible light image, (b) before power transmission, and (c) after 1-hour power transmission.

3.1.4.2 Verification on SAR

For biomedical applications of electro-magnetic (EM) field generating devices, the EM field absorption in the body has to be satisfied. The SAR is a measure of the rate at which energy is absorbed by the human body, defined as W/kg. If the SAR becomes too high, it can cause harm to the human body. At a frequency range of 1 Hz to 10 kHz, the EM field stimulates the nerve cells. At a frequency range of 100 kHz to 10 GHz, the absorbed EM energy causes a temperature increase in a human.

Thus, many countries and organizations set restrictions of 0.08 W/kg to the whole body, 1.6 or 2 W/kg to the head/trunk, and 4 W/kg to the arm/leg at a frequency range of 100 kHz to 300 GHz. If the whole human body is exposed to a strong EM field, the temperature increase becomes more severe. Thus, the restriction is stricter than the partial absorption rate [3.28]–[3.31].

Therefore, the SAR was estimated for the proposed MR-WPT system using the HFSS simulation tool. The human body was modeled with water. Fig.3.15 shows the 3-D graph produced using the SAR analysis results, where Fig.3.15(a) indicates the positioning of the TX coils and RX coils. The RX and load coils are cylindrical shape capsule models, which are covered by water. In the SAR analysis, the efficiency of the system was 0.2% (-27dB) at a 7.3-cm distance. The transmitting power from the TX was 150 W, and 300 mW of energy was received at the load coil. The maximum SAR value was very small at 1.74 W/kg. A smaller amount of energy compared with the restriction was absorbed in a limited area of the human body. Thus, the safety of the proposed MR-WPT system in the human body was confirmed.

<div align="center">(a)   (b)</div>
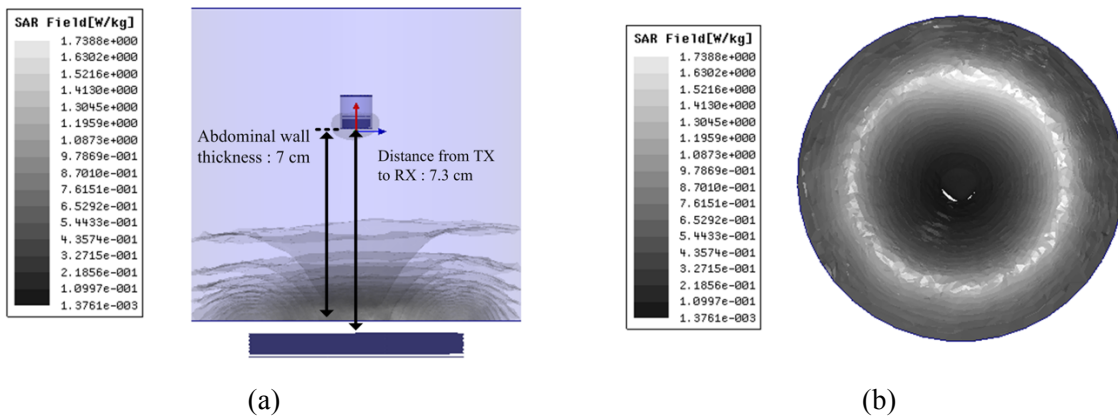
Fig.3.15. 3-D graph of specific absorption rate (SAR) for the proposed MR-WPT system: (a) side-view, and (b) bottom view.

3.1.5 Conclusion

In this section, a new method to track the optimal efficiency of an MR-WPT system suitable for biomedical capsule endoscopy application was presented. The theoretical proof was followed by the results of simulations and measurement experiments. Since capsule endoscopy require a small form factor, a 9-mm diameter receiver with a 16.47-MHz resonance frequency was designed, and the performance was measured. In order to track the efficiency while the receiver was in the GI tract with variations in the distance, angle, and axial-misalignment to the transmitter, a new adaptive method was proposed. This adaptive technique utilizes the coupling coefficient k_{12}. In the distance change situation (D_{23} between the TX and RX coils), the efficiency was increased by up to 2.45 dB with the proposed work. In the angle change situation (θ_{23} between TX and RX coils), the efficiency is increased up to 4.69 dB. In the axial misalignment case, (A_{23} between TX and RX coils), the efficiency was increased by up to 1.48 dB. It was demonstrated experimentally that the proposed MR-WPT system for capsule endoscopy applications is able to track the optimal efficiency under various geometric factors while transferring a real power of 26 mW to the load at a distance of 7 cm.

Since the proposed work is intended for biomedical application, penetration experiments through real biological tissue were performed. There was minimal effect on the efficiency when the receiver and load coils were tested inside a tissue block at a depth of 7 cm, with a degradation of only 0.39 dB. The SAR test showed a very low value of 1.74 W/kg, with an energy transfer condition of 300 mW to the load. This confirmed the safety of the proposed MR-WPT system for use in a human body.

3.2 Step-charging technique for Li-ion battery charger

3.2.1 Background

Inductive power transfer (IPT) technology enables contactless energy transfer between two resonators through a magnetic field. IPT is a promising method of powering electrical devices, especially in environments where wired charging is inconvenient or even dangerous. For IPT applications, enhancing the power transfer efficiency is a key priority, as various research has been conducted to improve the transfer efficiency. Recently, IPT applications are being applied to electrical vehicles [3.32-3.35], biomedical implantation [3.36-3.38], and portable devices [3.39-3.41].

The electrical devices used in an industrial environment are generally powered by batteries, conventionally charged through wires. Conventional wired charging systems are susceptible to harsh environments, especially when exposed to water or dust. Also, in work places like manufacturing plants and construction sites, these wires can be cumbersome, inconvenient and hazardous, which has resulted in a demand for a highly-efficient and reliable alternative charging technology. IPT technology has been shown to transfer energy wirelessly in a range of up to about ten of centimeter with high efficiency. IPT charging systems are also more durable in harsh environments because there are no exposed terminal connectors. IPT technology can provide efficient, safe and convenient battery charging for electrical devices without direct electrical connection. Thus, IPT charging is beneficial for electrical devices in industrial environments including industrial power tools.

The most commonly used rechargeable battery in electrical devices is the Li-ion battery because of its high capacity, which requires constant current (CC) and constant voltage (CV) charging modes, regardless of load variation, to extend battery lifetime. Conventionally, a wired battery charger is composed of a dc-dc buck converter to step down high input voltage to an appropriate voltage level for battery charging, and a charging circuit to regulate charging current and charging voltage. In IPT battery charging, charging power is controlled by DC-DC converter in front of the battery [3.42, 3.43], or power is controlled by using frequency modulation and regulator at the same time [3.44]. Another approach is to eliminate the Fig. 1 Proposed IPT block diagram with battery charger in receiver power stages in front of the battery and implement CC/CV modes using a special topology in order to improve the power transfer efficiency [3.45, 3.46].

In [3.42, 3.43], since the dc-dc converter controls the power, a separate communication circuit for power control is not necessary, but the efficiency is reduced due to the additional power stage circuit. Also, when the charging is completed, the transmission of power from the primary side must be stopped, so a communication device for that is needed. In [3.44], a frequency modulation (FM) and LDO regulator type battery charger is used to control the power. It is more efficient in power transfer than the previous method, but there is always a drop-out voltage in the LDO regulator and it causes

the secondary side to generate heat. Another widely used approach is the topology switch. Work in [3.45], hybrid topologies compensation structure was proposed to supply CC and CV output. A series-series (SS) or parallel-parallel (PP) was used to realize CC mode in impedance matching conditions with zero phase angle (ZPA). A series-parallel (SP) or parallel-series (PS) was used to realized CV mode in impedance matching conditions with ZPA. To implements CC/CV modes, topology switching was used. In [3.46], CLC-LCL and CLC topology were used to obtain CC and CV modes charging states. These techniques do not require feedback control. However, the two technologies can only be realized with exact impedance matching. The topologies must have well matching impedance conditions to have load-independent operation, which is considerably difficult to realize in real systems.

This study presents a step-charging technique for CC and CV modes battery charging with low-cost control system in Inductive power transfer system for a power tool application. The block diagram of the proposed IPT system is shown in Fig.3.16. The proposed IPT system has three power stages, two rectifiers and a half-bridge inverter. The theoretical derivation of the charging frequency

is explained according to the battery charging condition, and the algorithm for applying the battery hysteresis is introduced. Using the proposed step-charging technique, a highly efficient and cost-effective battery charging IPT system is realized.
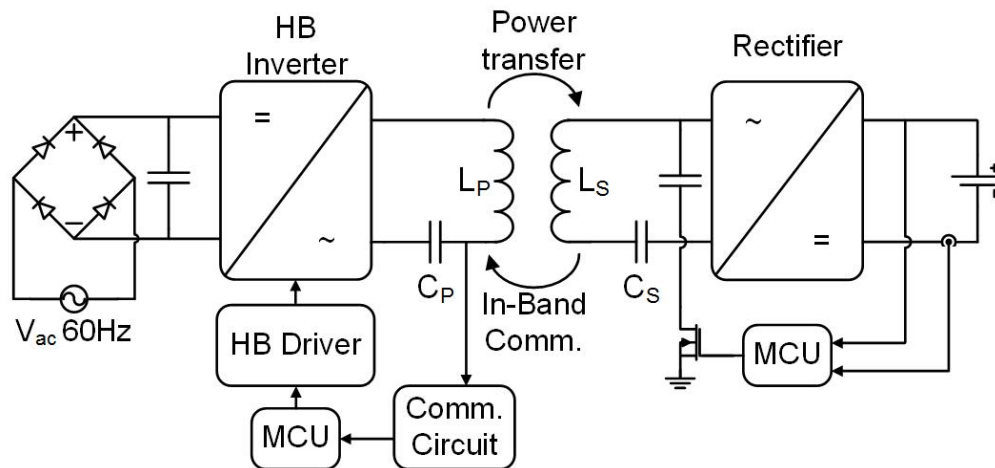
Fig.3.16. Proposed IPT block diagram with battery charger in receiver.

3.2.2 Frequency modulation for CC and CV modes
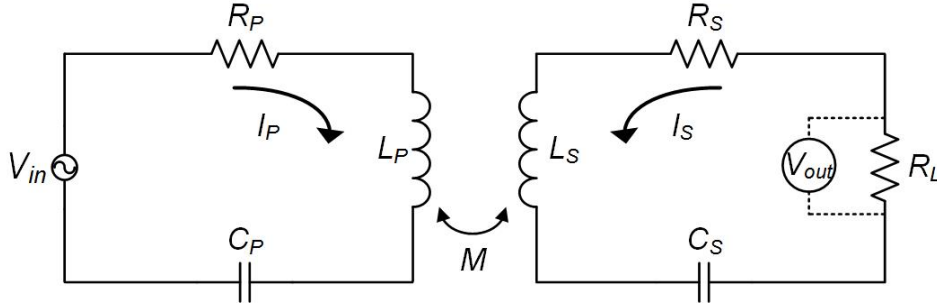
Fig.3.17. Equivalent circuit of series-series compensated IPT.

For the proposed system, SS compensation is used because of its simple structure and the voltage step-down characteristics compared to the SP, PS and PP compensation topologies. An equivalent circuit of the SS compensated IPT system is shown in Fig.3.17. The circuit can be used to obtain load current of the network with respect to switching frequency f. The relationship the voltage applied to the primary coil and between the currents through each coil can be expressed using following matrix.

$$\begin{bmatrix} V_{in} \\ 0 \end{bmatrix} = \begin{bmatrix} Z_P & j\omega M \\ j\omega M & Z_P \end{bmatrix} \begin{bmatrix} I_P \\ I_S \end{bmatrix} \tag{3.12}$$

where Z_P and Z_S are the loop impedances of primary and secondary sides without coupling. These terms can be expressed as follow:

$$Z_P = j\omega L_P + \frac{1}{j\omega C_P} + R_P \tag{3.13}$$

$$Z_S = j\omega L_S + \frac{1}{j\omega C_S} + R_S + R_L \tag{3.14}$$

where R_P and R_S are the parasitic resistance of primary and secondary side, R_L is the equivalent resistance of the Li-ion battery, L_P and L_S are the inductance of primary and secondary side coils for power transfer, and C_P and C_S are the resonance capacitance of primary and secondary side. Also, ω is the angular frequency $2\pi f$. To obtain the voltage gain, equation (3.12) can be expressed as:

$$V_{in} = Z_P I_P + j\omega M I_S \tag{3.15}$$

$$I_P = -\frac{Z_S}{j\omega M} I_S \qquad (3.16)$$

In equations (3.15) and (3.16), I_S can be replaced by $V_{out}=R_L$. The voltage gain obtained from the above equation is expressed as follows:

$$G_V = \left|\frac{V_{out}}{V_{in}}\right| = \frac{\omega M}{Z_P Z_S + \omega^2 M^2} R_L \qquad (3.17)$$

where V_{in} is input voltage at the primary side, V_{out} is the output voltage at the secondary side, and M is the mutual inductance of L_P and L_S. Since there is a rectifier with a capacitor filter, which acts as an impedance transformer, R_L can be modified as an equivalent ac resistance R_{L-AC}, which is introduced in [3.47-3.49]. The load resistance can be replaced by R_{L-AC}, which is expressed according to the battery voltage V_{batt} and the charge current I_{char} as

$$R_{L-AC} = \frac{8}{\pi^2} R_L = \frac{8}{\pi^2} \frac{V_{batt}}{I_{char}} \qquad (3.18)$$

According to (3.17) and (3.18), frequency could be controlled to supply constant current to the battery. Mutual inductance and voltage is given by the position of the coils and battery characteristics. The charging current is predetermined based on the recommended charge current rating for the battery. The optimal frequency can be derived from the following:

$$G_{V\_diff} = G_{V\_freq} - G_{V\_voltage} = V_{batt} \left\{ \left|\frac{8\omega M}{\pi^2(Z_P Z_S + \omega^2 M^2) I_{char}}\right| - \frac{1}{V_{in}} \right\} \qquad (3.19)$$

where G_{V_diff} is the voltage gain difference between the gain according to the frequency (G_{V_freq}) and the desired gain ($G_{V\_voltage}$). The desired gain is determined by the current battery voltage and charging current given by the battery characteristic. Fig.3.18 shows G_{V_diff} according to the normalized frequency. At the $G_{V\_diff} = 0$ condition, we can find the control frequency for the desired current and current battery voltage. The control frequency is calculated by interpolation method. As we can see in Fig.3.18, The control frequency needs to be close to the resonance frequency when the required charging current or current battery voltage becomes high. For the black line in Fig.3.18, the red dash line is when the frequency increases by about 8%, and the blue dash-dot line when the frequency decreases by about 5%. The frequency below the resonance frequency is the capacitive region, where current leads. In this region, shoot-through current at half-bridge inverter switch diode can occur. Because of this, the region above the resonance frequency is used for frequency modulation. Fig.3.19

71

shows charging frequency with respect to the battery voltage. The calculated frequency is extracted from (3.19), assuming input voltage is fixed and the battery charging current is 4 A. The calculated results are wellmatched to measured results, with a maximum 1 kHz difference between the measured and calculated frequency, which is only 0.7% error. This discrepancy is caused by non-idealities in the real circuit containing a half-bridge inverter and other components, which are neglected in the ideal circuit shown in Fig.3.17.
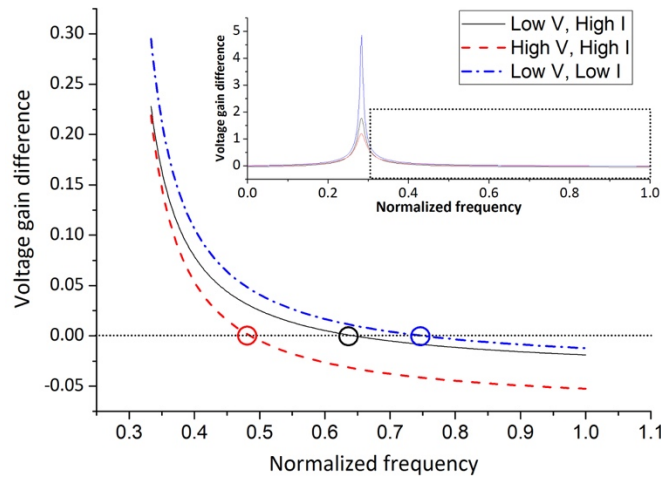
Fig.3.18. Voltage gain difference graph according to the normalized frequency at different voltage and current conditions.
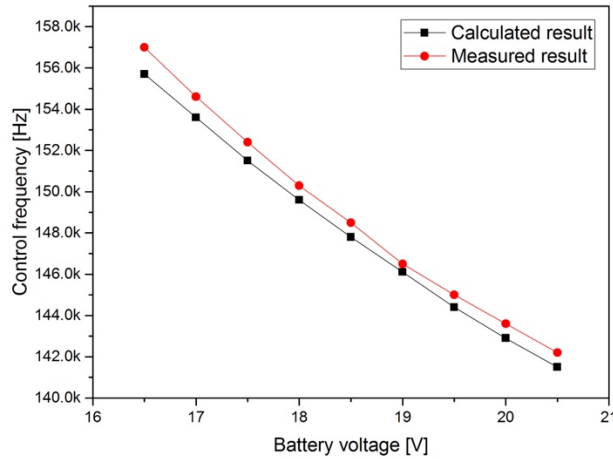
Fig.3.19. Charging frequency according to the battery voltage at fixed charging current condition.

3.2.3 Step-charging technique

3.2.3.1 Li-ion battery characteristics

Rechargeable battery uses CC mode and CV mode to charge. Li-ion rechargeable battery, which is one of the most popular secondary battery, is charged with combination of CC/CV mode. Combination of CC/CV mode is used to maximize battery life time and ensure safety from explosion while charging the battery. To implement CC/CV mode, fundamental characteristic of the battery is used as known as voltage hysteresis. Fig.3.20 shows the voltage hysteresis characteristic of the rechargeable battery. Voltage of battery is slightly lower in discharging condition compared to charging condition. The voltage hysteresis is voltage difference between charging condition and discharging condition. The voltage difference becomes larger when charging or discharging current becomes higher. Fig.3.21 shows voltage hysteresis characteristic in different current. In charging condition, battery voltage is different with different charging current. By modulating voltage hysteresis characteristic, CC/CV modes are realized.
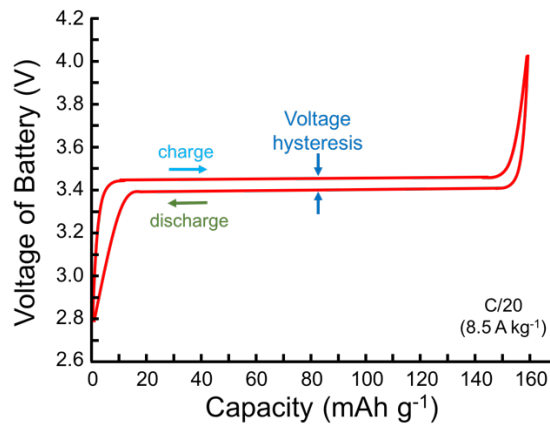
Fig.3.20. Voltage hysteresis characteristics of the rechargeable battery.
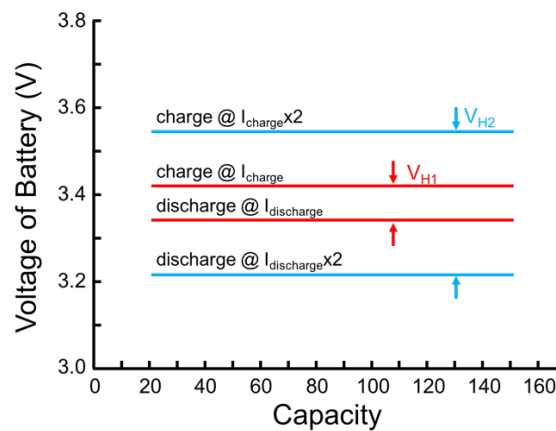
Fig.3.21. Voltage hysteresis characteristics in different charging and discharging current.

3.2.3.2 Step-charging algorithm

The proposed step-charge technique enables the implementation of a battery charging circuit with a simple communication system and minimized feedback control. To implement this technique, operation of the primary and secondary sides has to be synchronized by the algorithm through one-way communication from the secondary to primary side. A flow chart of the algorithm is shown in Fig. 3.22, outlining the procedure for CC and CV mode battery charging. This algorithm is implemented on a low-cost low-frequency-resolution MCU, using a look-up table to determine the control frequency from the measured battery voltage.

Before charging the battery, the primary side sends a ping repeatedly to check if the secondary side coil is properly placed for charging. The primary side can detect the secondary side itself without communication. The detection circuit and explanation will be introduced in section 3.2. The primary side transmits power at the initial frequency f_{int}. In our system initial frequency is 161 kHz The secondary side reads the battery ID and sends this information to the primary side. If the battery ID is of a chargeable type, primary side starts charging. Then, the system checks the battery voltage and sends the calculated frequency data based on (8).

In CC mode, the secondary side reads the battery voltage when I_{char} reaches the minimum current value $I_{out-set\_cc}$, which is selected after considering the frequency resolution of the MCU, and sends feedback data to the primary side to maintain the average current at 4 A. Based on equation (8), the frequency value satisfying the CC mode is found and the power control frequency is changed. A look-up table is used to control this technique. If a large change occurs in the load value, when the amount of current can be deviated from the predicted range, all of the power predicted values in lookup table for a particular frequency will be shifted. This sequence is illustrated in Fig. 23(a). This sequence is continued until the battery voltage reaches 20.75 V, which is fully-charged battery voltage given by the battery profile. When the battery voltage reaches 20.75 V, it switches to CV mode.

In CV mode, the charge current should decrease over time according to the battery conditions. To realize CV mode with an MCU, which can control frequency discretely, a current step-down method is applied, which is shown in Fig. 23(b). The battery exhibits hysteresis, shown as a drop of battery voltage proportional to the charging current. The current step-down method uses the battery hysteresis. In the flow chart, the previous charging current is expressed as I_{out} and the next target charging current is expressed as $I_{out-set\_cv}$, which is set to $I_{out} - 0.25A$. When the battery voltage reaches the maximum acceptable voltage, which is 20.75 V in the target application, the secondary side sends the new frequency data to the primary side to reduce the charging current to $I_{out-set\_cv}$. With the reduced charging current, the charging voltage is decreased below 20.75 V. This sequence continues until the battery charging current reaches the minimum charging current, which is 1 A for the target application.

In addition to the charging procedure, protection is included in the proposed charging algorithm.

The implemented protection programs are over-voltage protection, over-current protection, and temperature protection. For over-voltage and over-current conditions, the charging system shuts off completely. For high temperature conditions, the charging current is reduced for 10 minutes to limit the heat generation.
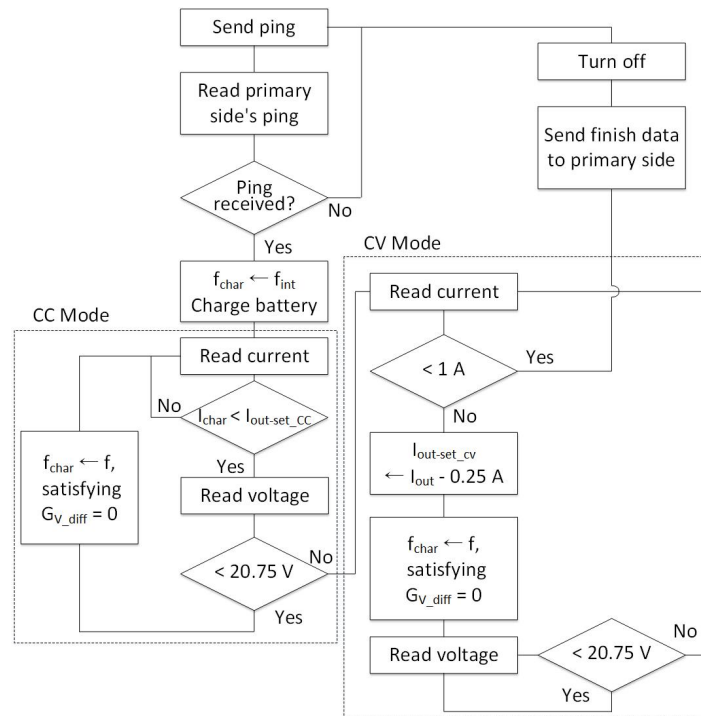
Fig.3.22. Flow chart of the proposed step-charging technique for battery charging system.

(a)

(b)
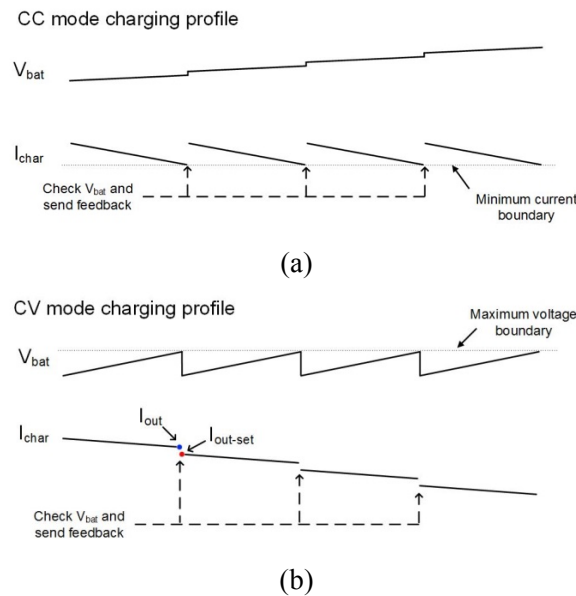
Fig.3.23. Battery charging profiles with proposed step-charging technique: (a) CC mode charging profile, and (b) CV mode charging profile.

3.2.4 System description

3.2.4.1 Transmitter and receiver
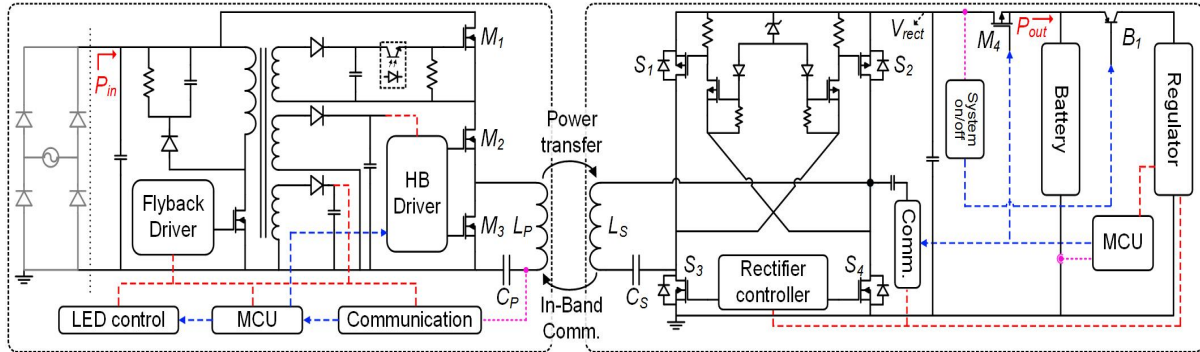
Fig.3.24. Proposed wireless battery charger schematic. (red dot line: low level power line, blue dots line: control line, purple dots line: sensing line)

Table 3.2. Parameters of system

Parameters		Value
Primary side	board size	$14 \times 10 cm^2$
	coil size	$9.5 \times 6 cm^2$
	L_p	264 μH
	C_p	8.2 nF
	V_{in}	311 V_{dc}
	major components	MCU (AT90PWM), Driver IC (IRS2186), Half-bridge inverter (IPP60R230P6)
Secondary side	board size	$9.5 \times 6.5 cm^2$
	coil size	$9.5 \times 6 cm^2$
	L_s	3.1 μH
	C_s	700 nF
	V_{batt}	16-20.75 V
	major components	MCU (AT90PWM), Rectifier (IRFR8314PbF, IPD90P03PAL), Rectifier controller (TEA1795T)

The schematic of primary side and secondary side is shown in Fig.3.24. The hardware of the primary-side board is shown in Fig.3.25(a). The system parameter and components used in the circuit are summarized in Table. 3.2. In input voltage is 311 V, which is rectified voltage rating of 220 V_{rms} at 60 Hz. A fly-back converter with an integrated PWM controller is used to step down 311 V to 5 V and 12 V, which supplies auxiliary power to the MCU, communication circuit and driver. A MCU (AT90PWM) is mainly used to control the operation of the power transfer between the coils. It changes the transfer frequency according to the received data from the communication circuits. A half-bridge inverter is used to drive the primary coil, where the source is the 311-V bus after the full

76

bridge rectifier. Between the full-bridge rectifier and the half-bridge inverter, a MOSFET (M_1) is placed to prevent shoot-through current while changing the driver frequency of the primary coil. The M_1 is needed because gate driving signals for M_2 and M_3 become high when the MCU changes the driving frequency. A MCU (AT90PWM) is mainly used to control the operation of the power transfer between the coils by changing the transfer frequency according to the received data from the communication circuits. The secondary side schematic is also shown in Fig.3.24. The secondary-side board is shown in Fig.3.25(b). The secondary side is made up of a full-bridge active rectifier, regulators, and an MCU. The active rectifier converts transferred ac power into dc power. This active rectification circuit decreases drop-out voltage compared to a diode rectifier from about 700 mV to 100 mV, which increases voltage and power conversion efficiency. The system on/off circuit is triggered when rectified voltage V_{rect} is detected. After checking the signal, the system on/off circuit turns on MOSFET M_4 and BJT M_5 to charge the battery and turn on the MCU. This circuit makes reduce standby power by selectively turning on the MCU. The MCU plays a main role in the receiver as it processes all the monitored data, which are battery voltage, charging current, and temperature. The MCU initially senses the battery identification resistor to determine whether or not the connected battery is compatible with the charging system. After identifying the battery, it monitors the battery voltage and charging current to control the charging state. If the battery voltage and charging current exceed the pre-defined boundary condition, the MCU sends a data to primary side to regulate charging state. In addition, the monitored data are used for over-voltage protection and over-current protection. A thermistor is used for temperature protection. Protections are conducted by controlling primary side with data communication. Fig.3.26 shows the pre-charger and system on/off circuit in secondary side. M_4 and M_5 are connected to each other in the opposite direction. In the turn-off state, only the charging using the resistance path is possible. As mentioned above, when V_{rect} is detected, B_2 and B_1 are sequentially turned on, and power is supplied to the MCU. Since the MCU senses the battery ID and the battery state, and starts power control.

(a)   (b)
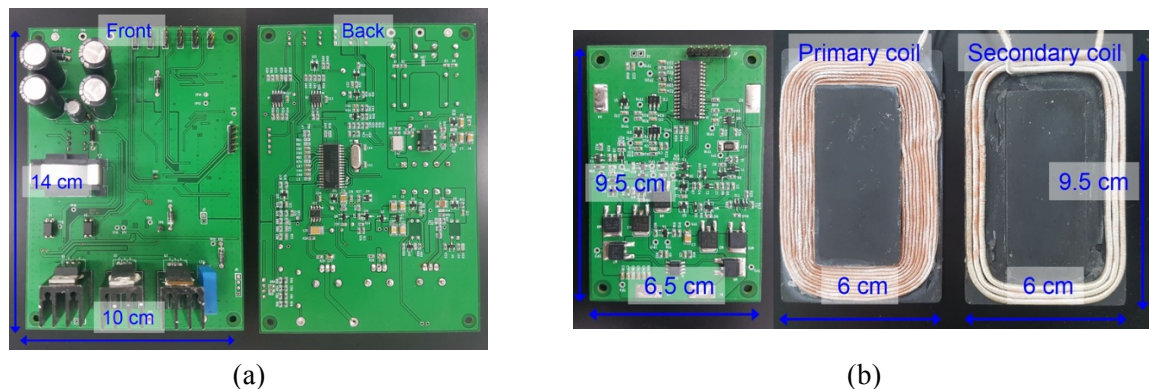
Fig.3.25. Fabricated step-charging technique IPT system: (a) primary side circuit, and (b) secondary side circuit, primary and secondary coils.

Fig.3.26. Pre-charger and system on/off circuit in secondary side. (red dots line: low level power line, blue dots line: control line)
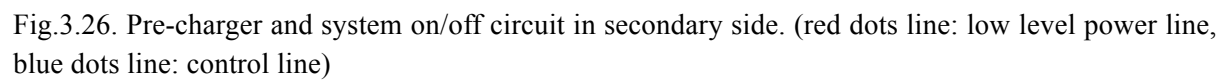
3.2.4.2 Coil characteristics

The primary and secondary coils are shown in Fig.3.25(b). The primary coil is 9.5×6 cm^2 in size and consists 33 turns with a total inductance of 264 μH. The secondary coil is 9.5×6 cm^2 size and consists of 3 turns with a total inductance of 3.1 μH. The gap between primary and secondary coils is 7 mm during power transfer. Fig.3.27 shows measured efficiency from the primary to secondary coils. This was measured with a network analyzer (Keysight E5061B ENA), which supports power transfer efficiency measurements for wireless power transfer applications. The power transfer efficiency is above 95% in the 130-160 kHz range. This result is well-matched with 95.0% - 95.2%, which is the calculated efficiency using efficiency equations in [3.34]. Because of the low-quality factor, the power efficiency is almost constant over a broad frequency range. This characteristic is suitable for the proposed frequency modulation technique.
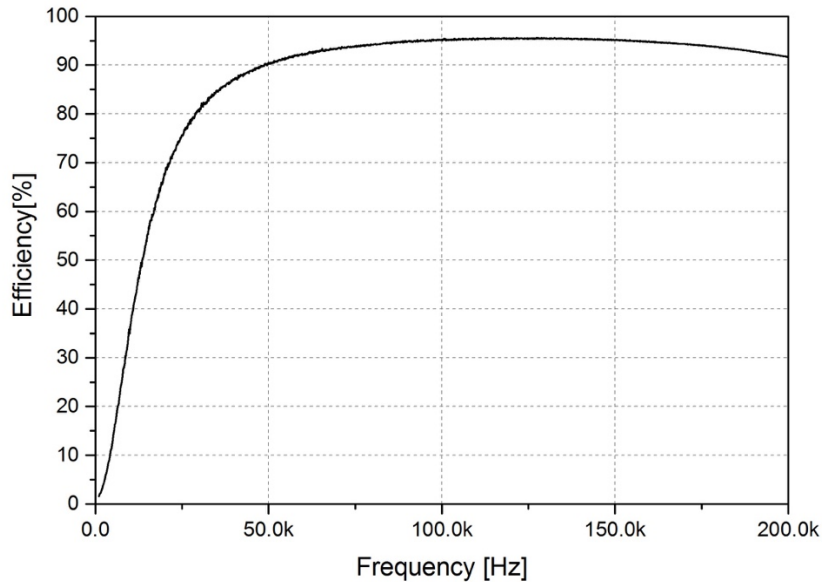
Fig.3.27. Measured efficiencies of primary to secondary coil power transmission.

3.2.4.3 Communication circuits and analysis

The basic concept of in-band communication is introduced in [3.44] used for IPT, but is not widely covered in the literature. In this section, the in-band communication is analyzed using equivalent circuit. Fig.3.28(a) shows the communication circuit of the primary and secondary side, where unidirectional in-band communication is used. The data are transferred from the secondary to primary side. An impedance modulation technique is used for the in-band communication. MOSFETs (T_1, T_2) are connected to L_S and C_S to make a path to C_M and R_M, which changes the impedance of the secondary side. When T_1 and T_2 are turned on, the primary side also senses the impedance change of the secondary side. The voltage between L_P and C_P is changed. During communication, the equivalent circuit is represented as in Fig.3.28(b). The loop impedance of the primary side is the same as (3.13), but the secondary side is expressed as

$$Z_S = j\omega L_S + \frac{1}{j\omega C_S \| C_M} + R_S + R_M \tag{3.20}$$

where C_M is the capacitor for impedance modulation and R_M is the resistance for impedance modulation.

$$I_P = \frac{V_{in}}{Z_P + \frac{\omega^2 M^2}{Z_S}} \tag{3.21}$$

Equation (3.21) is the current I_P of the primary side. The voltage of C_P can be expressed as

$$V_{CP} = \frac{1}{\omega C_P} I_P \tag{3.22}$$

(a)　　　　　　　　　　　　(b)
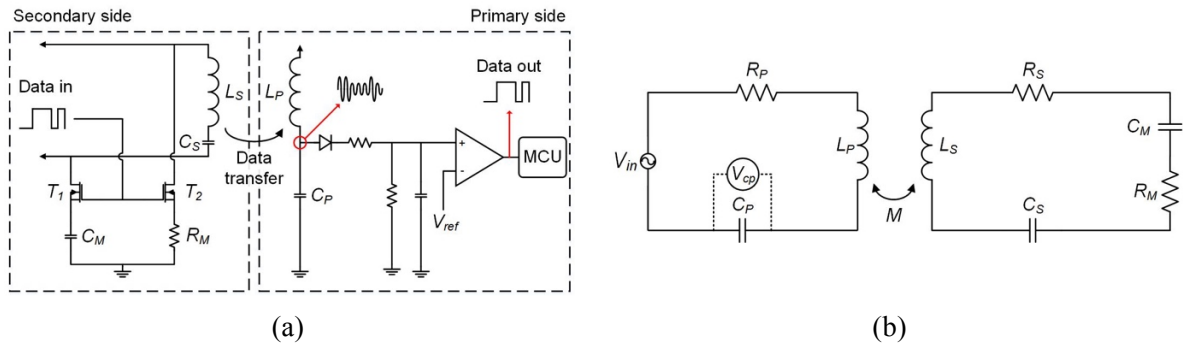
Fig.3.28. In-band communication circuits: (a) block diagram, and (b) equivalent circuit.

Based on (3.21) and (3.22), the voltage results of the C_P over frequency are shown in Fig.3.29. The top black line shows V_{CP} without data transferring. The bottom red line shows V_{CP} with data transferring. These high voltage signals are rectified and stepped down to below 5 V. Then, a voltage comparator is used to restore the data and send it to the MCU. The V_{ref} is set to 2.4V, which is chosen to operate in the full frequency operating range, to recover the data with the comparator. The voltage difference makes data recognizable. With this communication technique, the secondary side can send data immediately when an event occurs. Fig.3.30 shows the measured results during communication. The blue line (top trace) shows the sending data signal from the secondary side. Since in-band communication is performed while the primary side still tries to transfer power, some noise is observed in the sending signal. The light blue line (middle trace), shown in the middle of Fig.3.30, is the voltage between L_P and C_P. The yellow colored line (bottom trace) is the recovered data at the primary side. Even with some noise on the sending side, the restored date on the primary side is accurately received. The time required for communication is about 5.6 ms per one communication. In addition, the communication circuit is used to sense the secondary side, which causes the impedance to the secondary side coil and the ferrite to fluctuate and V_{CP} to decrease. This is less change than the influence in the communication, and communication is designed considering this influence.
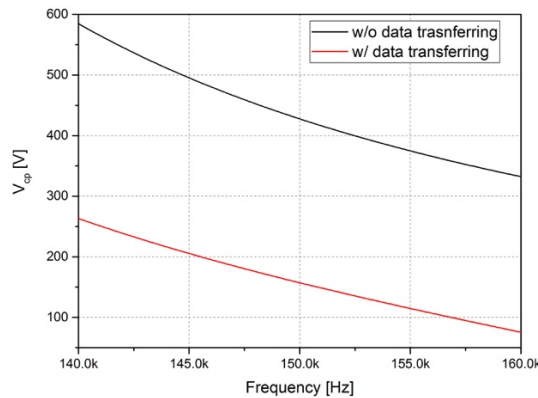
Fig.3.29. Voltage of the C_p when communicated dependence on frequency.
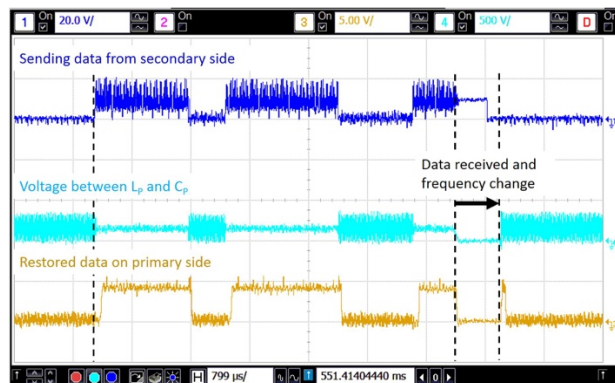
Fig.3.30. Measured communication signals at primary and secondary sides.

3.2.5 Performance verification

3.2.5.1 Experimental settings

Fig.3.31 shows the experimental setup of the proposed wireless battery charger. The proposed system is measured using a power supply (Kikusui PCR2000LA), electric load (Kikusui PLZ334W), oscilloscope (Lecory HDO4000A, Kesight MSO9254A), and power analyzer (N4L PPA520). The input voltage of the system is 311 V, which is the rectified voltage rating of the 220 Vrms. A 5S2P Li-ion battery (5 cells in series, 2 cell strings in parallel) is used as the battery.
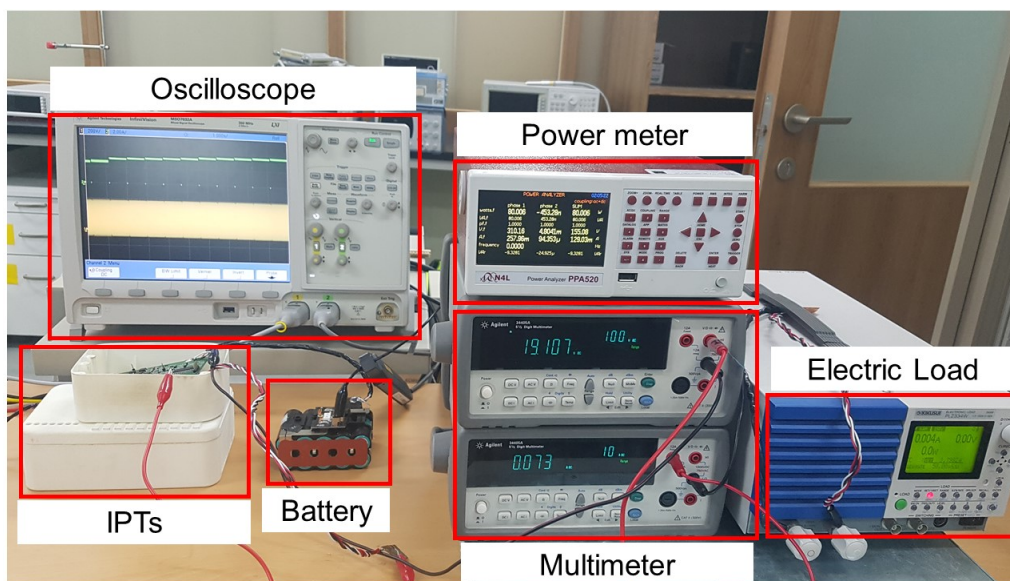
Fig.3.31. Experimental setup.

3.2.5.2 Experimental results

Fig.3.32 shows the battery charging waveforms of the proposed wireless battery charger in the time domain. The top pink line indicates charging voltage, and the bottom yellow line indicates charging current. Total charging time is 62 minutes. During the total charge time, the secondary side transmits 8 bits of communication data about 100 times, and if there is any other error, it tries additional communication. The total communication time is 560 ms, which is 0.015 % of the total charging time. Around 8 W of power is consumed during communication, about, but the time required for communication is very short and there is almost no power loss. The average charging current is 4 A in CC mode. The transfer frequency is determined by the proposed algorithm and controlled discreetly with the MCU. The transfer frequency range is 142-162 kHz. The current decline is caused by the step-charging control of the frequency. After the system detects the battery voltage at 20.75 V, CV mode starts. In CV mode, the charging current is reduced by 0.25 A per step. Fig.3.33 shows the measured power transfer efficiency, charging current, and charging frequency over the output power range. The efficiency is measured from the dc input power P_{in} to the battery charging power P_{out}, which is indicated in Fig.3.24, such that efficiency is $\eta = P_{out} = P_{in}$. Fig.3.33(a) shows the charging efficiency of the system under CC mode at 4-A charging current. The average efficiency is 89.5% under 66-87 W charging conditions. In CC mode, the voltage of the battery increases with the charging power. The maximum efficiency is 90.3% under a 68-W charging condition. This includes 3W of power consumption of MCUs and communication circuitries. The power transmission efficiency of the power stage alone is about 93%. This is a very high power transfer efficiency considering that the coil-to-coil efficiency is about 95%. Fig.3.33(b) shows the charging efficiency of the system under CV mode with the battery voltage at 20.75 V. The maximum and minimum efficiencies in CV mode are 89.7% and 68.3%, respectively. Table 3.3 shows the performance comparison of existing wireless power transfer systems for battery charging applications [3.34, 3.37, 3.42-3.44, 3.50, 3.52]. The implementation of this IPT battery charging system focused on cost effectiveness for close-distance charging, while maintaining high efficiency. Some of the other works outlined in Table3.3 uses sophisticated wireless communication modules or higher-performance controllers (DSP) that increase the system cost. Conversely, this work used a low cost MCU for control using in-band communication that does not require additional wireless communication modules. Although [3.34, 3.51] achieved higher end-to-end efficiency, their power levels were significantly higher and the controllers were much costly. Compared to the remaining works with lower-cost implementation, the proposed IPT system achieved a higher efficiency (90.3%). In addition, the technology of this study can be increase the power control range when combined with technologies such as [3.52], which is control the power and voltage with primary side DC-DC converter.
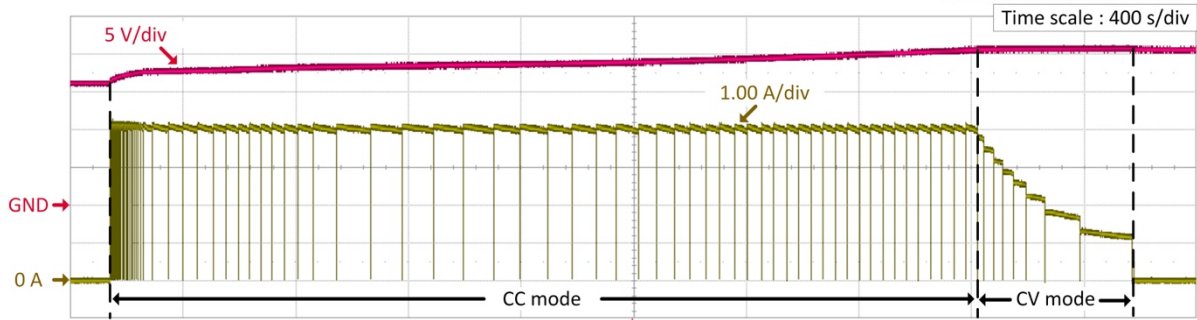
Fig.3.32. CC/CV mode battery charging profiles in time domain.
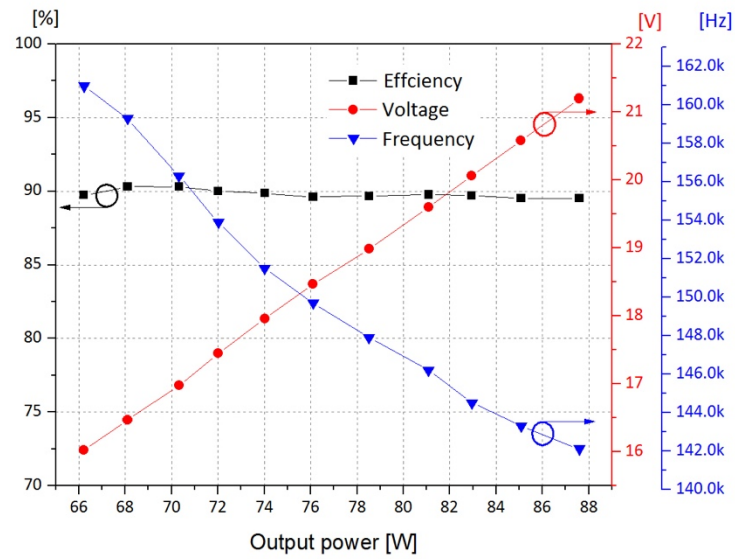
(a)
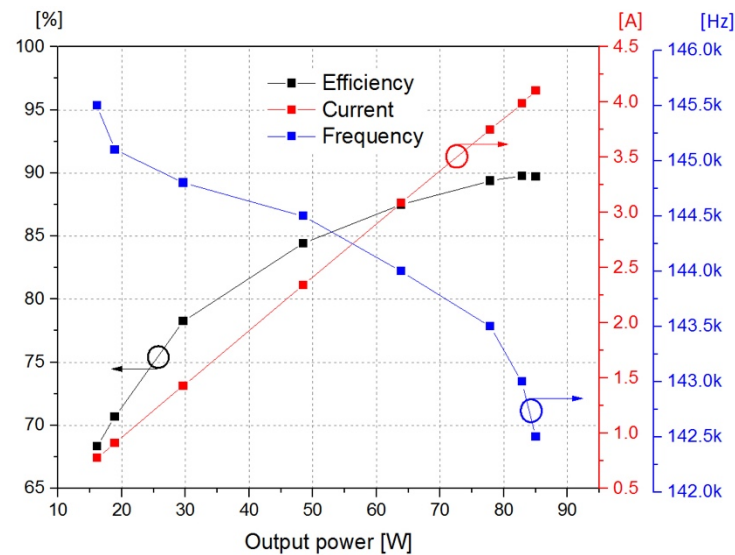
(b)

Fig.3.33. Charging efficiency profiles with transfer frequency and battery voltage or charging current: (a) CC mode profile, and (b) CV mode profile.

Table 3.3. Performance comparison

| | Distance | Efficiency | Power | System feature | | | |
				Controller	Comm.	Power ctrl.	Integration
[3.34]	8 cm	96%	4 kW	DSP	Wireless	Freq. modulation	-
[3.37]	1 cm	80%	15 W	-	Wireless	Freq. modulation	-
[3.42]	10 cm	84%	560 W	MCU	Wireless	DC-DC converter	-
[3.43]	On pad	63%	2.5 W	On-chip	In-band	-	On chip (RX)
[3.44]	On pad	84%	15 W	On-chip	In-band	Freq. modulation	Full system
[3.50]	11 cm	50%	20 W	PWM IC	-	Load modulation	-
[3.51]	10 cm	94.5%	1.5 kW	DSP	Wireless	Topo. Compensation	-
This work	0.7 cm	90.3%	80 W	MCU	In-band	Freq. modulation	Full system

3.2.6 Conclusion

This paper presented a step-charging technique to regulate battery charging voltage and current with minimized power stages, achieving maximum 90.3% end-to-end efficiency. Previous studies using a conventional frequency modulation require high resolution frequency control, but this method is difficult to apply to low-end products such as power tools. To solve this problem, we analyzed the power control method of the system and designed the algorithm to charge the battery with the step-charging technique. The proposed step-charging technology enables CC/CV modes power control with low-resolution frequency modulation using battery hysteresis. The hardware implementation is designed for an 80-W IPT power tool charging system. To minimize cost, a low performance MCU is used to control the entire IPT system and in-band communication is adopted. The experiment verifications were performed to confirm effective operation of the step-charging technique. The experimental results confirm that the feedback signals from the secondary to primary side are minimized during battery charging condition to reduce disturbances in the charging current. The experimental results show the power transfer efficiency, algorithm test and full battery charging graph in the time domain. Compared to previous works, the proposed frequency modulation technique for IPT allows for lower-cost implementation while maintaining high efficiency.

3.3 Instantaneous power consuming level shifter for body implantable buck converter

3.3.1 Background

Wireless power transfer has been widely used for body implantable medical device to address power supply problem. However, there are concerns regarding the implant location. The size of an implantable system with a wireless power receiving coil should be sufficiently small to fit in the location [3.53]-[3.55]. The coupling coefficient is proportional to the ratio of the size of the power receiving coil and power transmitting coil [3.56]. Therefore, coupling coefficient in the body implantable device is usually extremely low [3.53]. In extremely low coupling condition, voltage gain is susceptible to the implant depth [3.55]. Since the thickness of the skin varies for each person, the received voltage of the receiver varies a lot for each person. Therefore, a DC converter is needed to provide stable power even when the implant depth varies in extremely low coupling condition.

A switching converter is more efficient than a linear converter in a wide voltage conversion ratio condition. Therefore, a switching converter is preferred as DC converter in a wireless power transfer system for body implantable applications [3.57]-[3.59]. This converter type uses many external components such as inductor, storage capacitor, bootstrap cap, and components for the compensation circuit. The use of many external components should be avoided in body implantable medical devices as these increase the size of the device. The inductor and storage capacitor are essential components of a switching converter and cannot be removed. The switching converter for the body implantable device operates in discontinuous mode (DCM) since the device is operated at low power [3.60]. In DCM, the number of components for the compensation circuit can be further reduced and integrated on the chip so that such components are not used as external components. To remove bootstrap capacitor, the level shifter should be the only component of the driver for a high-side power switch. However, the level shifter is always-on circuit and its high power consumption when it is used in a driver degrades power conversion efficiency.

In this section, a low power level shifter for buck converter is proposed as a high-side power switch driver for wireless power transfer in body implantable medical devices. The external bootstrap capacitor was eliminated and only the level shifter was used as driver to reduce the overall size of implantable devices. Low power consumption was achieved by consuming power instantaneously during the transition period. Two types of on and off circuits were realized to cover the wide input range.

3.3.2 Conventional switching converter drivers

A driver circuit is used to operate the power MOS switch of a DC converter and class D amplifier. A taper buffer with scale factor that is proportional to the input capacitance to output capacitance ratio is generally used as driver [3.61]. The taper buffer is made up of an inverter chain. However, if the input voltage of the converter is greater than the driving voltage of the buffer, the buffer alone will not be able to drive the power switch. Several driver techniques can be applied for high input voltage such as using a bootstrap capacitor, using a high-side ground, and using a standalone level shifter.

3.3.2.1 Bootstrapping

The most popular method to drive a high-side MOS switch is using a bootstrap capacitor. Bootstrapping is used when the high-side MOS switch is an NMOS. The principle of bootstrapping is charging the voltage to drive the MOS switch to the capacitor using a diode and operating the low-voltage taper buffer using the charged voltage. The cathode of a bootstrap capacitor is connected to the source of a high-side MOS switch to realize an identical reference. Since the reference voltage is the same, the voltages of the bootstrap capacitor and taper buffer swing together with the high-side MOS switch. The driving signal is provided by the level shifter. The advantages of using bootstrapping is that it uses an NMOS as a power switch. An NMOS has a lower on-resistance compared to a PMOS, which has a low conduction loss. Also, driving loss is low because input capacitor is smaller within identical on-resistance. Bootstrapping can be applied whenever the supply voltage varies. However, a bootstrap capacitor cannot be integrated on a chip because a high capacity capacitor is required to support bootstrapping. Therefore, the use of an external capacitor is necessary. Applications with size constraints, such as body implantable devices, are not appropriate for bootstrapping.

3.3.2.2 High-side ground method

The high-side ground method is applied when PMOS is used in a high-side MOS switch. The high-side ground method is similar to bootstrapping; however, the process of selecting the reference voltage is different. In bootstrapping, the reference voltage is the source of the MOS switch, while an extra voltage regulator is needed to generate the reference voltage in the high-side ground method. The power consumption of the driver is low since a low voltage taper buffer is used as the driver. However, flexibility with respect to the supply voltage variations is poor owing to its fixed reference voltage. The driver can be designed with adaptive reference voltage, but its efficiency is lower than that of bootstrapping.

3.3.2.3 Standalone level shifter driver

A level shifter is a circuit that increases a low reference level swing to a high reference level with the same swing voltage. Using a level shifter as a driver eliminates the need for an external capacitor because a low voltage gate driver such as an inverter chain is not required. In addition, since it only increases the reference level of the voltage swing, it can operate properly even with variable supply voltage.

The power consumption of a level shifter differs from that of a digital inverter. Fig.3.34 shows the schematic and waveform of a conventional level shifter. The level shifter always consumes current alternating between I_F and I_R. This current consuming property is a serious drawback of the converter driver because it lowers the power conversion efficiency (PCE). The larger the driving capacitor, the faster the switching frequency; thus, the level shifter becomes the dominant component that reduces the PCE.
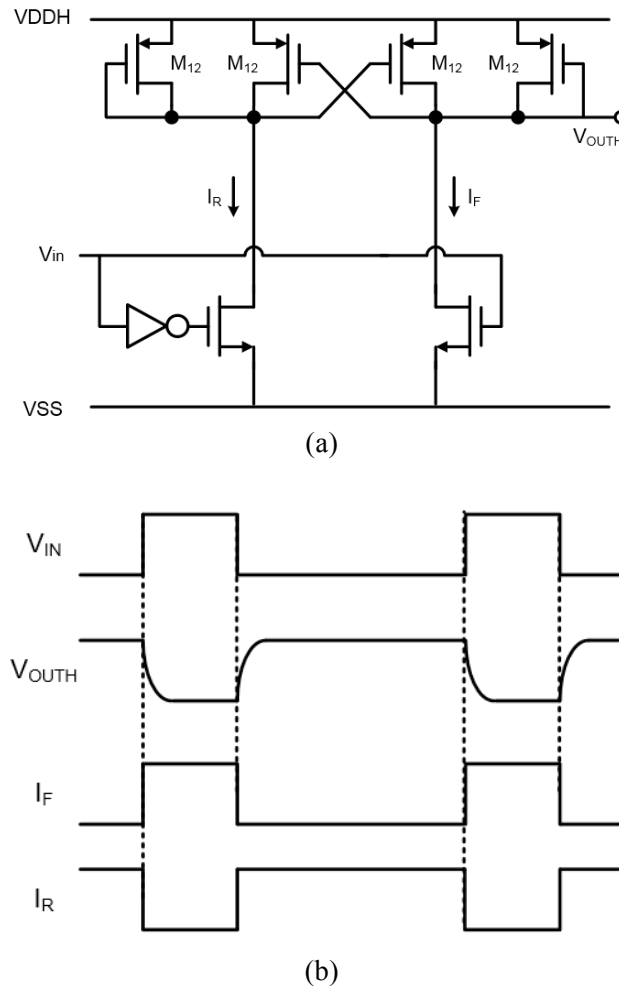
Fig.3.34. Conventional level shifter: (a) schematic, and (b) timing diagram.

89

3.3.3 Driver for body implantable converter

The PCE and the size are the main parameters of a converter used in body implantable devices. Another important parameter is the tolerance of the input voltage variation. As mentioned earlier, a switching converter uses a driver circuit to control the power MOS switch. The three commonly used techniques are bootstrapping, high-side ground method, and using a standalone level shifter. Bootstrapping and the high-side ground method have the advantage of low power consumption using a low voltage inverter chain. The level shifter has the advantage on not using external storage capacitor. In this section, a level shifter driver that realizes low power consumption by controlling the instantaneous flowing current similar to a digital inverter is introduced.

The proposed instantaneous power consuming level shifter is shown in Fig.3.35. The methodology to reduce power consumption was proposed for low power high voltage flat panel display driver in [3.62]. The instantaneous power consuming level shifter driver reduces power consumption considerably by controlling the flowing currents I_F and I_R only at the transition period. A combination of two signals from a microcontroller controls the operation of the driver. However, it is difficult to use a microcontroller for a body implantable device because it increases the size of the device and there is only one feedback signal to control the driver of a switching converter. Hence, an embedded controller for instantaneous power consuming level shifter using a single feedback signal is needed.

Fig.3.35(b) shows the block diagram of a controller for the proposed level shifter for a switching converter. The controller is composed of an edge detector, a delay cell, and an output voltage detector. The edge detector and delay cell are used to operate the level shifter during the transition period of the input signal. Fig.3.35(c) shows the timing diagram of the controller. The edge detector detects the rising edge of the input signal (V_{IN}) to turn on the falling signal of the level shifter (V_{FL}). The delay cell is used to turn V_{FL} off after a certain time delay. To control the rising signal of the level shifter (V_{RS}), the edge detector and delay cell are used in a manner similar to controlling V_{FL} by detecting the falling edge of V_{IN}.

The current I_{RS}, which controls the rising time of the level shifter output voltage (V_{OUTH}) can be very low because it only charges the gate capacitance of M_{P3} and M_{P4}. However, I_{FL}, which controls the falling time of V_{OUTH} should be high because it discharges a considerably large output capacitance. The current source I_3 is set from the relation of the switching frequency and output capacitance. I_3 draws the charge stored in the output capacitance through M_{P5}. To regulate the voltage drop, a diode connected M_{P6} is used. I_{FL} is divided into the current through M_{P5} (I_{Mp5}), which is related to the inevitable switching loss, and the current through M_{P6} (I_{Mp6}), which is related to the driver loss. Fig.3.36 shows I_{Mp5} and I_{Mp6} for varying values of V_{OUTH}. The sum of I_{Mp5} and I_{Mp6} is I_3. I_{Mp5} discharges the charge stored in the output capacitance and I_{Mp6} increases as I_{MP5} decreases. When I_{Mp5} is halved, the consumed power is as high as the switching loss (P_{sw}). From this point, the driver

90

consumes more power to fully turn on the power switch. The driver loss (P_{dr}) includes extra power consumption due to the delay margin of the delay cell (t_{dm}). To increase the PCE, an output voltage detector is used to eliminate extra power consumption.

(a)   (b)

(c)
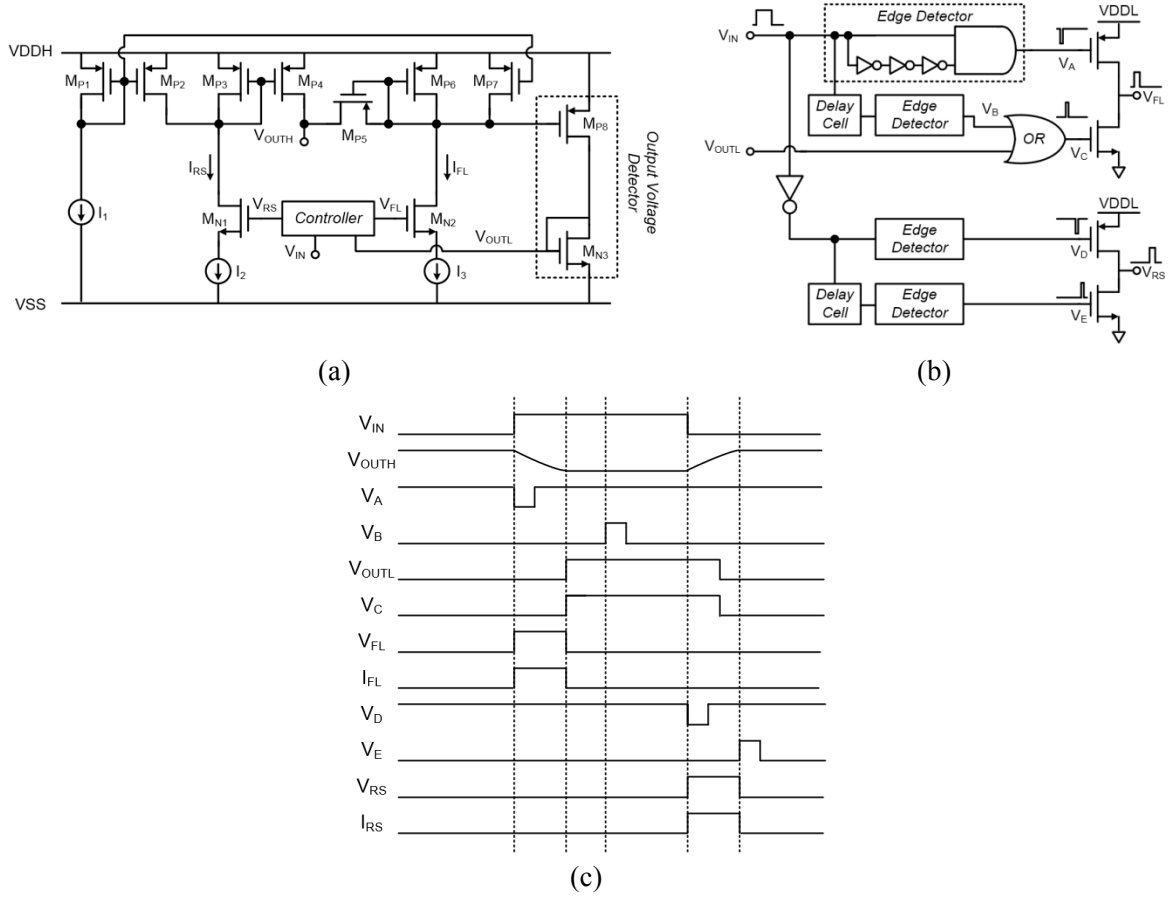
Fig.3.35. Proposed level shifter: (a) schematic, (b) controller, and (c) timing diagram.
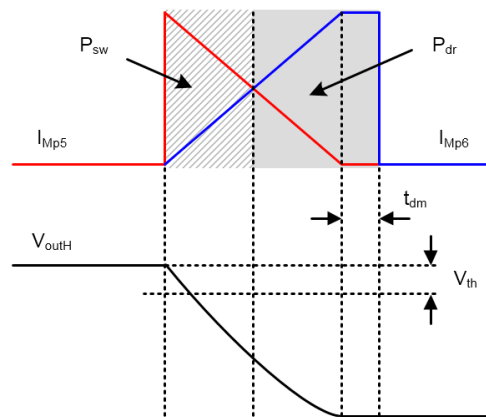
Fig.3.36. Detailed waveforms of I_{FL} and V_{OUTH}.

The output voltage detector is composed of current mirror, diode connected transistor, and comparator. The transition of V_{OUTH} is sensed by the current mirror. When V_{OUTH} falls, M_{P8} supplies current to M_{N3}, then V_{OUTL} increases. When V_{OUTL} is higher than the reference voltage, the comparator triggers the ending signal to turn the level shifter off. If the transition of V_{OUTH} becomes higher than the threshold voltage required to turn on the power switch before the time delay of the delay cell, the output voltage detector controls V_{FL} to turn the level shifter off. In the case of low supply voltage, V_{OUTH} does not vary sufficiently to be detected by the output voltage detector. In this case, the level shifter is turned off by the delay cell. Hence, the level shifter operates in a wide input range using a combination of the output voltage detector and delay cell. Monte Carlo simulation of the proposed level shifter was performed with 600 samples resulting in output voltage error of 0.1%.

The power distribution of buck converter with conventional and proposed level shifter driver is shown in Fig.3.37. Simulation was conducted when the load current is 3 mA. The result shows that the load with proposed level shifter occupies more portion because power consumption of level shifter is reduced by 66%. In Fig.3.38, efficiency of buck converter on various load with and without proposed level shifter is shown. The efficiency is increased by the maximum of 9% when the load is lightest.
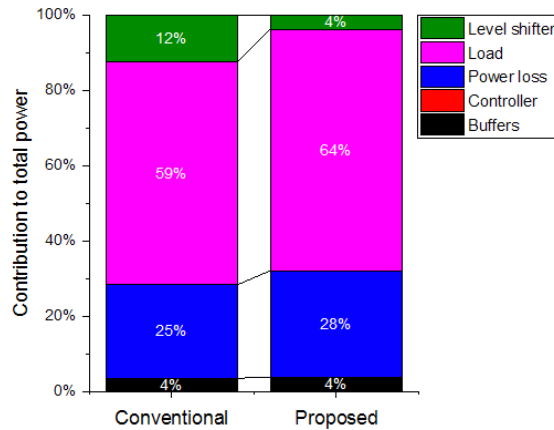
Fig.3.37. Simulated power distribution of the buck converter with conventional and proposed level shifter.
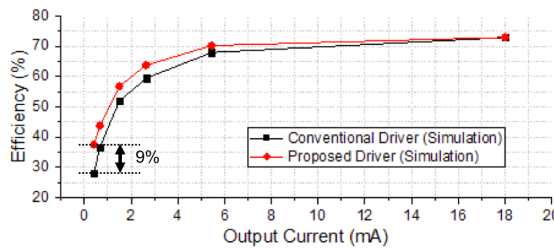
Fig.3.38. Simulated efficiencies of the buck converter with conventional and proposed level shifter driver.

92

3.3.4 Measurement results

A buck converter with the proposed instantaneous power consuming level shifter driver was implemented by the TSMC 0.18-µm BCD process. The converter includes a conventional type II compensator with error amplifier because it operates in DCM [3.63]. Fig.3.39 shows the micrograph of the fabricated buck converter. The chip area without bonding pad is 0.38 mm^2. The converter operates at a switching frequency of 1.3 MHz and can support input voltage in the range of 2–5V. It provides a regulated output voltage of 1.8 V with output current from 400 µA to 18 mA. To only verify the performance of the proposed level shifter, techniques to increase the PCE such as zero voltage switching (ZVS) and ringing suppression were not implemented.

Fig.3.40 shows the measured low voltage duty signal (V_{dutyL}), duty signal shifted to high voltage by the level shifter (V_{dutyH}), regulated output voltage, and drain terminal voltage of high-side PMOS switch (V_x), which indicates proper operation of the converter. The plot in Fig.3.40 indicates that the converter operates properly by moving the low voltage duty signal to the high voltage duty signal using the proposed level shifter. The transition speed of the output of the level shifter is slower than the low voltage duty signal, which is realized by decreasing the peak current within a limit that does not significantly affect the operation of the level shifter. Although the transition speed is slow, the converter operates successfully because the output voltage detector and delay cell provide sufficient time to turn on the power switch. Fig.3.41 shows the operation of the converter with various output current levels. The simulated and measured PCE values of the converter with proposed level shifter driver are shown in Fig.3.42.
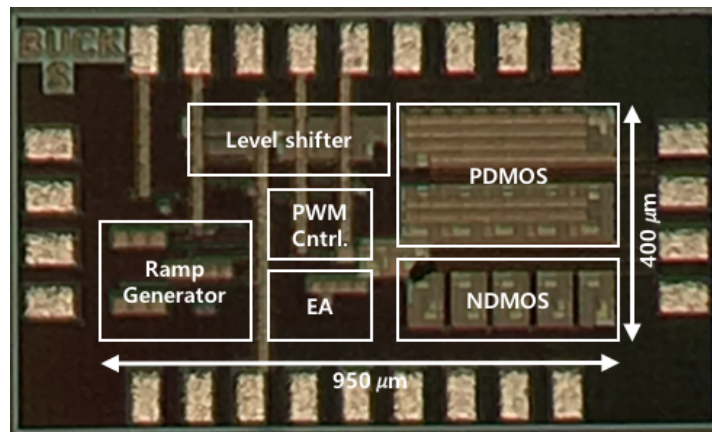
Fig.3.39. Micrograph of the buck converter with proposed level shifter.
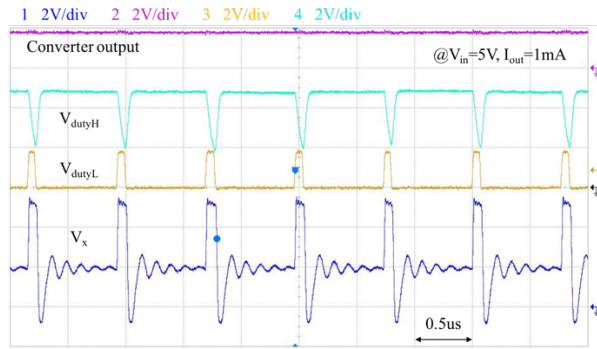
Fig.3.40. Measured voltage of converter output V_{dutyH}, V_{dutyL}, and V_x.
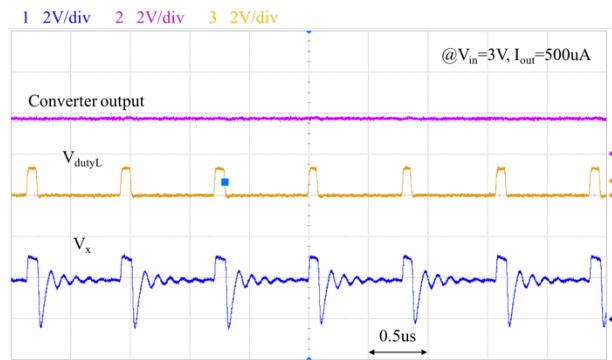
(a)
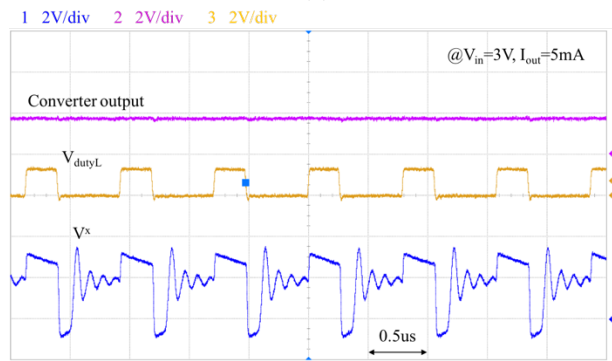
(b)

Fig.3.41. Measured voltage of converter output VdutyL, and Vx voltage at: (a) 500 μA, (b) 5 mA.
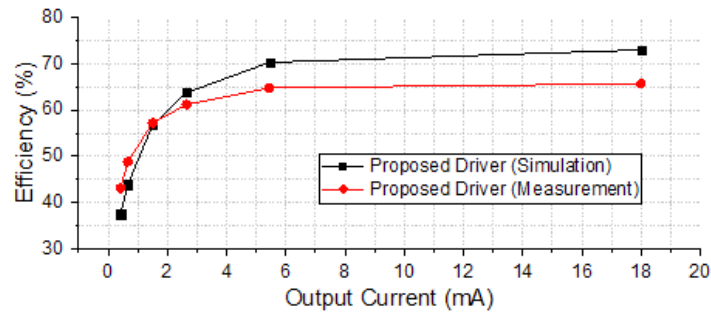
Fig.3.42. Efficiency of the buck converter with proposed level shifter driver.

94

3.3.5 Conclusion

In this section, a level shifter driver was proposed to minimize the size of the converter by removing the bootstrap capacitor while reducing the power consumption of the driver stage. To achieve low power consumption, the level shifter consumes power only during the transition time, similar to a digital circuit. The power consumption of the level shifter decreased by a third. The effect of reduced power consumption of proposed level shifter influences strongly when the load is light. Therefore, the instantaneous power consuming level shifter is suitable to use in body implantable device. The instantaneous power consuming level shifter can be also used in applications where low power consumption and size reduction are important requirements such as in human implantable devices and internet of things.

Chapter IV

WPT System for Body Implantable Devices

4.1 Motivation

WPT is a technology that has the effect of increasing the capacity of the battery by indirectly increasing the duration of the battery. It was popularized with wireless charging function in smart phone. However, WPT is most needed for BIMD. The main reasons are that a large battery cannot be inserted into the human body and an operation is required to replace the battery. Therefore, pacemaker has already adopted WPT. Since the pacemaker is relatively large in size among BIMD, the combination of a large battery and WPT can indirectly increase duration and capacity. However, BIMD, such as bio-sensors and retina implants, has a limited insertion area and space, which make it difficult to insert even batteries. WPT is an essential technique to supply power for the aforementioned applications. As mentioned in Section 2.6, there are three considerations in WPT for BIMD.

- Space limitation
- Human hazard
- Safe operation

First, space constraints are introduced by the location of insertion. Due to space constraints, the volume or size of the system must be small and the Rx coil, the core of WPT, must be small. Due to the relatively small receiver coil, the wireless power transmission performance becomes sensitive to the distance between the coils. The variation in distance between the coils changes the voltage induced in receiver. In a coil of different sizes, the voltage change is larger than the coil of the same size. In order to ensure the safety of the inserted system, the receiver circuit should be designed not to break even under wide voltage variation. In addition, the use of external passive components should be reduced to make the system smaller.

Electronics intended for the human body should lower SAR. If SAR is high, a problem may occur to the human body. The best way to lower SAR is to transmit very low power. Of course, in order to transmit low power, the load must be designed to have low power consumption, but above all, the PCE at each converting part must be high. The power converting parts in WPT are the power transfer between the transmitter coil and receiver coil, the ac to dc conversion of the rectifier, and the dc to dc conversion of the converter. Increasing the power conversion efficiency at each part can indirectly lower the absorption rate of the human body.

4.2 Proposed approaches

WPT system is made up with two coils which are transmitter and receiver coils, transmitter driver, rectifier, and DC-DC converter. Size of two coils is different because of space constraint by implant location. The power transfer efficiency is very low with different size of coils. A medium for power transfer is a human body. As a result, the transmitter cannot transfer high power because power loss in a medium will occur human hazard. Therefore, the BIMD should be operated in very low power, and WPT system for BIMD should have high power transfer and conversion efficiency. Moreover, receiver should support safe operation in wide input voltage range because different size of coils occurs large input voltage variation caused by displacement. In addition to space constraint, receiver should be designed in small size by reducing the use of external components.

To lower transmitting power, the power transfer efficiency should be increased and the efficiency in circuit level should be increased by reducing power losses. The power transfer efficiency can be increased by load transformation. PCE in circuit level can be increased by reducing power losses. The power losses in WPT circuits are switching loss, conduction loss, and driving loss. Switching loss and conduction loss can be minimized by optimizing size of power transistors, but optimization of switch control timing should be introduced. Furthermore, power reduction technique for high-side driver is needed to further reduce driving loss while supporting wide input voltage variation.

For enhancing efficiency in WPT system and proper operation with different size of coils, this research proposes three techniques:

1) Optimal resonant load transformation for efficiency enhancement.
2) Sampling-based on/off-time calibrated active rectifier.
3) Bootstrap-capacitor-less DCM-VOT wide input buck converter.

The power transfer efficiency and PCE will be increased with the proposed techniques. Also, the receiver circuit will not be broken by transferred power variation in displacement of two coils. Along with the proposed techniques, the main goal of this research is designing wireless low power transfer system for battery-less body-implanted system.

4.3 Optimal resonant load transformation for efficiency enhancement

4.3.1 Model and analysis

In the magnetic resonance WPT, a capacitor is connected to a coil to generate an LC resonance point, and power is transmitted at a resonance frequency. There are four kinds of coil structure which are SS, SP, PP, and PS depending on the position where the compensation capacitor is connected. The coil compensation structure determined by the capacitor is shown in Fig.4.1. Coils and capacitors can be connected in series or in parallel. The power transmission performance varies depending on each combination. Using a serial structure at the transmitter, power is transmitted from a voltage source, and when using a parallel architecture, power is transmitted from a current source.

The most commonly used structure among the above four structures is the SS structure. It is easy to design and easy to analyze. In order to analyze the efficiency of the performance of wireless power transmission, reflected impedance is used. The reflected impedance can be obtained by dividing the voltage induced in transmitter by receiver by the input current. The reflected impedance is a measure of how the information in receiver appears to the transmitter through coupling. Therefore, it is possible to assume that all power consumed by the reflected impedance is transmitted to receiver. To do this analysis, the M-model is used, and it is shown in Fig.4.2. WPT modeling methods include T models and L models as well as M models. The T model uses circuit theory for WPT analysis, and the L model uses the ideal transformer.
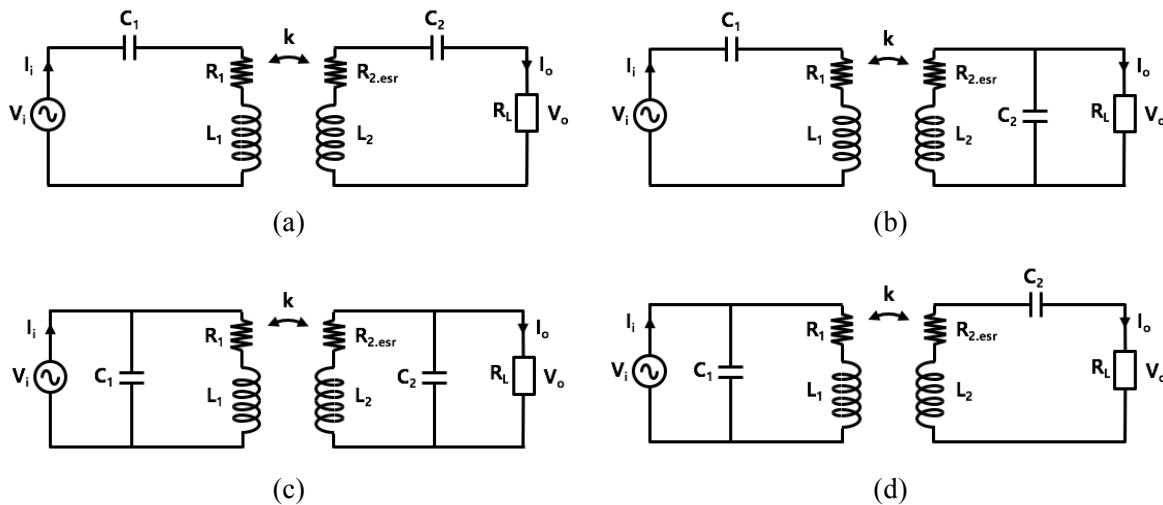
Fig.4.1. Basic compensation topologies in WPT: (a) SS, (b) SP, (c) PP, and (d) PS.

The analysis of SS using the M model is as follows. Let's assume resonance frequency is used. The reflected impedance, Z_r, can be expressed as

$$Z_r = \frac{\omega^2 M^2}{R_{sec}} \quad (R_{sec} = R_2 + R_o) \tag{4.1}$$

where $\omega = 2\pi f$, M is mutual inductance, R_{sec} is resistance in receiver which is equal to sum of parasitic resistance, R_2, and load resistance, R_o. With reflected impedance, efficiency at transmitter, η_{pri}, is

$$\eta_{pri.} = \frac{Z_r}{R_1 + Z_r} \tag{4.2}$$

where R_1 is sum of source resistance and parasitic resistance. η_{pri} is also known as coupling efficiency of WPT system. The efficiency at receiver is

$$\eta_{sec.} = \frac{R_o}{R_2 + R_o}. \tag{4.3}$$

The product of efficiency at transmitter and receiver is end-to-end efficiency, η_{tot},

$$\eta_{tot.} = \frac{Z_r}{R_1 + Z_r} \times \frac{R_o}{R_2 + R_o}. \tag{4.4}$$
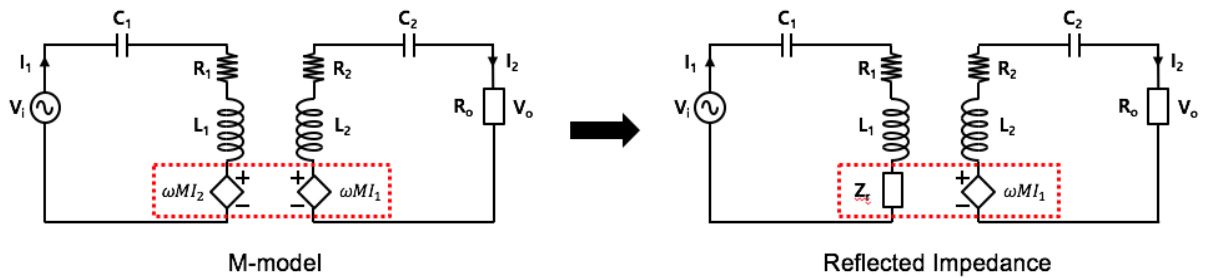
Fig.4.2. Basic M-model, and M-model with reflected impedance.

The quality factor, Q, in series compensation is as follows,

$$Q_s = \frac{1}{C_s \omega R_s} = \frac{L_s \omega}{R_s}.$$ (4.5)

where C_s is series compensation capacitor, R_s is series connected resistance, and L_s is series connected coil inductance.

Q factor of the receiver can be considered to be equal to the magnitude of the reflected impedance. Therefore, a series compensated receiver has large reflected impedance in low load resistance, which implies high power transfer efficiency. If BIMD is modeled into a resistance, it can be modeled into a high resistance because it operates in low power consumption. According to (4.5), high resistive load will have low Q factor with series compensation. Thus, parallel compensation topology is considered in receiver. Q factor in parallel compensation is as follows,

$$Q_p = R_p C_p \omega = \frac{R_p}{L_p \omega}.$$ (4.6)

where C_p is parallel compensation capacitor, R_p is parallel connected resistance, and L_p is parallel connected coil inductance. It is possible to understand from (4.6) that parallel compensation topology in the receiver is suitable with BIMD because of its high Q factor possibility. However, parallel compensation is a little complicate to analysis than series compensation. Therefore, passive impedance transformation is required [4.1]. The passive impedance transformation is a technique to transform parallel circuit to series circuit or vice versa. The passive impedance transformation is simplified when $Q_p^2 \gg 1$ and the result of parallel to series conversion is

$$C_s \approx C_p$$ (4.7)

$$R_s \approx \frac{R_p}{Q_p^2} = \frac{1}{R_p C_p^2 \omega^2}.$$ (4.8)
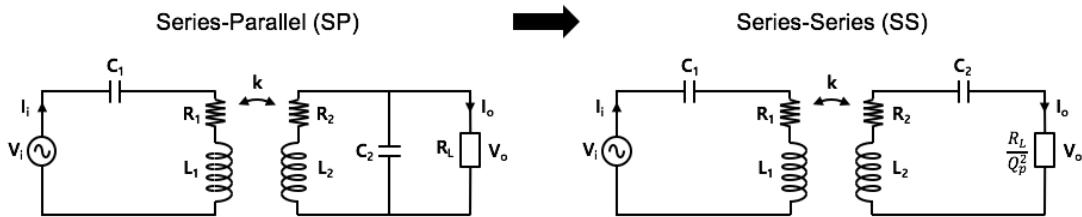
Fig.4.3. Parallel to series conversion in receiver.

100

After the passive impedance transformation, the reflected impedance is

$$Z_{r,sp} = \frac{\omega^2 M^2}{R_2 + \frac{R_L}{Q_L^2}} \qquad (4.9)$$

where $Z_{r,sp}$ is reflected impedance in series to parallel WPT system, R_L is load resistance, and Q_L is Q factor with R_L. With (4.2), (4.3), and (4.9), high Q factor which is equal to high reflected impedance induces high efficiency in transmitter but low efficiency in receiver. In contrast, low Q factor which is equal to low reflected impedance induces low efficiency in transmitter but high efficiency in receiver. It is possible to perceive that optimum Q factor exists to have maximum efficiency.

To achieve optimum Q factor, we need to find a R_L which makes $\frac{\partial \eta}{\partial R_L} = 0$. The end-to-end efficiency can be calculated by combining (4.4) and (4.9),

$$\eta_{tot.} = \frac{Z_r}{R_1 + Z_r} \times \frac{R_o}{R_2 + R_o} = \frac{\frac{\omega^2 M^2}{R_2 + \frac{R_L}{Q_L^2}}}{R_1 + \frac{\omega^2 M^2}{R_2 + \frac{R_L}{Q_L^2}}} \times \frac{R_o}{R_2 + R_o}$$

$$= \frac{\omega^2 M^2 R_L}{R_p R_L^2 + 2 R_p R_s R_L + R_p R_s^2 + \omega^2 M^2 R_L + \omega^2 M^2 R_s}. \qquad (4.10)$$

where $M = k\sqrt{L_1 L_2}$. The optimum R_L is extracted from (4.10) by partially differentiating end-to-end efficiency to load resistance, R_L. The extracted optimum R_L, $R_{L,opt}$ is

$$R_{L,opt} = \frac{1}{C_2^2 \omega^2 \sqrt{R_2^2 + \frac{R_2}{R_1} \omega^2 M^2}} \qquad (4.11)$$

where R_1 is parasitic resistance in transmitter, R_2 is parasitic resistance in receiver, and C_2 is compensation capacitor in receiver. To find optimum load resistance, simulation environment is established, and it is shown in Table 4.1. L_1 is transmitting coil, which is also known as primary coil, L_2 is receiving coil, which is also known as secondary coil, and C_1 is compensation capacitor in transmitter. From the simulation, $R_{L,opt}$ is 6.5 $k\Omega$ with the given specifications.

Table 4.1. Parameters of primary and secondary coils for simulation

Parameter	k	L_1	C_1	R_1	L_2	C_2	R_2
Value	0.05	18 μF	7.41 pF	100 Ω	3.6 μH	37 pF	10 Ω

4.3.2 Proposed load transformation technique

In the previous section, the method to obtain optimum load for maximum efficiency is introduced in WPT environment. In a given WPT environment, the optimum load value is 6.5 $k\Omega$. However, the actual target load is about 1.8 $k\Omega$. Using a 1.8 $k\Omega$ as a load will result in significantly lower efficiency than using a 6.5 $k\Omega$. So an additional circuit is required that can amplify the load between the coil and the load.

Fig.4.4 shows two types of L-section technique used for impedance matching in the RF microelectronics. The L-section is used to amplify or attenuate the equivalent load. If the LC value used in the L-section is set to the resonance frequency, the reactance component can be canceled and neglected, which implies that it is a suitable technology for the magnetic resonance WPT. Since the Fig.4.4(a) increases the load, it is applied to the SP topology.

A schematic with L-section is shown in Fig.4.5. To have easier analysis, series connected capacitor, C_t, is transform into parallel. Then, inductance, L_t, and capacitance for equivalent load amplification is canceled out. The Q factor with L-section is

$$Q_t = \frac{1}{R_L C_t \omega} = \frac{L_t \omega}{R_L} \tag{4.12}$$

and amplified equivalent load resistance is

$$R_o = Q_t^2 R_L = \underbrace{\frac{1}{C_t^2 \omega^2 R_L}}_{(1)} = \underbrace{\frac{L_t^2 \omega^2}{R_L}}_{(2)} = \underbrace{\frac{1}{C_2^2 \omega^2 \sqrt{R_2^2 + \frac{R_2}{R_1}\omega^2 M^2}}}_{(3)} \tag{4.13}$$

.

(a)   (b)
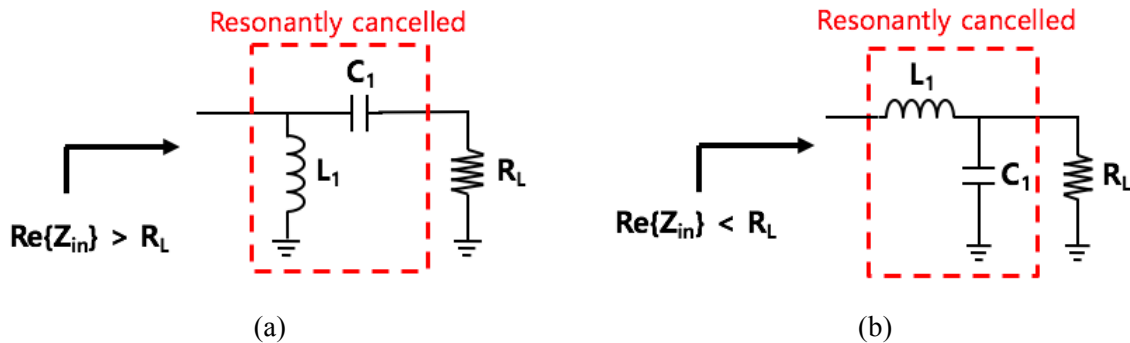
Fig.4.4. L-section for impedance matching in RF microelectronics.
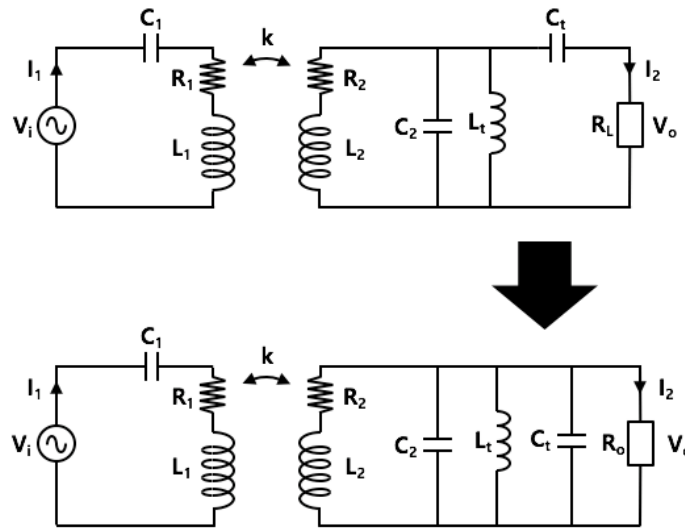
Fig.4.5. Series-Parallel topology with L-section.

With (1) and (3) in (4.13), capacitance for L-section is calculated, and it can be expressed as,

$$C_t = \sqrt{\frac{C_2^2 \sqrt{R_2^2 + \frac{R_2}{R_1}\omega^2 M^2}}{R_L}}.$$

(4.14)

With (2) and (3) in (4.13), inductance for L-section is calculated, and it can be expressed as,

$$L_t = \sqrt{\frac{R_L}{C_2^2 \omega^4 \sqrt{R_2^2 + \frac{R_2}{R_1}\omega^2 M^2}}}.$$

(4.15)

An inductance and a capacitance for optimum load resistance can be calculated with parameters from Table 4.1. Parameters are applied to (4.14) and (4.15), and 3.4pF and 39μH are achieved, respectively. Parameters including L-section are organized in Table 4.2.

Table 4.2. Parameters of primary and secondary coils including L-section

Parameter	k	L_1	C_1	R_1	L_2	C_2	R_2	Lt	Ct	RL
Value	0.05	18μF	7.41pF	100Ω	3.6μH	37pF	10Ω	39μH	3.4pF	1.8kΩ

4.3.3 Simulation results

MATLAB software is used to verify the proposed load transformation technique. The equations for verification was derived from T-model, and the parameters in table 4.2 are used. In order to investigate the efficiency changes due to displacement in the WPT environment, the simulation was done while the coupling coefficient variation. The range of the coupling coefficient variation was confirmed by measurement, and from 0.1 to 0.02 was measured when the distance between the coils was changed from 0 mm to 30 mm. Before measuring the efficiency, we simulated the change of reflected impedance by L-section.

Fig.4.6 shows the change in reflected impedance when the coupling coefficient changes. Unlike other verification, the reflected impedance was extracted from M-model. The blue line is the basic SP topology, and the red line is the SP topology with the L-section, SPT. The reflected impedance is increased by the L-section, which will be resulting efficiency increment.

Fig.4.7 shows the change in efficiency when the coupling coefficient changes. When the L-section is used, it is confirmed that the efficiency increases even if the coupling coefficient is changed. The lowest increment is 2.6% and the maximum increment is 8.6%. The maximum increment is appeared at coupling coefficient near 0.05 because optimization was done near 0.05 in section 4.3.2.

In addition, the voltage gain change was also verified. The change in voltage gain is shown in Fig.4.8. In the conventional SP topology, the voltage gain decreases as the coupling decreases. However, using the L-section, the decrease in the voltage gain is not proportional to the decrease in the coupling coefficient. In the basic SP topology, the voltage gain is changed from 0.4 to 1.4. The voltage gain in L-section type is changed from 0.6 to 1. The result shows that L-section suppresses the variation of voltage gain.
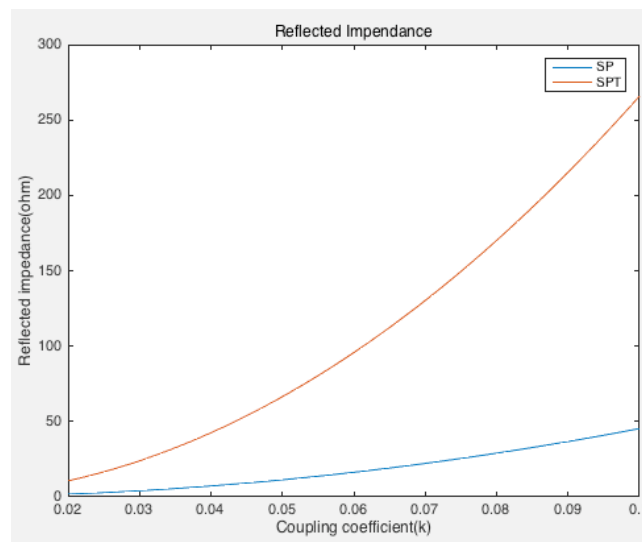
Fig.4.6. Reflected impedance vs. Coupling coefficient. (SP: series-parallel, SPT: series-parallel and L-section)
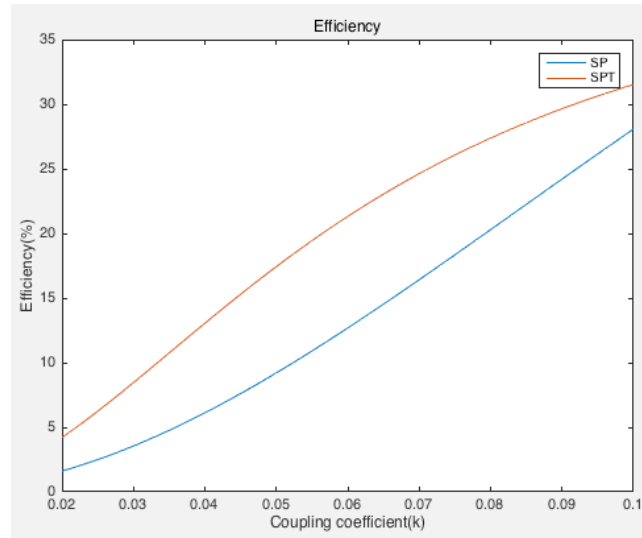
Fig.4.7. Power transfer efficiency vs. Coupling coefficient. (SP: series-parallel, SPT: series-parallel and L-section)
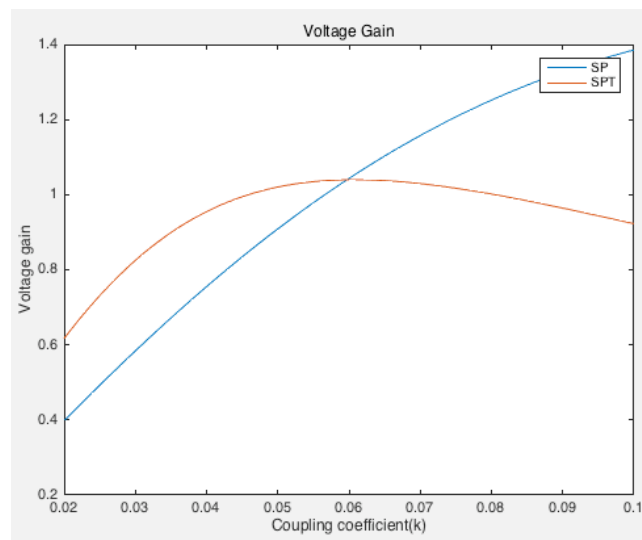
Fig.4.8. Voltage gain vs. Coupling coefficient. (SP: series-parallel, SPT: series-parallel and L-section)

4.3.4 Coil characteristics, and measurement results

The implant location is decided as artificial blood vessel. The size of transmitting coil and receiving coil are different in order to resolve misalignment problem. The coils are fabricated with flexible printed circuit board (FPCB). The fabricated coils are shown in Fig.4.9. Fig.4.9(a) is primary coil, and Fig,4.9(b) is secondary coil. Outer dimension of primary coil is 50 mm $\times$ 70 mm. A width of electric wiring and spacing is 0.5 mm. Inner dimension, which is empty space, is 25 mm $\times$ 40 mm. The winding is 14 turns, and the inductance is 19 μH. And, outer dimension of secondary coil is 10 mm $\times$ 20 mm. A width of electric wiring and spacing is 0.1 mm. Inner dimension, which is empty space, is 6 mm $\times$ 16 mm. The winding is 10 turns, and the inductance is 3.3 μH.

Keysight network analyzer E5061B was used for measurement, and the WPT analysis software provided by E5061B was used for measuring the power transfer efficiency. The compensation capacitor is selected as a value which resonates at frequency of 13.56 MHz in accordance with the measured coil inductance. For L-section, 33 μH is used for L_t, and 4.2 pF is used for C_t. The secondary coil is moved vertically from primary coil from 0 mm to 30 mm, which is an identical environment to the coupling measurement. The measured power transfer efficiency and the voltage gain are shown in Fig.4.10. The maximum efficiency increment is 9.82%, and the average efficiency increment is 5.34%. The efficiency increment trend is similar to the simulation result. In measured voltage gain, SPT shows less gain variation than SP in vertical displacement. Maximum voltage gains of SP and SPT is 2.08 and 1.38, respectively. Minimum voltage gains of SP and SPT is 0.08 and 0.31, respectively. The additional effect of reducing the change in voltage gain will provide simplification on receiver circuit design.

(a)   (b)
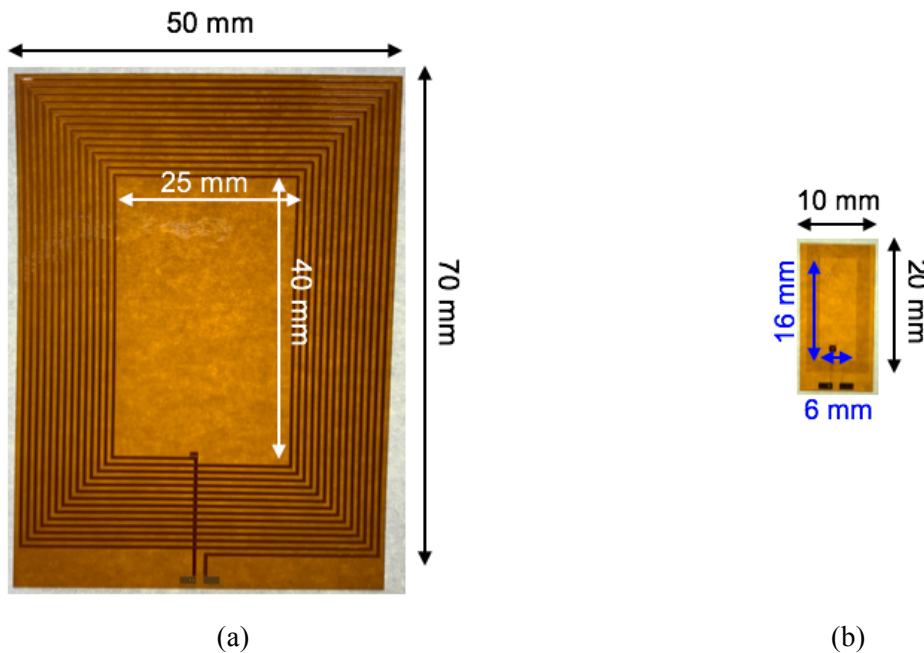
Fig.4.9. Fabricated coils with flexible printed circuit board: (a) primary coil, and (b) secondary coil.
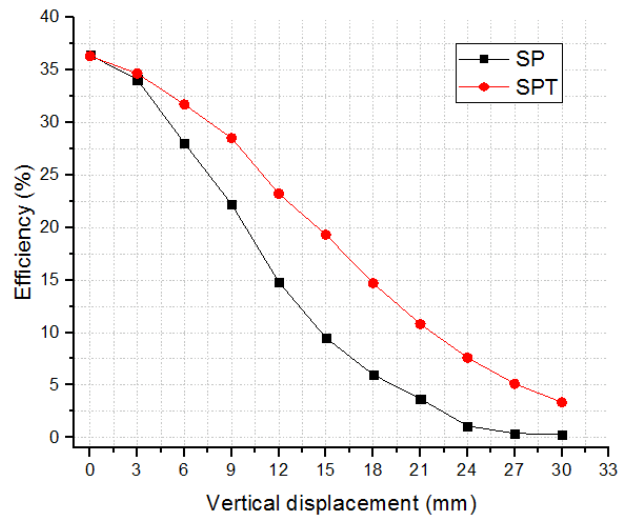
(a)
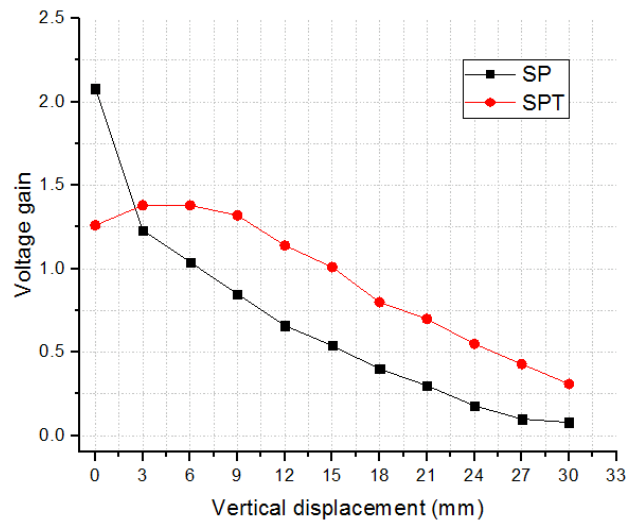
(b)

Fig.4.10. Measurement results of between SP and SP with L-section (SPT): (a) power transfer efficiency, and (b) voltage gain.

4.4 Sampling-based delay compensated active rectifier

4.4.1 Background

Existing BIMD have limited performance and usable time due to limitations of available power. Pacemakers, cochlear implants, and gastric stimulators, which are universally implanted with a battery, had to conduct operation again to replace the battery after the end of battery life. In order to increase the service life, the size of the capacity of battery should be increased. However, there is a limitation in increasing battery capacity because of the foreign body sensation to the patient, and the volume of the battery cannot be increased beyond a certain limit due to the space limitation in the implant location. To overcome the limitations, WPT is emerging as a power supply solution in the field of BIMD. In particular, attempts have been made to supply electric power from the outside of the human body by using the MR-WPT in implantable devices [4.2] - [4.3].

The MR-WPT uses the magnetic coupling between the primary coil and the secondary coil to transfer power. The power amplifier (PA) applies the AC current to the primary coil to generate a magnetic field, and the magnetic field is applied to the secondary coil according to the amount of magnetic coupling between the primary coil and the secondary coil. The AC voltage induced at the receiver is changed to a DC voltage through a rectifier, and it is supplied to the voltage required by the implanted device through the regulator. The magnetic coupling becomes stronger as the distance between the primary coil and the secondary coil becomes closer to each other or the size of the two coils becomes the same. However, in the case of BIMD, the magnetic coupling is very low because of the size of the implanted coil is small due to the implant space limitation. In a situation where magnetic coupling is low, the receiver circuit must be designed to operate stably even with changes in voltage gain, because the power transfer efficiency and voltage gain changes due to the distance and alignment between the coils.

A power consumption of BIMD powered by WPT without a battery varies from application to application, from less than 1 mW [4.4] to tens of mW. The PCE of receiver circuit is significant when the power consumption of the implanted device is large. The low PCE of the receiver end not only can damage the surrounding skin tissues by generating heat due to the power loss, but also increases the amount of electromagnetic field radiated to the human body by making more power available at the transmitting end.

The rectifier, which converts the induced AC voltage to DC voltage, should be designed to have a high PCE and a high voltage conversion ratio (VCR) within a voltage range caused by a change in coil coupling. Diodes that have been used as passive switches have been replaced with active switches to reduce the voltage drop and to achieve high efficiency, but internal delays caused by parasitic resistances inside the chip, parasitic capacitors and speed limit of the comparator have become a

problem. The internal delay of the active switch reduces the duration of power supply, generates reverse current, and reduces PCE and VCR. In particular, the internal delay of the active switch becomes a major negative influence on performance of the rectifier because the higher the frequency is used to reduce the size of external components such as coils and resonant capacitors. Therefore, compensating the internal delay is the most important factor in designing an active rectifier with high PCE and VCR.

In this section, an adaptive delay compensated active rectifier that can operate at a wide input voltage of 3-12V is proposed. The delay compensation block consists of negative feedback based on the sample and hold, and it compensates the delay even when the magnitude of the voltage applied to the rectifier changes due to the change of the magnetic coupling or PVT variation.

4.4.2 Previous approaches
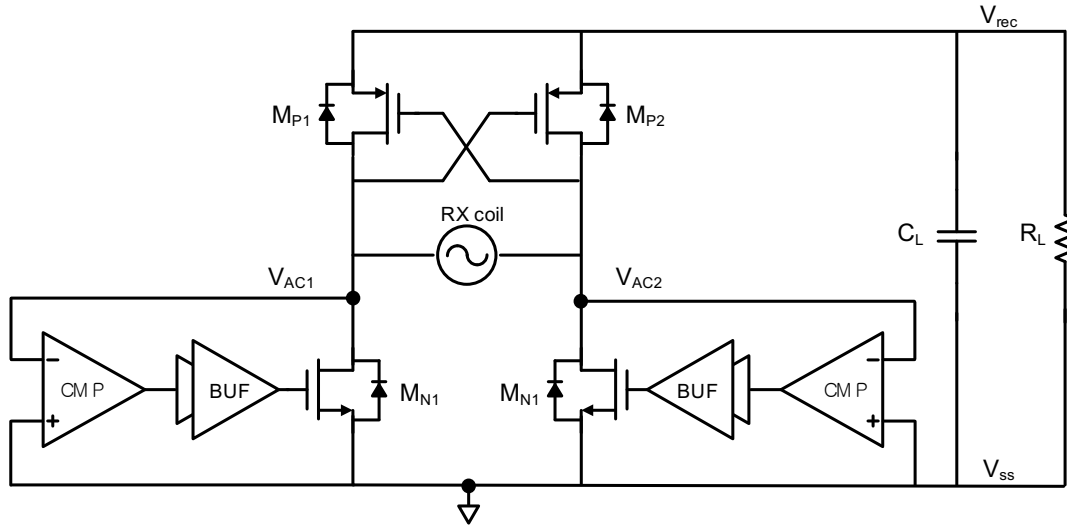
Fig.4.11. Block diagram of conventional PMOS cross-coupled active rectifier.

Fig.4.11 shows an active rectifier commonly used in implantable devices. The high-side switch is presented in a cross-coupled form and does not require a driver. The low-side switch turns on when the coil induced voltage, V_{AC}, becomes lower than V_{SS}, detects by a comparator. Parasitic resistors and capacitors, and the speed limit of the comparator causes a delay in the switch transition. A delay of several ns or more results in an efficiency reduction. The delay affects both on-transition and off-transition of the low-side switches. If the on-transition time is delayed, the effective conduction time is reduced to increase the peak current. The increased peak current increases the voltage drop. On the other hand, when the off-transition time is delayed, the switch is still turned on even when the V_{AC} is lower than the rectified voltage, V_{rec}. It generates a reverse current from the storage capacitor, and it is critical to the PCE.

Conventionally, delay in switch control is minimized by increasing the speed of the comparator. However, it is not suitable for use in the BIMD because it requires large power to speed up the comparator. In order to overcome the problem, there have been many studies to compensate the delay by operating comparator faster than the actual comparison voltage by applying offset to the input of the comparator. Compensating for delay by applying offset to the input of the comparator eliminates the need for a high-speed performance.

In [4.5] and [4.6], reverse current is removed by compensating the low-side switches turn-off delay using unbalanced current biasing or unbalanced sizing of the comparator. However, since the methods generate only fixed offsets, the delay cannot be fully compensated when the magnitude of induced voltage at the receiver or the load resistance changes. And the fixed offset in a specific condition

cannot have compensation accuracy under process, voltage, and temperature (PVT) variation. [4.7] introduces a switched-offset technique that applies unbalanced current biasing only during turn-off transition. Unlike [4.5] and [4.6], the offset is only applied after the low-side switch is turned on to avoid increase on turn-on delay. However, fixed offset cannot still compensate the delays perfectly in various conditions.

[4.8] and [4.9] dynamically apply turn-on offset and turn-off offset through a switch operation to prevent reverse current and reduce conduction loss by increasing effective conduction time. The amount of offset is externally control by manipulating the control bit. However, off-chip control is not suitable for the implantable system. Therefore, an adaptive delay compensation technique that can adjust offset internally according to the operation condition is required.

4.4.3 Proposed sampling-based delay compensation technique
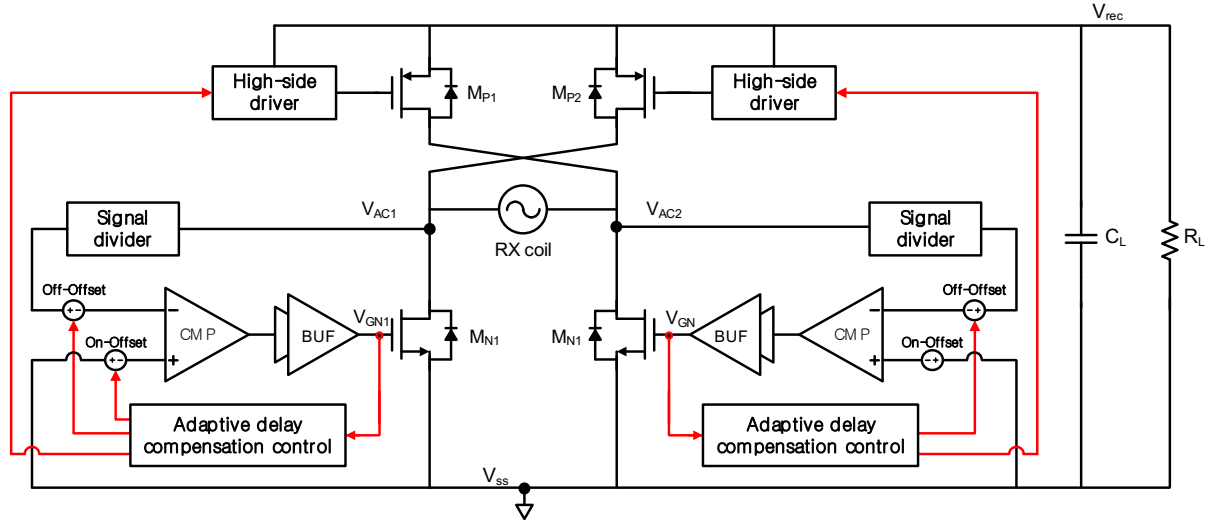
Fig.4.12. Proposed adaptive delay compensated active rectifier.
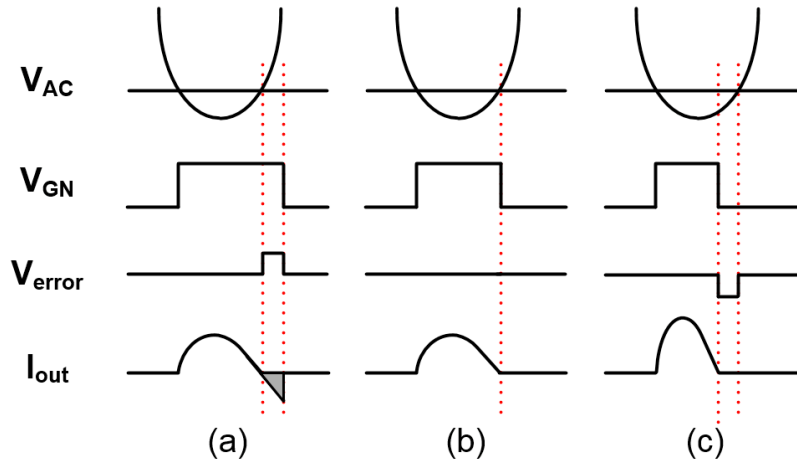
Fig.4.13. Waveform of rectifier when delay is: (a) less, (b) perfect, and (c) over compensated.

An active rectifier including an adaptive delay compensation technique that can adjust the amount of offset internally is shown in Fig.4.12. It aims for a loosely coupled WPT system, where the required power and coupling coefficient changes. The power switches in proposed active rectifier is designed with DMOS to operate over a wide input voltage range. The comparator and circuits for adaptive delay compensation control block are designed with CMOS to minimize power consumption. Since the circuits can be damaged when a high V_{AC} is induced, a signal divider is used to lower the voltage. In addition, high-side drivers are employed to control high-side switches because the cross-coupled PMOS structure cannot be used due to the gate-source voltage limit in a situation where a wide input voltage is required.
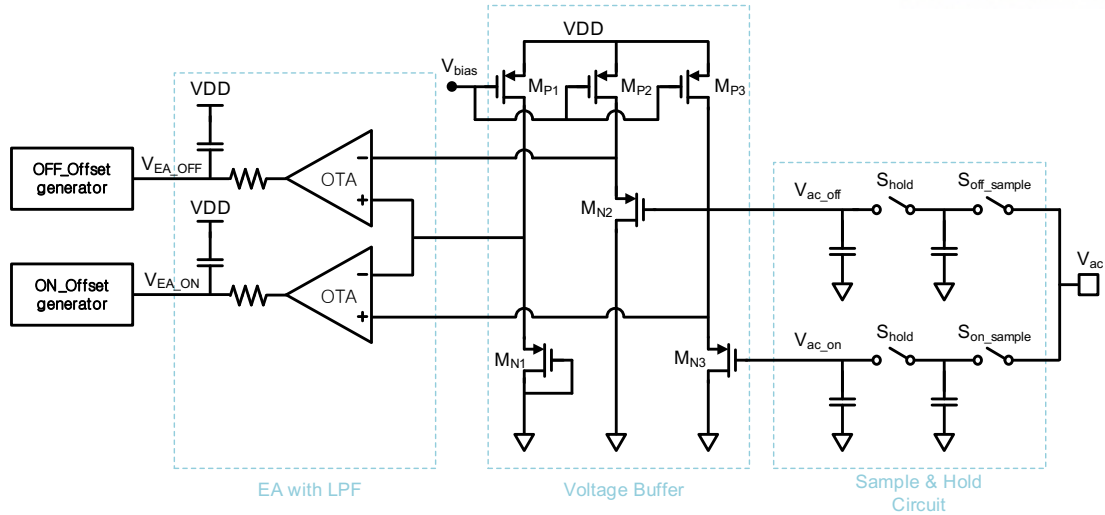
Fig.4.14. Schematic of sampling-based adaptive offset generator.
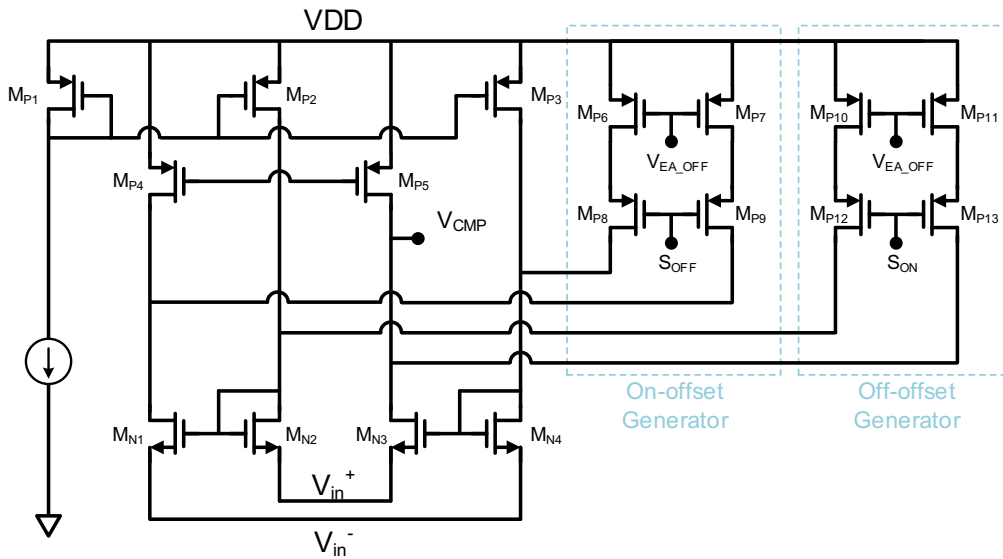
Fig.4.15. Schematic of common gate comparator and push-pull type offset generator.

Fig.4.13 shows waveforms of rectifier when the delay compensation is applied. If the delay is less compensated, the reverse current occurs. If the delay is over compensated causing early gate transition, the conduction time is reduced, and the peak current is increased. Hence, it is necessary to adaptively control the offset to compensate the delay because it acts as a factor to lower the PCE. Likewise, when compensating for the internal delay that occurs during turn-on period, the delay compensation becomes a problem if the amount of offset is added more or less than necessary. In contrast to the turn-off period, when the delay is over compensated, a reverse current occurs. When the delay is less compensated, the conduction time decreases and the peak current increases.

113

The proposed adaptive delay compensation control block consists of two negative feedbacks to compensate the delay occurring at turn-on and the turn-off to generate gate transition at optimal timing. The offset generated by the negative feedback is alternately applied to the comparator through a switch operation. The two negative feedbacks produce offsets equal to the difference between V_{AC} and V_{SS} by detecting the V_{AC} at the moment of turn-on and turn-off of low-side switches. The V_{AC} value is continuously detected to change the amount of offset. Therefore, adaptive delay compensation is possible, even if the magnitude of input signal is changed or the power required by the load is changed.

A sampling-based adaptive offset generator (SBAOG), a key circuit in the adaptive delay compensation control block, is shown in Fig.4.14. SBAOG has cascade connection of sample-and-hold circuit, voltage buffer, and error amplifier (EA). Each circuit has a parallel structure to compensate turn-on delay and turn-off delay. The SBAOG samples the V_{AC} at the moment when the gate transition of the low-side switch occurs, and makes offset by the difference from the V_{SS}. Since the sampled voltages are close to V_{SS}, it is necessary to increase the voltage level to match the dynamic range of the OTA. A symmetric single stage voltage buffer is used to increase voltage level of sampled signal and V_{SS}. EA is designed to have a bandwidth that is sufficiently lower than the resonant frequency used for WPT. By adding a low pass filter to the output stage, the noise component due to the switching operation of the sample-and-hold circuit is reduced.

Fig.4.15 shows the common gate comparator and push-pull type offset generator used in the proposed active rectifier. V_{EA_OFF} and V_{EA_ON}, which are output signals of EA, are applied to the PMOS gate of the offset generator to determine the offset. The offset generator generates an offset by flowing additional current to the comparator which is similar to the unbalanced-current biasing scheme. The timing of adding offset is controlled with S_{OFF} and S_{ON}.

Fig.4.16 shows the timing diagram and control logic used to control the switch of the adaptive delay compensation block when V_{AC1} is used as input. The block receives V_{GN1} and V_{GN2}, which are gate control signal of two low-side switches, and controls sampling timing and offset generating timing. The switch control is based on SR latch. Turn-on sampling and turn-off sampling starts from the falling edge of V_{GN2}. It stops turn-on sampling at the rising edge of V_{GN1}. It stops turn-off sampling at the falling edge of V_{GN1} and detects V_{AC}. The S_{hold} signal is generated from $S_{on,sample2}$, and is applied via delay logic to prevent it from turning on simultaneously with $S_{off,sample1}$. Offset enable signals S_{on1} and S_{off1} are generated from the output of SR latch which has the rising edge detector of V_{GN1} and the falling edge detector of V_{GN2} as an input. The turn-on offset is applied from the falling edge of V_{GN2} to the rising edge of V_{GN1}. The turn-off offset is applied from the rising edge of V_{GN1} to the falling edge of V_{GN2}.

(a)

(b)
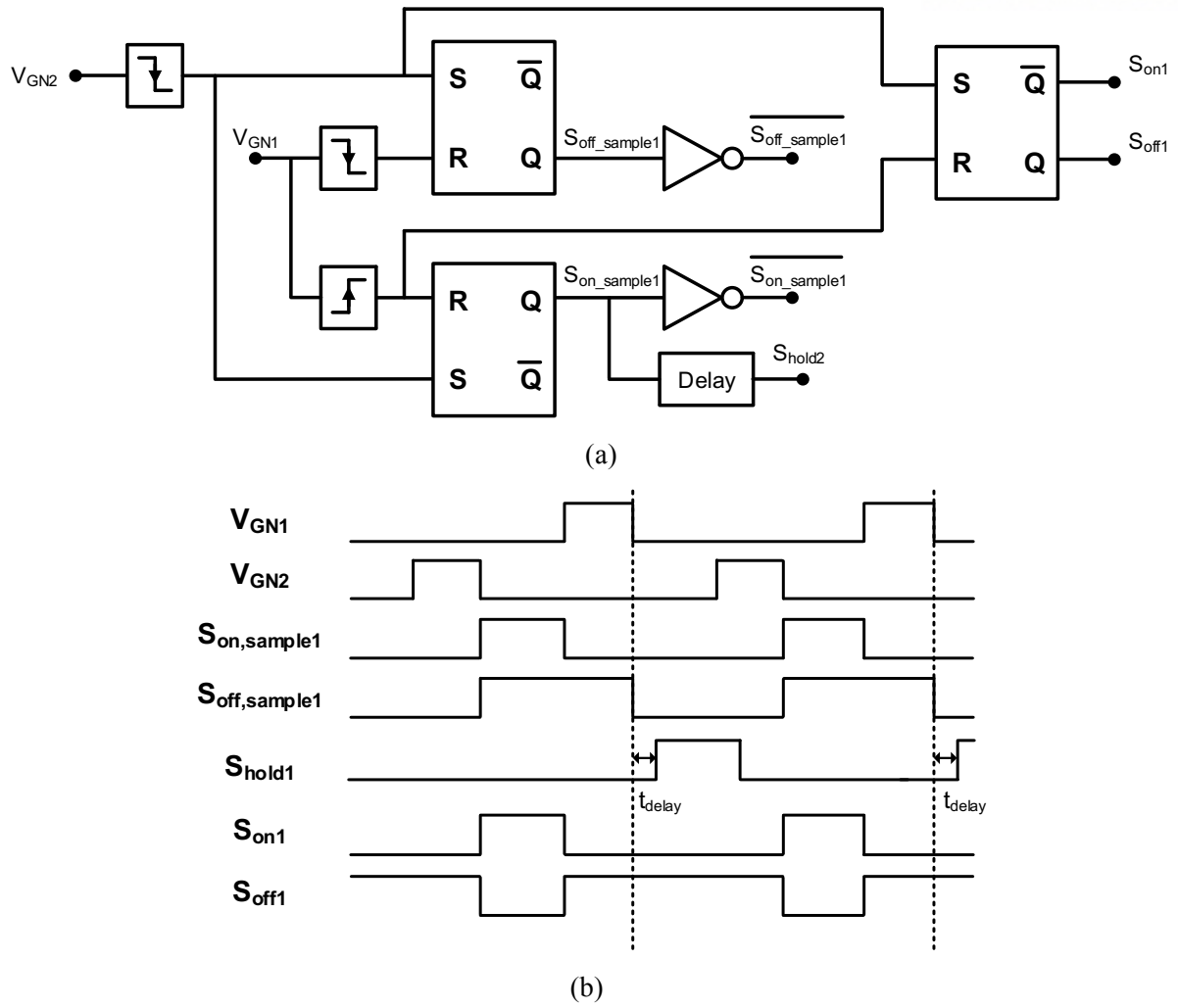
Fig.4.16. Control logic of proposed delay compensation circuit: (a) block diagram, and (b) timing diagram.

4.4.4 Simulation and measurement results

An active rectifier with the proposed adaptive delay compensation technique was designed using the TSMC 0.18-μm BCD process. The storage capacitor which holds the output DC voltage of the active rectifier is an only external component. The proposed active rectifier is designed to operate over a wide AC input voltage range from 3V to 12V. To minimize power consumption, a comparator and a delay compensation block are designed with 1.8V devices.

Fig.4.17 shows simulation results of the input AC waveform, delay compensated low-side switch gate signal, and output current waveform when the load requires 6 mW as output power. Fig. 7 (a) and 7 (b) show waveforms when the input voltage is 3 V and 12 V, respectively. It can be seen that the on- and off-delay is well compensated with the proposed technique at the low and high limit of the input voltage range.
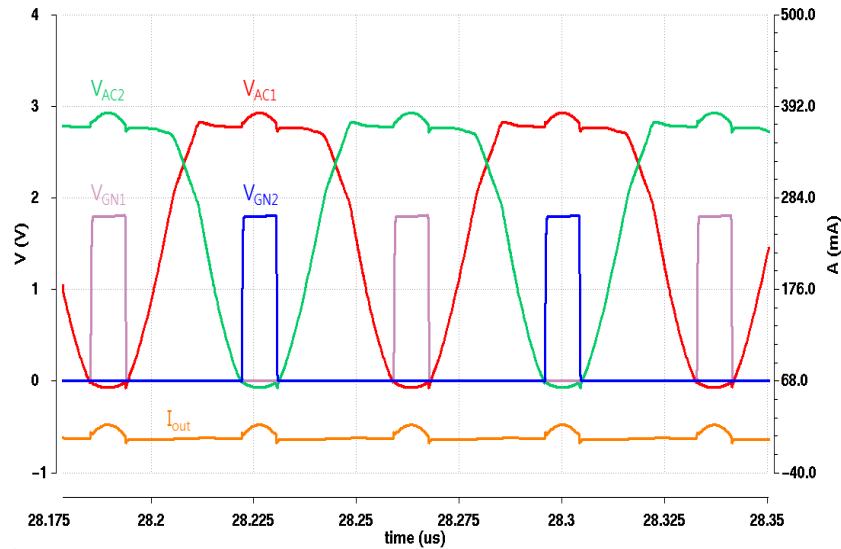
(a)
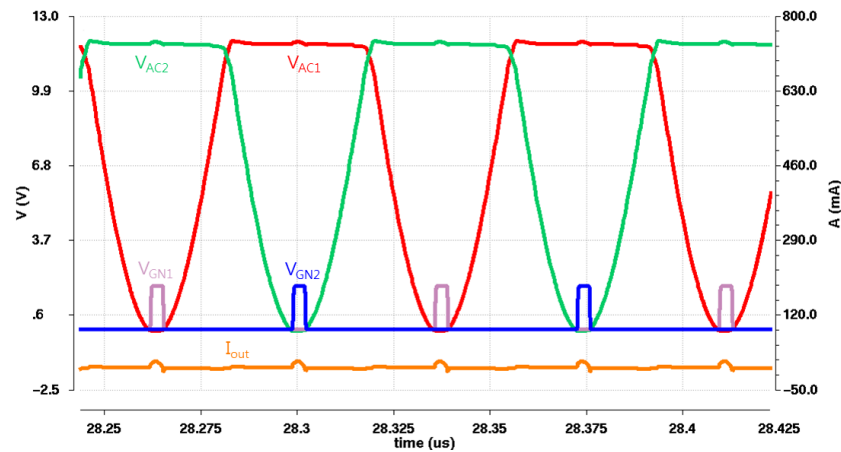
(b)

Fig.4.17. Simulated waveforms of delay compensated switch operation and output current at: (a) V_{AC} = 3V, and (b) V_{AC} = 12V.

116

(a)　　　　　　　　　　　　　　(b)
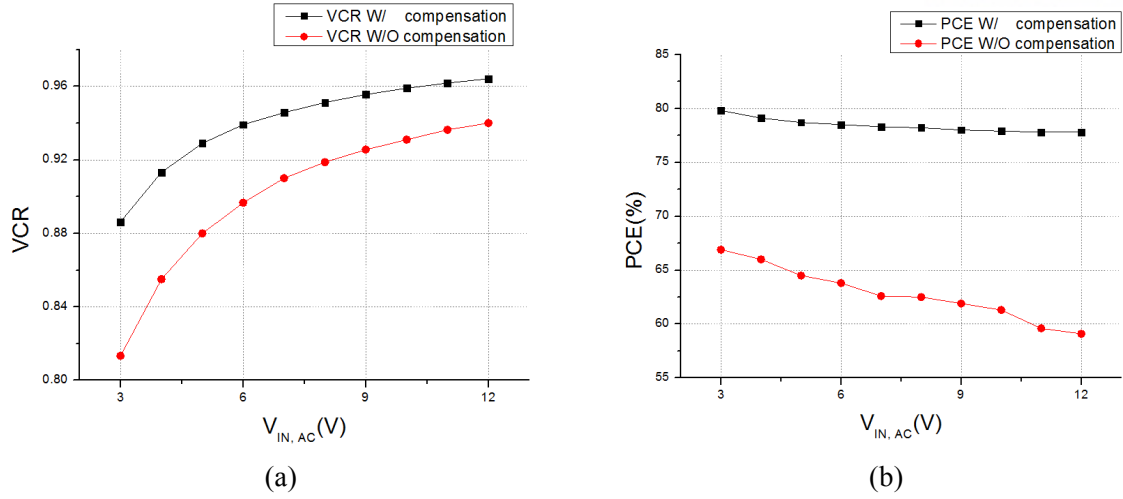
Fig.4.18. Simulation results while input AC voltage changes with and without proposed compensation technique: (a) VCR, and (b) PCE.

(a)　　　　　　　　　　　　　　(b)
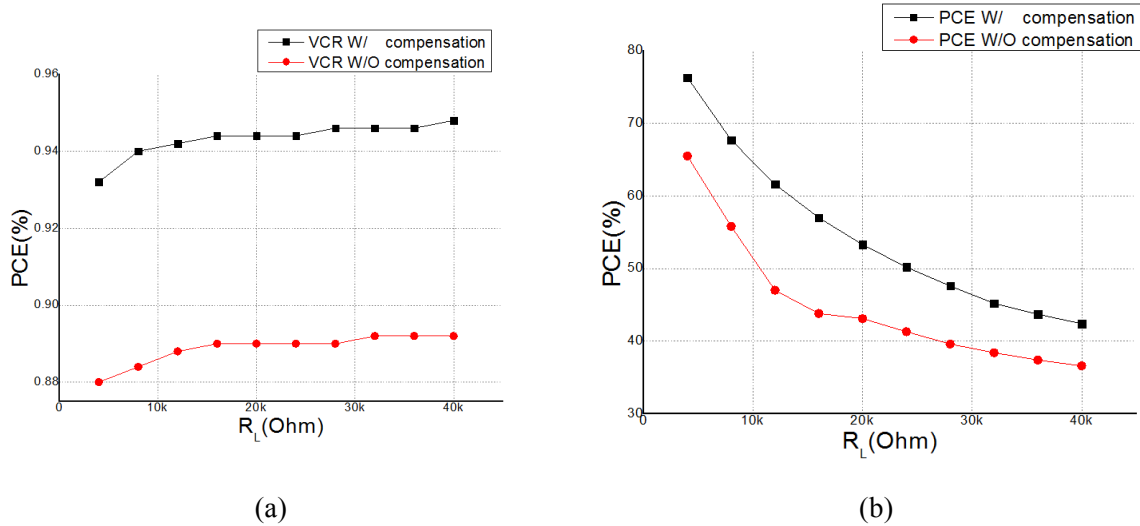
Fig.4.19. Simulation results under load resistance variation with proposed compensation technique: (a) VCR, and (b) PCE.

Fig.4.18 shows the VCR and PCE of the active rectifier with the proposed technique without the adaptive delay compensation technique while the input voltage is changed from 3V to 12V. The results show that higher VCR and PCE are achieved with the proposed technique. To achieve VCR in Fig.4.18 (a), the simulation is done with the fixed output power at 6mW. If the input voltage increases, the output current decreases due to increased resistance. Therefore, the lowest VCR is achieved when the input voltage is 3V, and the largest VCR is achieved when the input voltage is 12V. The minimum VCR value of the delay compensated active rectifier is about 0.88 at Vin = 3V and the maximum VCR value is over 0.96 at Vin = 12V. The PCE graph of Fig.4.18 (b) was also measured with the fixed output power at 6 mW. The PCE of the delay compensated active rectifier is about 80% at Vin = 3V

117

and about 77.5% at Vin = 12V. As the input voltage increases, the PCE decreases because the increase in the power consumed by the high-side driver is greater than the reduction in the conduction loss.

VCR and PCE of the delay compensated active rectifier when the load resistance is changed are shown in Fig.4.19. The input voltage is fixed at 5V and the load resistance is increased 10 times to reduce the output power from 6mW to 0.6mW. As shown in Fig.4.19 (a), VCR is 0.9 or higher even when the load resistance is changed. In the PCE graph of Fig.4.19 (b), PCE tends to decrease as the load resistance increases because the amount of power consumed by the adaptive delay compensation block and the driver are larger than that required by the load. Therefore, to achieve the efficiency improvement using the adaptive delay compensation technique, the active rectifier should be employed under load conditions requiring a minimum of several mW of power.

The proposed active rectifier with adaptive delay compensation technique is implemented in a 0.18-µm BCD process. Fig.4.20 shows chip microphotograph of fabricated active rectifier. Fig.4.21 shows measurement result of waveform of delay compensated active rectifier. And, Fig.4.22 shows measured VCR of the active rectifier. Measurement was done without high-side switches. Diode was used as high-side switches. Measured VCR and simulated VCR in high resistances are almost equal, but measured VCR in low load resistance is lower than simulation results. It is assumed that compensation was not perfectly applied.
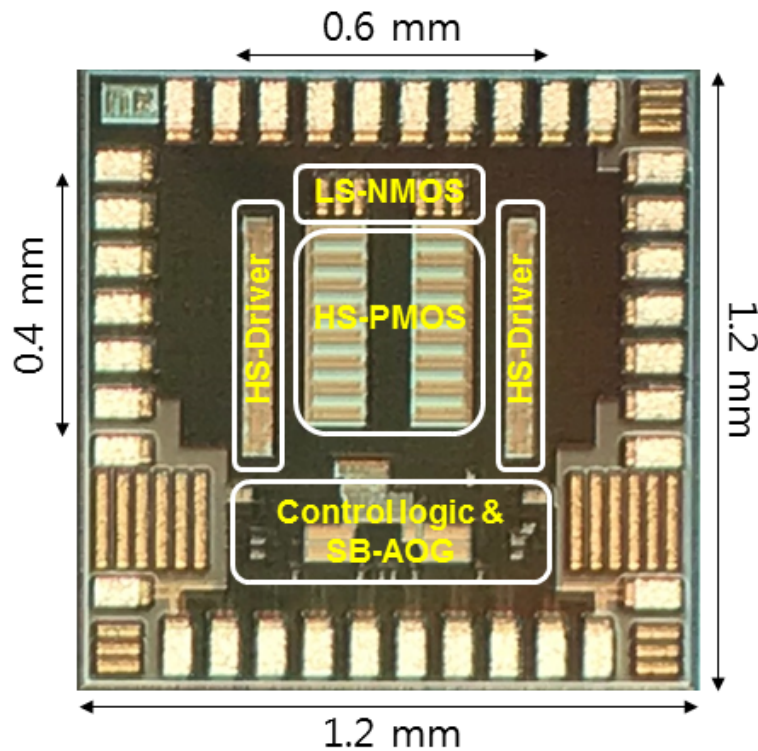
Fig.4.20. Chip microphotograph of the active rectifier.
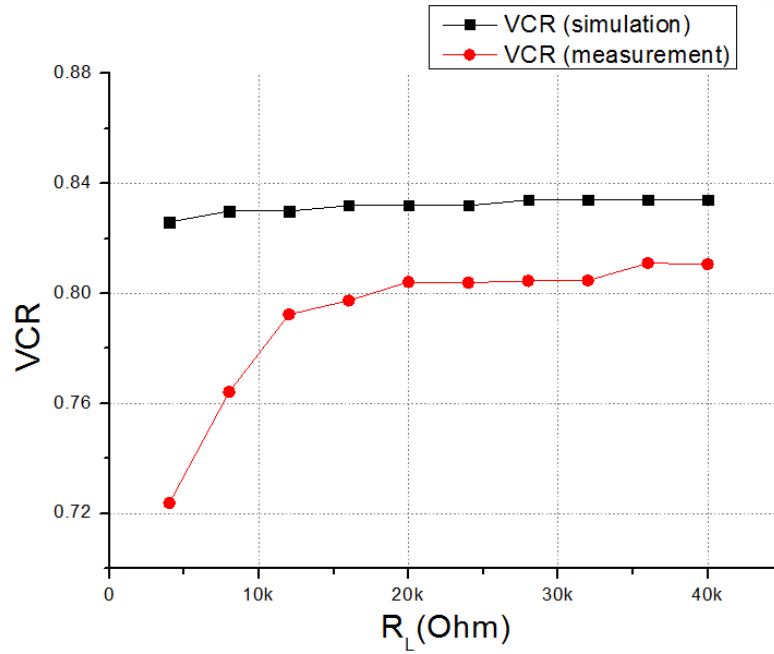
Fig.4.21. Measured waveforms of delay compensated active rectifier at V_{OUT} = 5V.
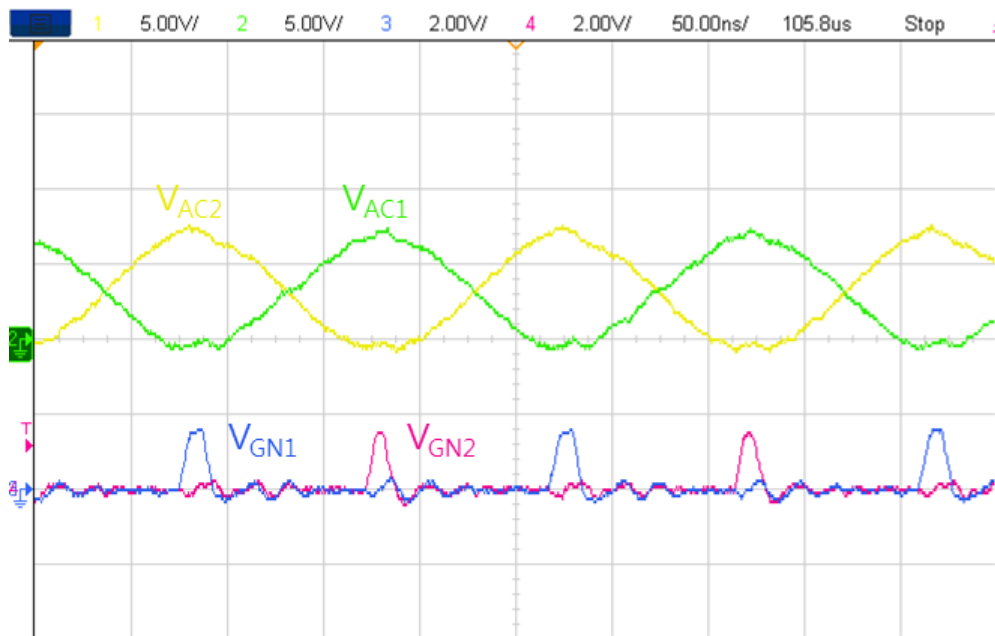
Fig.4.22. Measured VCR under load resistance variation at V_{OUT} = 5V.

4.5 Bootstrap-capacitor-less DCM-VOT buck converter

4.5.1 Background

As the population ages and the welfare is promoted, researches on BIMD are actively being carried out, and products providing more various functions are being released. On the other hand, due to these various functions, the power consumption of the BIMD is increased, so that the primary battery alone cannot provide sufficient power and the limited life time forces the patients to pay additional cost and suffering only for the power supply of the BIMD.

Wireless power transfer technology is a technology which has been making remarkable progress mainly in wireless charging for personal portable devices and wireless charging of electric vehicles. Convergence of WPT and rechargeable battery can extend the life time of the BIMD and reduce the suffering and the cost of battery replacement. It has the effect of increasing the capacity of the battery by indirectly increasing the duration of the battery.

A MR-WPT is an attractive solution to extend battery life for space-limited applications such as BIMD. However, MR-WPT has a property that voltage gain changes when there is coupling variation caused by misalignment or distance variation. Especially, when the receiver coil is smaller than the transmitter, coupling change results in larger voltage gain variation than where identical coils are used. Therefore, a challenge for MR-WPT for space-limited application is that receiver must operate safely while coupling variation occurs. Previously, [4.10] offered wireless feedback solution to provide stable rectified voltage to the load. However, regulating rectified voltage through wireless communication is only possible in limited distance variation and it cannot respond safely when coupling condition varies rapidly due to its slow response. Therefore, additional regulator is required to supply stable voltage where coupling condition is changing rapidly.

In the environment where the voltage conversion ratio changes widely, a switching converter is more efficient than a linear converter because switching converter has higher PCE than linear converter when the voltage conversion ratio is large. However, the switching converter requires several external components, such as an inductor, a storage capacitor, a bootstrap capacitor, and components for frequency compensation. Use of external components should be avoided for BIMD because implant space is limited. An inductor and a storage capacitor are essential to the switching converter and cannot be removed, but a bootstrap capacitor and components for frequency compensation can be removed. A pulse width modulation, which is widely used as a control method in converters, uses a fixed switching frequency to ensure a clean output, but compensation components are required and efficiency is very low in light loads. On the other hand, pulse frequency modulation (PFM) has relatively noisy output due to fluctuating switching frequency, but it does not need compensation components and shows high efficiency in light loads. Therefore, PFM control is

suitable for space constrained applications such as BIMD.

This section introduces a DCM PFM buck converter providing 1.8V output with input voltage varying from 3-to-12V. The presented buck converter supports safe operation at the receiver while coupling variation occurs. An external bootstrap capacitor for high-side driver is removed by only using a standalone level shifter as the driver to reduce receiver size. A momentary power consuming (MPC) technique is applied to the standalone level shifter to increase PCE. In addition, dead-time-based off-time calibration circuit (DOCC) is proposed to further increase PCE by reducing the low-side conduction loss.

4.5.2 Over architecture
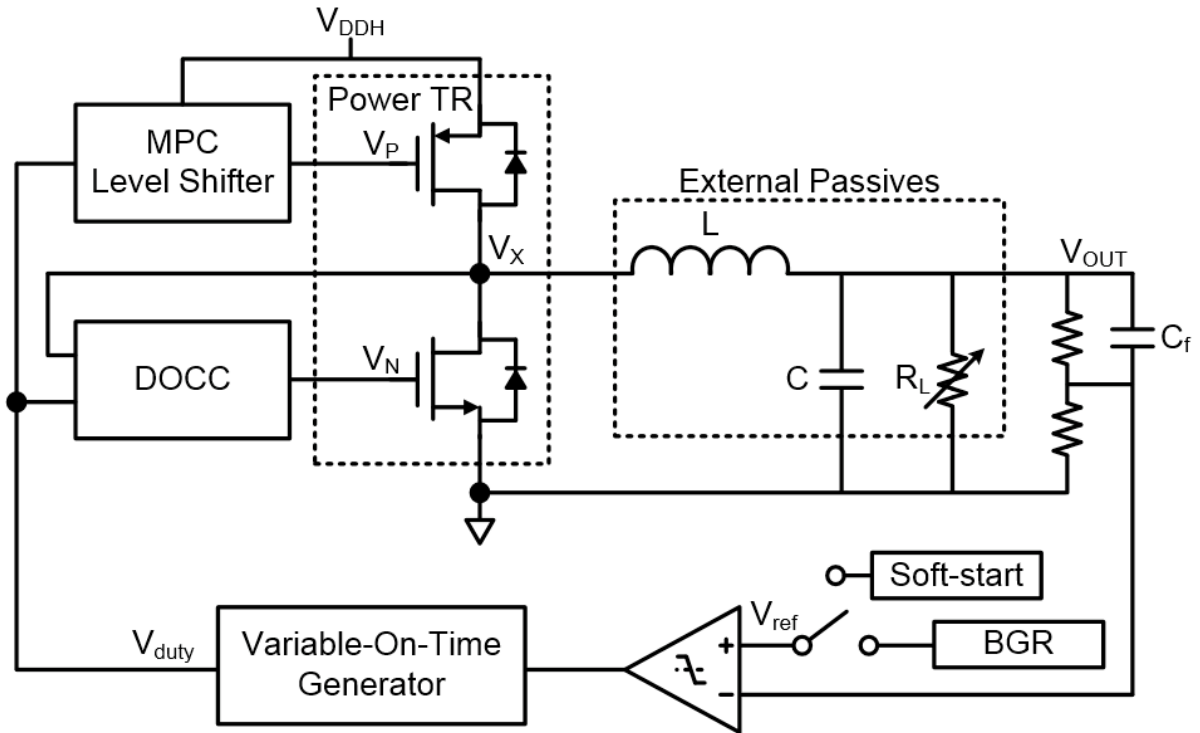
Fig.4.23. System architecture of DCM-VOT-converter.

The overall proposed system architecture of DCM-PFM buck converter is shown in Fig.4.23. The converter consists of standalone level shifter, DOCC, comparator, variable on-time generator, soft starting circuit, linear regulator, and bandgap reference. A linear regulator using V_{DDH}, which is an input voltage which can vary with the variation of the coupling, as the power supply is used to initialize converter settings and operate the control circuit. It is temporarily used before the converter is stabilized. When the soft start is ended and output of the converter is stabilized, the linear regulator is deactivated, and output of the converter supplies power to the control circuits. Bandgap reference is designed to use V_{DDH} as the power supply to operate regardless of the power reception state of the receiver. Since the converter operates in PFM mode, total size of the converter is reduced due to lack of compensation block. However, an integrated 10pF capacitor, C_f, is used to improve noise immunity by increasing ramp signal with relatively small output ripple. Basically, the on-time generator produces constant-on-time (COT) at certain V_{DDH}, but it provides variable-on-time (VOT) when V_{DDH} changes. An inductor and a storage capacitor are only used externally. The high-side NMOS switch, which is used to reduce conduction loss and size, is replaced with PMOS switch and eliminated the need for an external bootstrap capacitor.

122
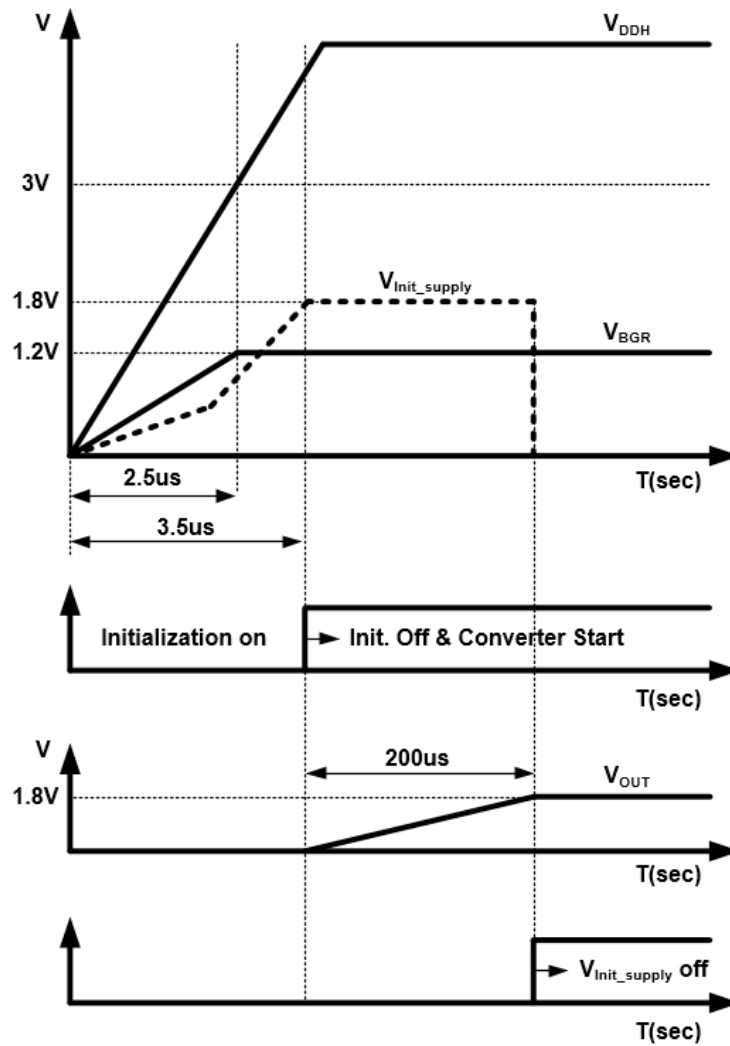
Fig.4.24. Timing diagram of initial operation sequence of the proposed converter.

Fig.4.24 shows the timing diagram of the initial operation sequence of the proposed converter. First, the output of bandgap voltage reference, V_{BGR}, rises when an input voltage is applied. As V_{BGR} rises, a linear regulator begins to operate. The output of linear regulator, V_{init_supply}, is settled after V_{BGR} is settled. Before V_{init_supply} reaches the desired voltage, the initialization circuit limits the operation of the converter control circuit. When V_{init_supply} becomes the desired voltage, the initialization circuit is turned off and the converter control circuit starts operating. At the same time that the converter control circuit starts to operate, the soft starting circuit controls the output of the converter, V_{OUT}, to prevent excessive current. Finally, when V_{OUT} reaches the desired voltage, the linear regulator is deactivated and the output of converter is used as the power supply.

4.5.3 Building blocks

4.5.3.1 Proposed high-side driver (MPC level shifter)

(a)   (b)
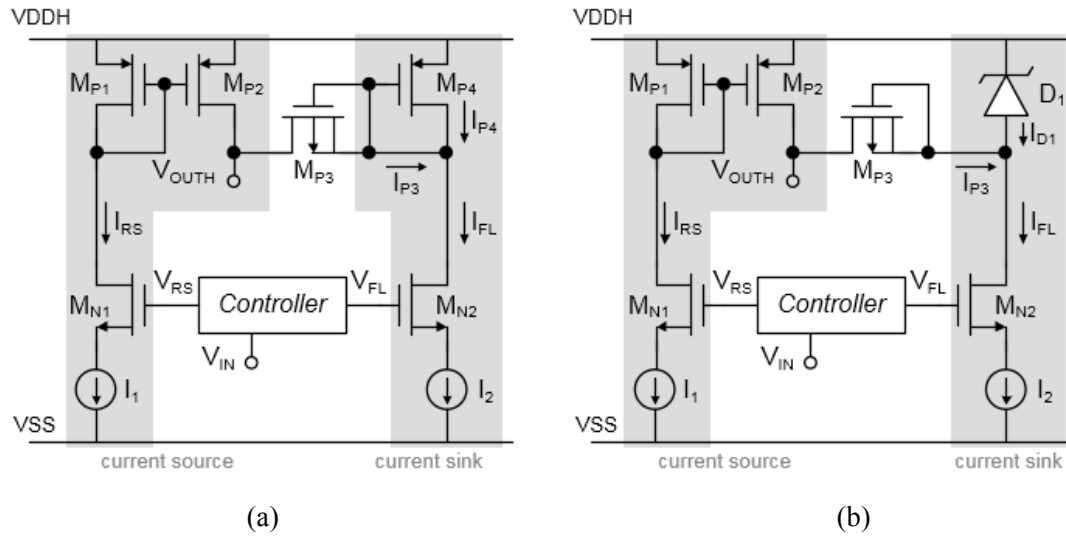
Fig.4.25. Schematic of level shifters: (a) conventional MPC level shifter, and (b) proposed MPC level shifter.
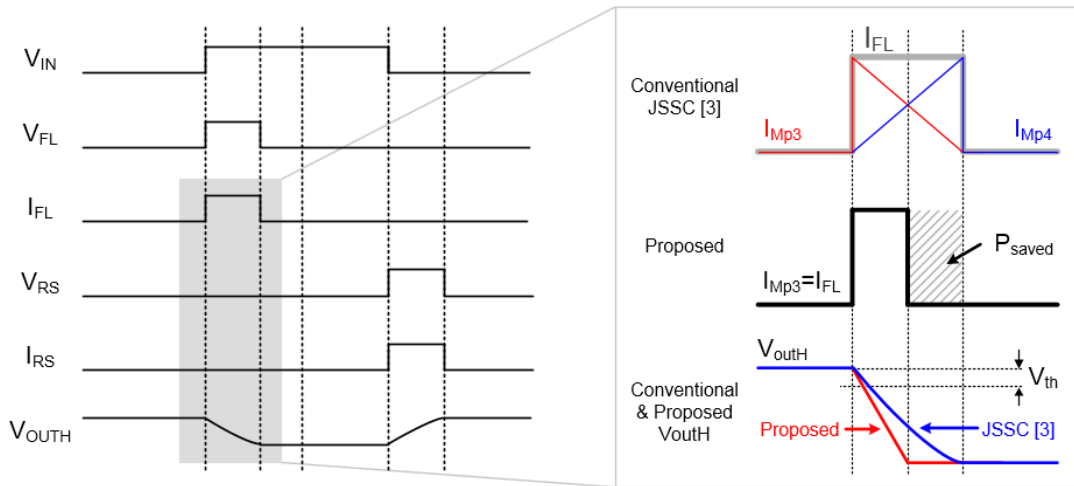
Fig.4.26. Timing diagram of the MPC level shifters. The properties of conventional and proposed level shifter are compared.

Several drivers were used to convert low reference signal to high reference level for driving high-side MOS switch. The most popular high-side driver is driver with bootstrap capacitor, which is used when the driving target is NMOS. The low on-resistance of NMOS compared to PMOS leads to smaller size, resulting in low gate capacitor. However, the capacity of bootstrap capacitor should be much higher than the amount of charge consumed to drive high-side NMOS to maintain stable supply voltage. Therefore, bootstrap capacitor is usually used in the capacity of nF. The sub nF capacitor can be integrated on the chip, but it still occupies large area. Hence, bootstrap technique is not suitable for

BIMD.

The high-side ground method or stand-alone level shifter can be used for driving high-side PMOS. The high-side ground method is similar to bootstrapping except that an additional voltage generator is needed for extra ground. This method has poor supply voltage range by fixed extra ground.

The stand-alone level shifter itself also is used as a high-side driver. The stand-alone level shifter changes low reference level swing to high reference level with same magnitude. It can drive MOS switch without external capacitor or additional ground. Also, the level shifter can operate properly even when supply voltage varies. However, the general level shifter consumes power continuously in contrast to the inverter chained buffer. The static power consumption deteriorates PCE of the converter.

To resolve large static current problem in level shifter, capacitively coupled level shifter (CCLS) [4.11], and MPC level shifter [4.12] were introduced. However, CCLS needs a large capacitor which is almost 10 times larger than gate capacitance to suppress charge sharing effect. As a result, it is not compatible with space-limited applications. The conventional and the proposed level shifter using MPC technique are shown in Fig.4.25. The MPC level shifter is divided into current sinking part and current sourcing part. These two parts are isolated by body diode of M_{P3}. Each parts are only operated when the output of level shifter needs transition. As a result, a large static current is eliminated, and a dynamic current is dissipated when the transition is occurred. [4.12] uses diode-connected M_{P4} to regulate maximum voltage drop of the output, V_{OUTH}. To drop V_{OUTH}, M_{N2} is turned on and I_{FL} is conducted. I_{P3} and I_{P4} gradually decreases and increases, respectively. The sum of I_{P3}, and I_{P4} is I_{FL}. I_{P3} is the current which drops V_{OUTH}. However, I_{P4} takes current away from I_{P3} which increases the transition time. A technique to reduce transition time while maintaining maximum voltage drop regulation is proposed. The diode-connected M_{P4} is replaced with a zener diode. By using the intrinsic characteristic of a zener diode that extremely small current flows before the reverse breakdown voltage, I_{P3} sinks the current equal to I_{FL}. If I_{FL} is regulated by current source I_2, the transition time is reduced by 50%, and the power dissipation of the level shifter also decreases in proportion to the transition time reduced. A timing diagram of the MPC level shifters is shown in Fig.4.26, and reduction of power consumption can be intuitively understood from Fig.4.26. A comparison of power consumption of the MPC level shifters at duty cycle of 10% and 5% are shown in Fig.4.27. It is extracted from cadence simulation. The results show that proposed MPC level shifter has low power consumption when the duty cycle is low. However, the power reduction ratio increases as the duty cycle increases.
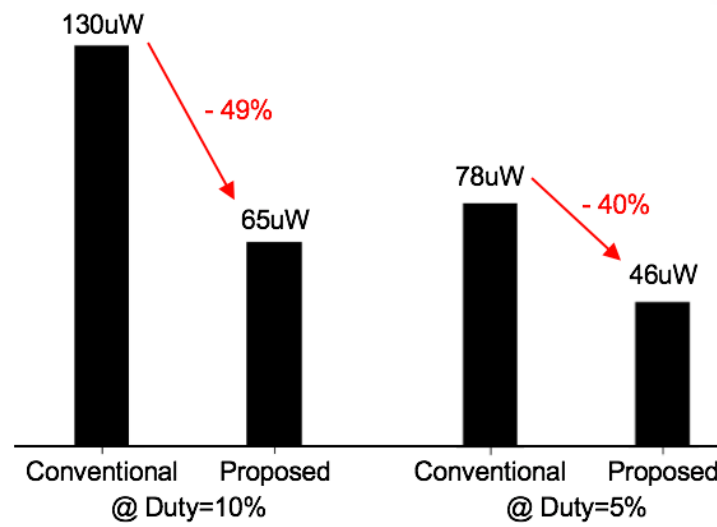
Fig.4.27. Power consumption comparison between conventional and proposed MPC level shifter at duty cycle of 10% and 5%.

4.5.3.2 Proposed low-side compensator (DOCC)

Conduction loss of the low-side diode in the converter is a factor that reduces PCE. A synchronous converter using a transistor switch rather than a diode is commonly used to eliminate diode conduction losses. It reduces the conduction loss compared to the diode by using the on-resistance of the transistor. The synchronous converter utilizes zero-voltage-switching to efficiently control the transistor switch.

While using ZVS, propagation delay of comparator and buffer results in a reverse current causing power loss. To eliminate the reverse current, a high speed comparator or a turn-off timing adjustment technique for switch control should be used. The concept of the proposed switch control technique to eliminate the reverse current is subtracting the delay time of the comparator and buffer from the switch control time. Since it is impossible to subtract time, the proposed switch control technique is to turn-off the switch as early as the delay time of the comparator and buffer.

Fig.4.28 shows the DOCC which compensates the delay of the low-side driver and reduces power loss caused by the reverse current. The DOCC provides an intentional offset voltage proportional to the delay that can alter the comparison timing resulting in zero reverse current. DOCC consists of buffers, comparators, dead-time to DC converters (DTDC), error amplifier, and V-I converter. The buffer is used to isolate offset added signal from the original compared signal. A function of DTDC is converting the time difference to DC voltage.
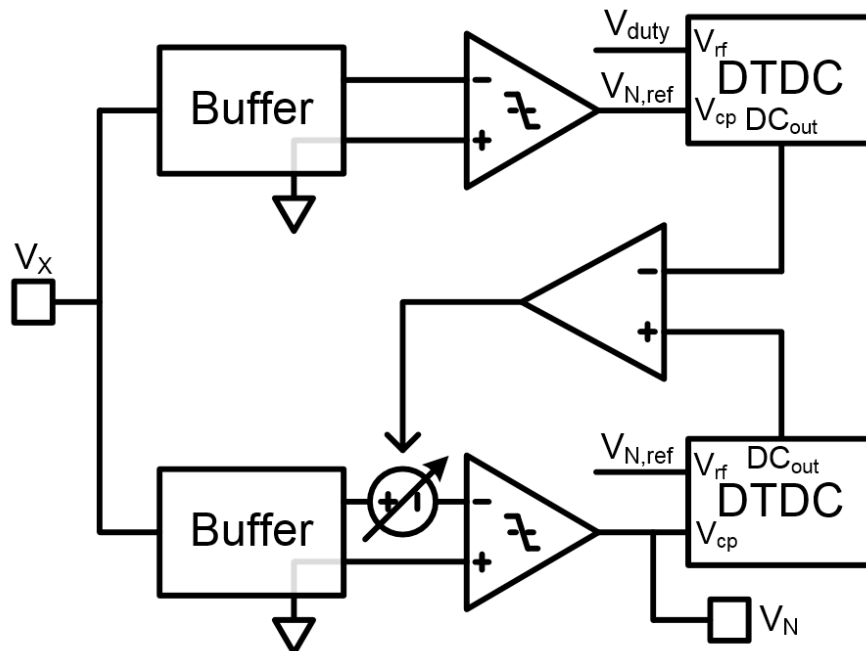
Fig.4.28. Block diagram of dead-time-based off-time calibration circuit (DOCC).
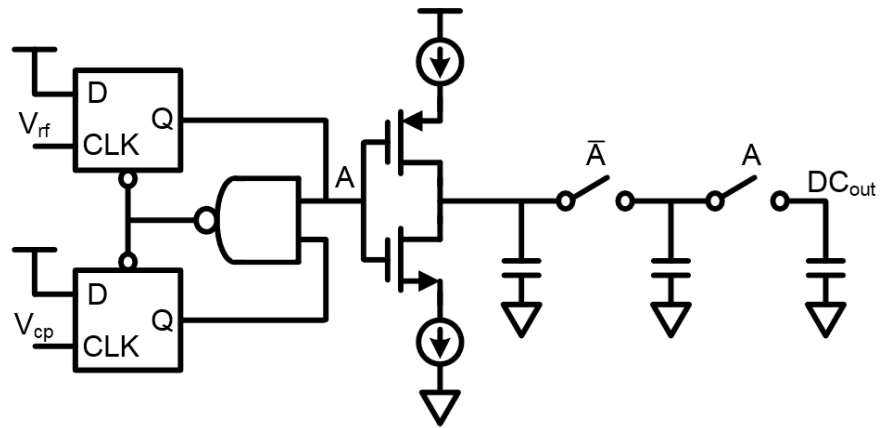
Fig.4.29. Schematic of dead-time to DC converter (DTDC).
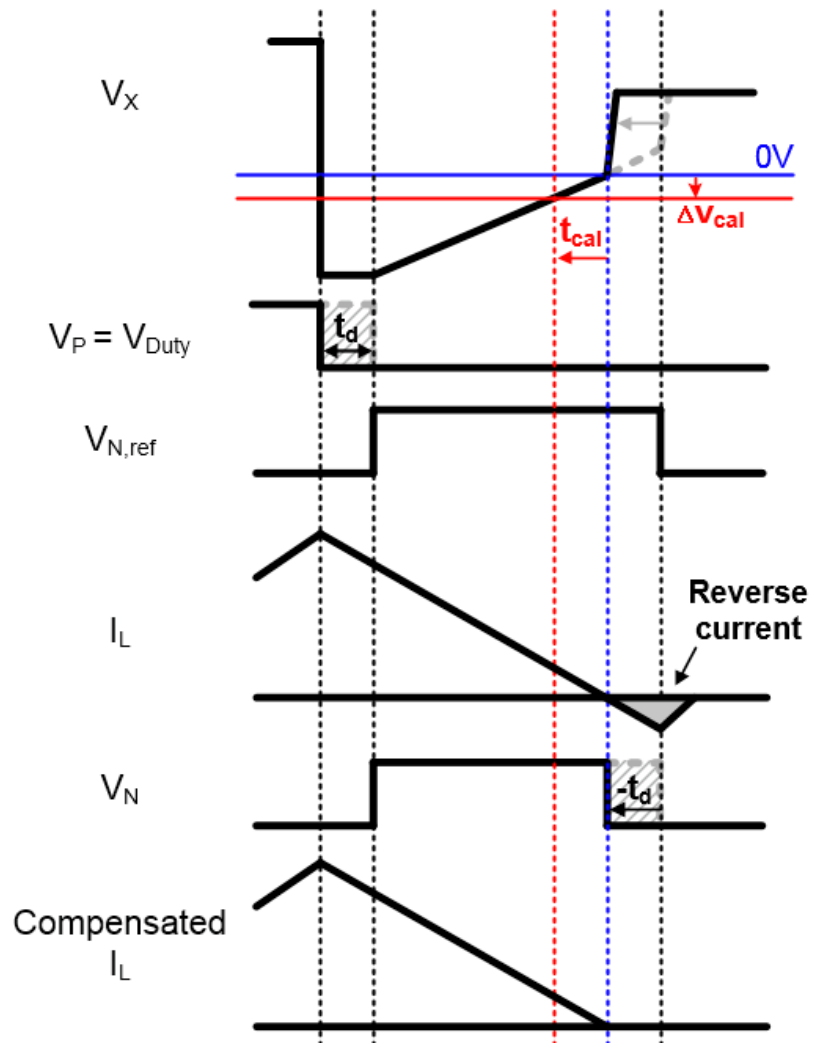
Fig.4.30. Timing diagram of DOCC.

A schematic of DTDC is shown in Fig.4.29. DTDC is originated from phase frequency detector (PFD) and charge pump which are commonly used in phase locked loop. However, DTDC differs from the usage in phase locked loop. DTDC measures time difference with PFD and only a single output is connected to charge pump. The charge pump generates DC voltage proportional to the time difference. A sample-and-hold circuit is used to store the DC voltage and isolate a capacitor for storing DC voltage from the output of charge pump. A timing diagram of DOCC is shown in Fig.4.30. A calibration reference is generated using a replica of circuit for ZVS. DTDC in replica converts the time difference between off-edge of V_{duty} and on-edge of $V_{N,ref}$ to DC voltage. The time difference between each edge is a dead-time to eliminate shoot-through current, and it represents the delay of the driver, t_d. The DTDC in main signal path converts time difference between off-edge of V_N, and $V_{N,ref}$. The error amplifier and V-I converter generate offset, and add it to the buffer. Negative feedback to generate offset, ΔV_{cal}, turns V_N off earlier than $V_{N,ref}$ by the amount of the dead-time. The comparator has additional delay which is proportional to the transition speed of the input signal. Therefore, delay occurred at switch off-period is larger than on-period. However, the dead-time includes propagation delay of level shifter which can compensate the delay difference caused by input transition speed. The DOCC calibrates for fixed dead-time, but this ensures a PCE rise through safe reverse current rejection.

4.5.3.3 Variable-on-time generator
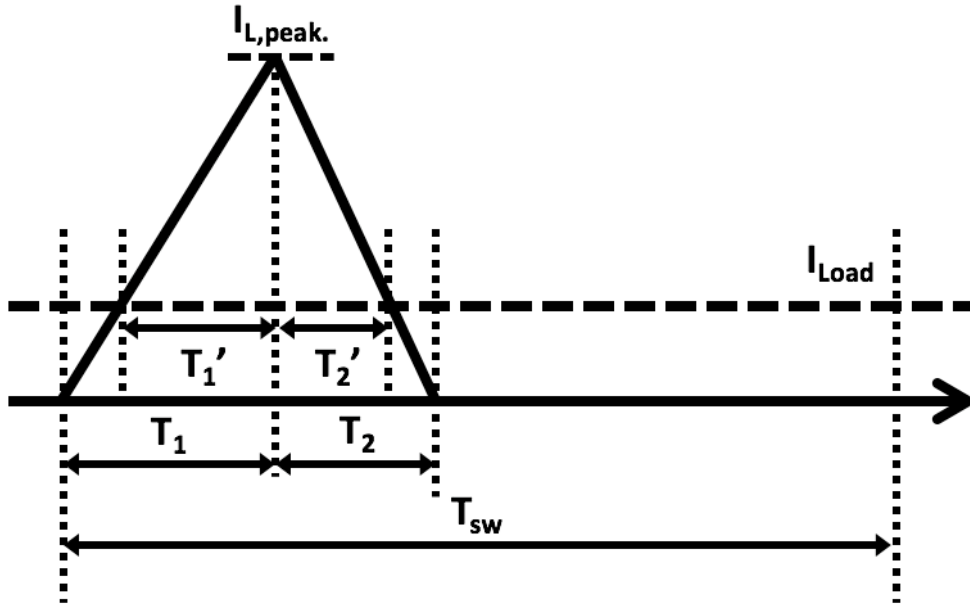
Fig.4.31. Waveform of inductor current.

PFM is a method of controlling the output voltage by changing the pulse frequency when the input voltage or the load changes. It is easier to design than pulse width modulation and shows high PCE in light load. There are several ways to implement PFM [4.13]. COT is a method of fixing the time for turning on the high-side switch, and determining the period of operation of the switch by the change of the output voltage. When the output voltage falls below the desired voltage, the comparator activates the pulse generator to operate the converter. The pulse generator is deactivated after the converter has been running for the set time. When the output voltage becomes lower than the reference voltage, it is activated again to operate the converter. VOT is a method of varying on-time in inverse proportion to the input voltage of converter, but the on-time is constant in the certain input voltage. The on-time of VOT is determined by f (V_{in}-V_{out}), where V_{in} is input voltage of the converter, V_{out} is output voltage of the converter.

Generally, VOT shows better performance over a wide input range than COT [4.14]. To compare the performance between COT and VOT, key design parameter is derived such as peak inductor current ($I_{L,peak}$), switching frequency (f_{sw}) and output voltage ripple (V_{ripple}). The waveform of inductor current is shown in Fig.4.31. Key parameters derived from Fig. 12 are

$$I_{L,peak} = \frac{V_{in} - V_{out}}{L} T_1 \qquad (4.16)$$
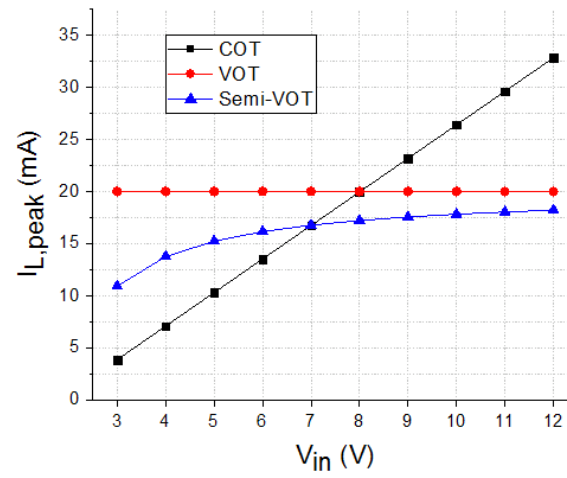
(a)
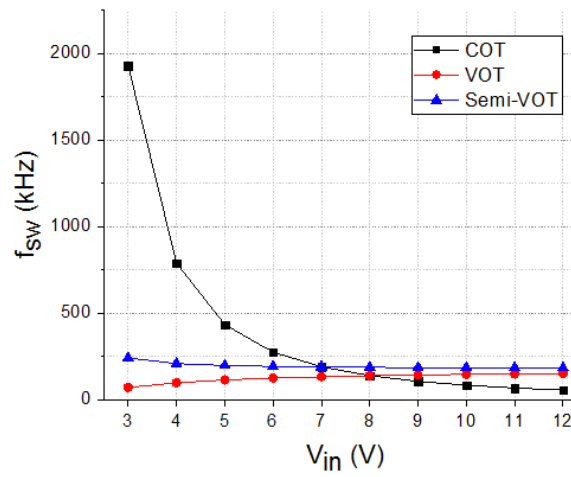
(b)
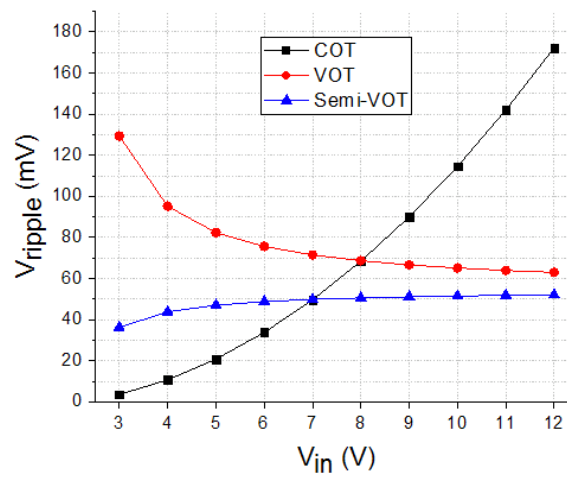
(c)

Fig.4.32. Performance comparison between COT, VOT, and semi-VOT: (a) peak inductor current, (b) switching frequency, and (c) output voltage ripple.

131

$$f_{sw} = \frac{2I_{out}}{I_{L,peak}^2 L\left(\frac{1}{V_{in}-V_{out}}+\frac{1}{V_{out}}\right)} \tag{4.17}$$

$$V_{ripple} = \frac{(I_{L,peak}-I_{out})^2(T_1+T_2)}{2C_{Load}I_{L,peak}}. \tag{4.18}$$

where L is an inductance, I_{out} is output current of the converter, T_1 is on-time of high-side switch, T_2 is on-time of low-side switch, and C_{Load} is a capacitance of storage capacitor.

Performance comparison between VOT and COT is shown in Fig.4.32. The rate of change of each parameter is small when the converter is controlled by VOT while the input voltage changes. In particular, the peak inductor current has a fixed current value even if the input voltage changes. However, when the input voltage is small, the switching frequency is low causing large ripple voltage. Even if WPT for BIMD should support a wide input voltage range, the main operating voltage range is a low voltage range. Therefore, a control method that has better performance when the input voltage is low should be employed. In this section, a VOT that on-time is determined by $f(V_{in}-V_{gs})$ is employed, and it is called a semi-VOT for classification. The semi-VOT has small variation rate of each parameter even when input voltage is changed, and output voltage ripple is small due to high switching frequency when input voltage is low.

Fig.4.33. Schematic of variable-on-time generator.

Fig.4.33 shows a schematic of the VOT generator. The bias current, I_{on}, is determined by the voltage across the resistor, R_{on}, and the voltage across R_{on} is V_{in}-V_{gs}. When the output of the comparator, V_{CMP}, operates D flip-flop, the bias current charges the on-chip capacitor, C_{on}, and when the voltage of the capacitor exceeds the threshold voltage, the VOT generator is deactivated by resetting the D flip-flop. The output signal from the D flip-flop is the on-time signal, and the on-time of the signal is defined by the following equation:

$$T_1 = C_{on}\frac{V_{th}R_{on}}{V_{in}-V_{gs}}.$$

(4.19)

4.5.3.4 High voltage bandgap reference

A voltage reference circuit for the linear regulator and the converter control circuit operates before the other circuits using the input voltage of the converter as a power source. The input voltage of the converter varies from 3 to 12 V, and a two-stage bandgap voltage reference circuit is designed to operate at a high voltage. The schematic of two stage bandgap reference circuit is shown in Fig.4.34. The output of 1st bandgap reference circuit is used as voltage supply of the 2nd bandgap reference circuit. The output of a normal bandgap reference circuit is less than 1.5V because the V_{BE} of the bipolar transistor is from 0.6 to 0.8V. For the operation of the 2nd bandgap reference circuit, the minimum output of 1st bandgap reference circuit is made around 3V by using four cascaded bipolar transistors, Q3. The output branch of the 1st bandgap reference circuit consumes more current than other branches for temperature compensation of 4 cascaded bipolar transistors. The 2nd bandgap reference circuit, which receives the output of the 1st bandgap as a power supply, is designed as a normal bandgap circuit and the output, V_{BGR}, is around 1.2 V.
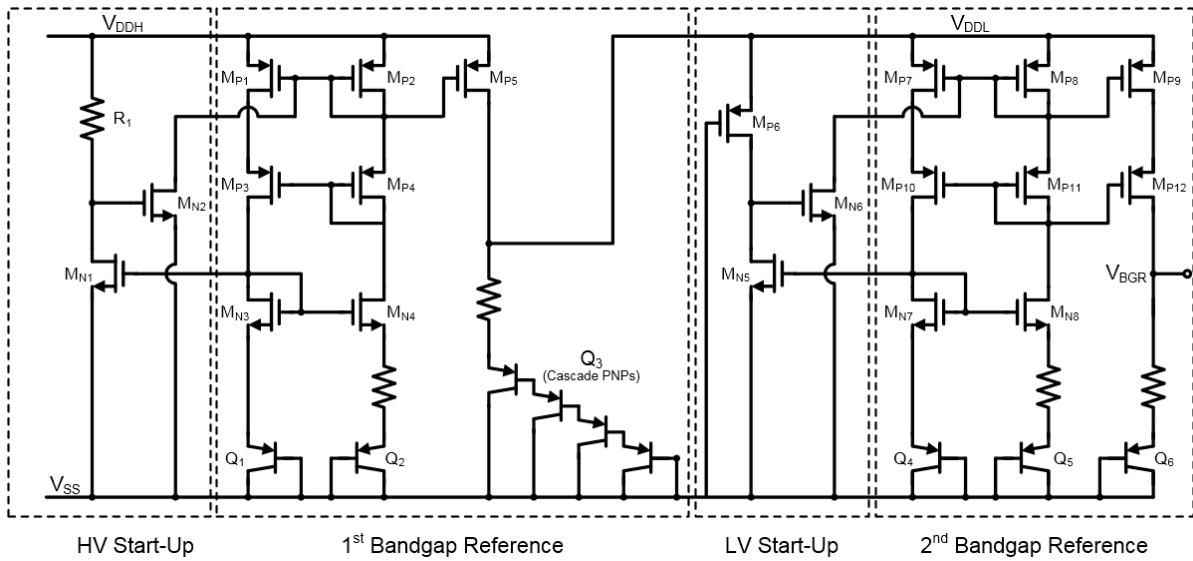
Fig.4.34. Schematic of high voltage two stage bandgap reference circuit.

4.5.3.5 Linear regulator

The linear regulator is used to supply power to the converter control circuit before the converter operates, and it is shown Fig.4.35. The bias current required for the regulator is a self-bias current using a resistor, R_1. The HRI device provided by the BCD process is utilized for R_1, and an on-chip capacitor, C_f, and resistor, R_f, are used for frequency compensation. The output capacitor, C_{out}, is used externally. When the output of the converter is stabilized and the output of the converter becomes equal to the output voltage of the linear regulator, the linear regulator is deactivated. To deactivate the linear regulator, M_{N6} is turned on to turn off M_{N1}, M_{N2}, and M_{N5} that supply a biasing current to the regulator. The reference bias current flowing through R_1 when the linear regulator is deactivated flows to M_{N6}, but it does not influence on converter efficiency because it is too low.

Fig.4.35. Schematic of high voltage linear regulator.

4.5.4 Measurement results

Fig.4.36. Chip microphotograph.

The DCM PFM buck converter with MPC level shifter and DOCC is implemented in a 0.18-μm BCD process, and it occupies an active area of 0.68 mm². Fig.4.36 shows the chip microphotograph. The converter operates at switching frequency under 750 kHz and it can support input voltage in the range of 3–12 V. It provides a regulated output voltage of 1.8V with output current from 20 μA to 3 mA. The external inductor and capacitor values of 47 μH and 100 nF are used, respectively. Fig.4.37 is measurement setup to check performance of the converter. Fig.4.38 shows measured waveform of DOCC from minimum V_{DDH} to maximum V_{DDH}. DTDC generates time difference of V_P and $V_{N,ref}$, and $V_{N,ref}$ and V_N, properly, resulting in reverse current prevention. Measured waveform of the converter under various conditions are shown in Fig.4.39 and Fig.4.40. The switching frequency changes according to the input voltage and the output current. The output ripple voltage become higher when input voltage increases or output current decreases. Fig.4.41 is a WPT configuration measurement setup to verify the operation of the converter in noisy environment. Coils shown in Fig.4.9 are used. The rectifier shown in Fig.4.20 is used to construct WPT environment. Measurement results of DOCC in noisy environment is shown in Fig.4.42, and Measurement results of the converter in noisy environment is shown in Fig.4.43. From the results, proper operation of the converter with proposed techniques is confirmed. Measured efficiency of the converter is shown in Fig.4.44. Average

efficiency of the converter from 100 uA to 3 mA is 78 %. The efficiency of the converter starts to decrease from 100 uA. Performance summary and comparison is given in Table 4.3. Publications that supports below 5 mW is used for comparison. The presented converter supports widest input voltage range without bootstrap capacitor with highest efficiency below 5 mW as output power. The efficiency of [4.15] is higher than the converter, but it occupies much larger area with its bootstrap capacitor.
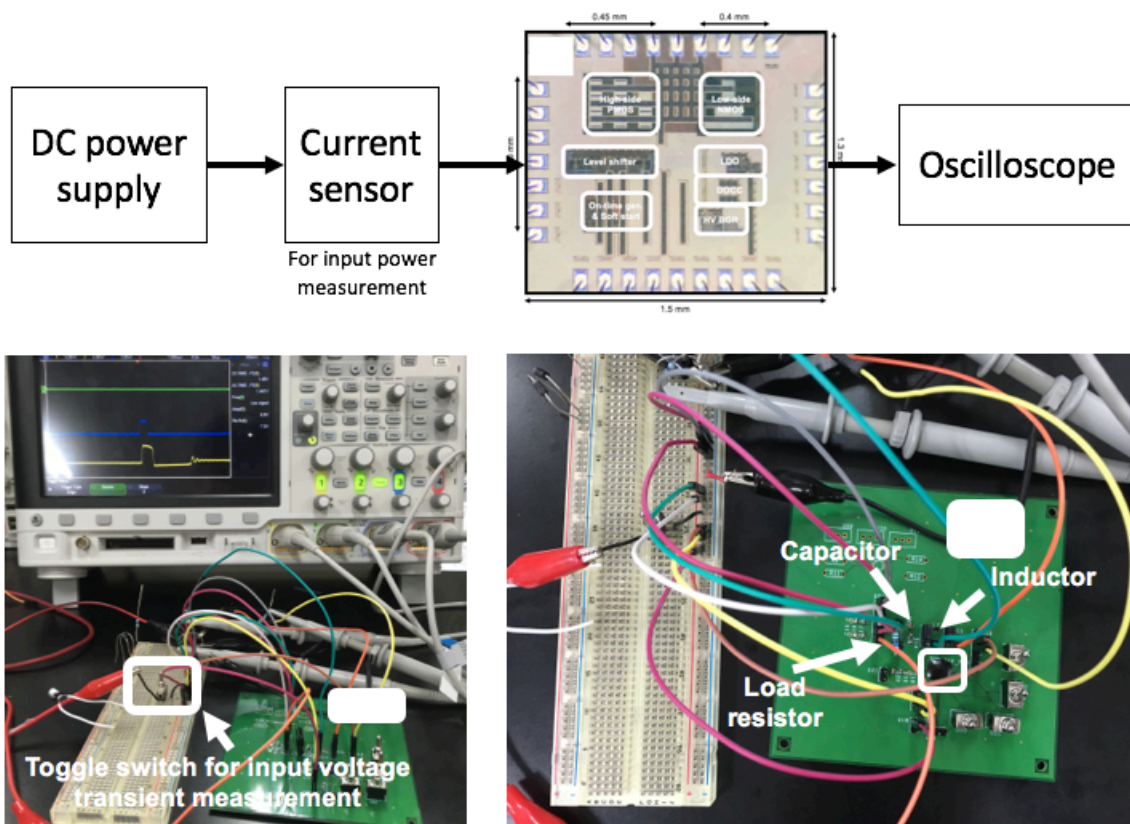
Fig.4.37. Measurement setup.
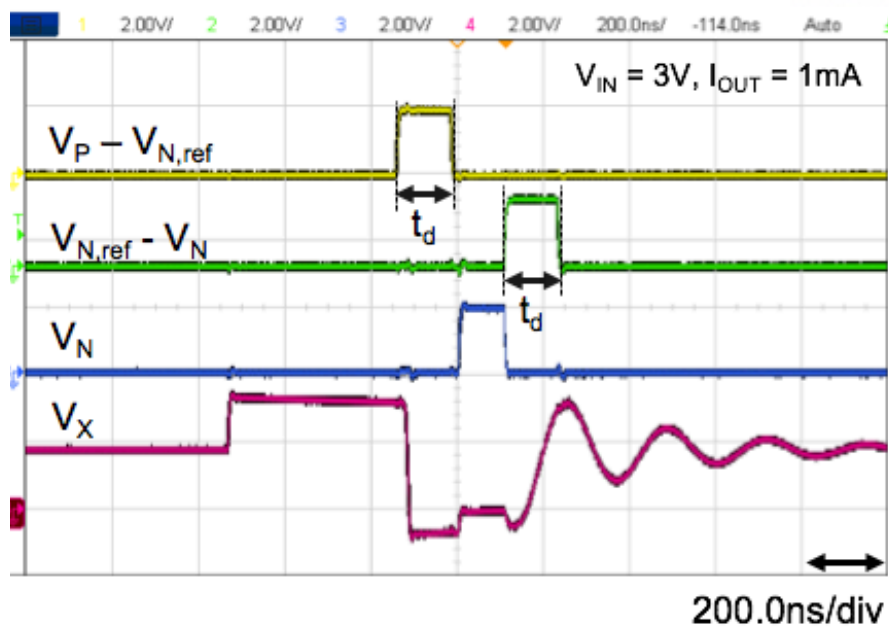
(a)
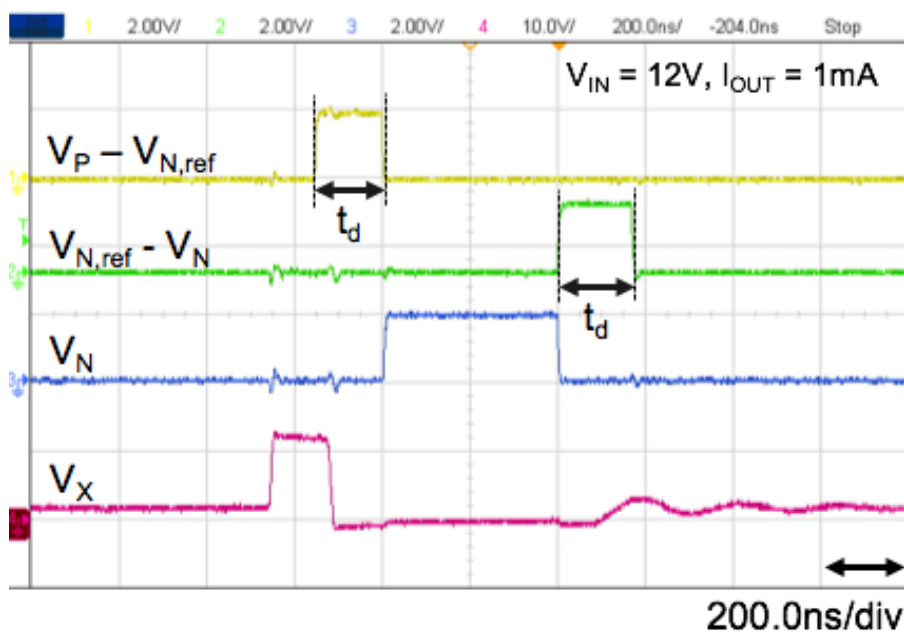
(b)

Fig.4.38. Measured waveforms of DOCC at I_{OUT} =1mA when V_{DDH} is: (a) 3V, and (b) 12V.
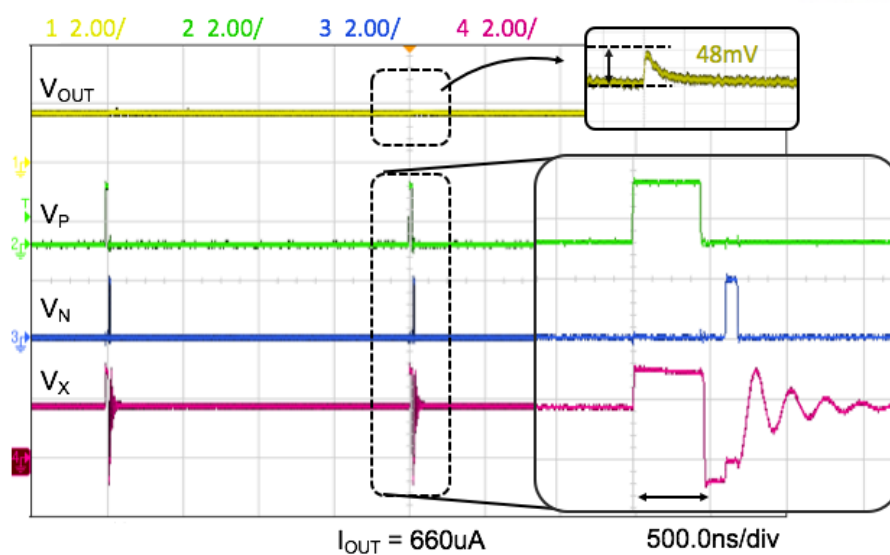
(a)
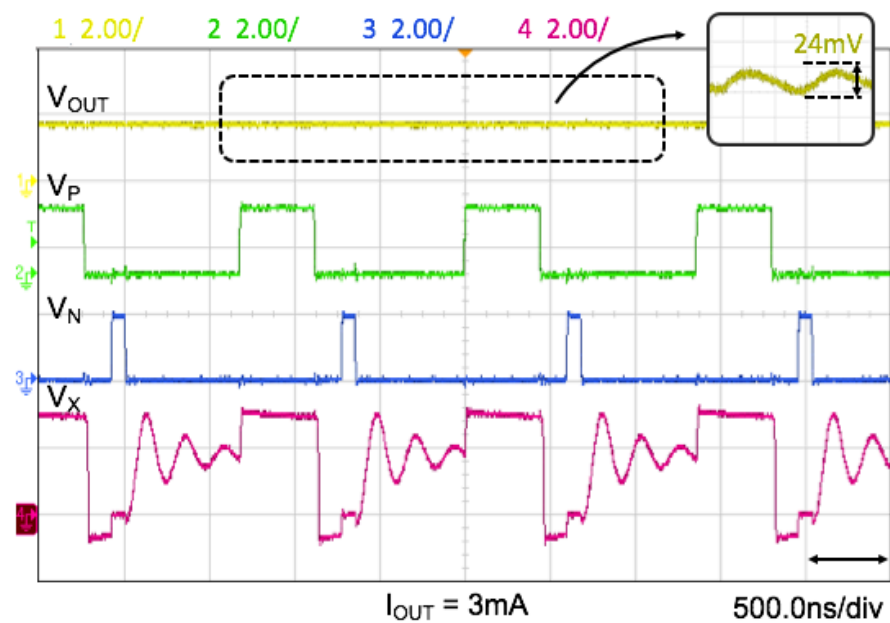
(b)

Fig.4.39. Measured steady-state waveforms of the converter when V_{DDH} is 3V: (a) I_{OUT} = 660uA, and (b) I_{OUT}=3mA.
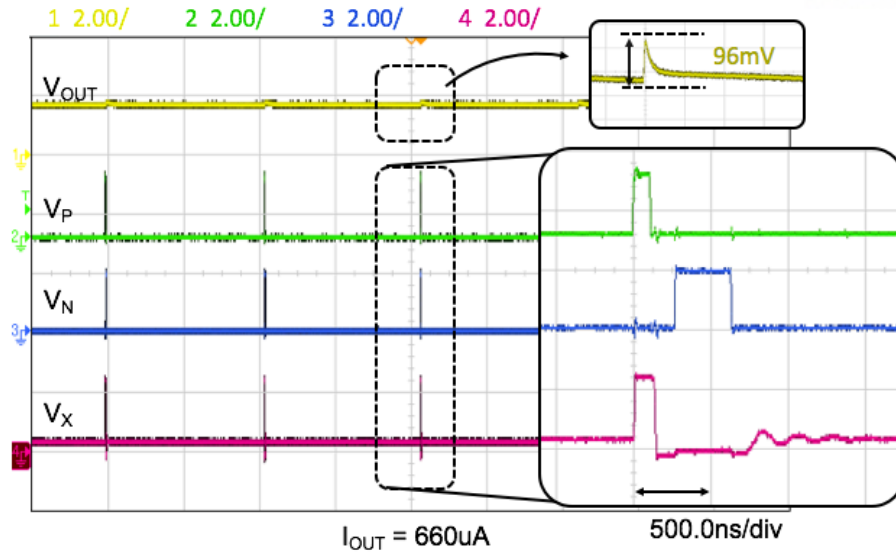
(a)
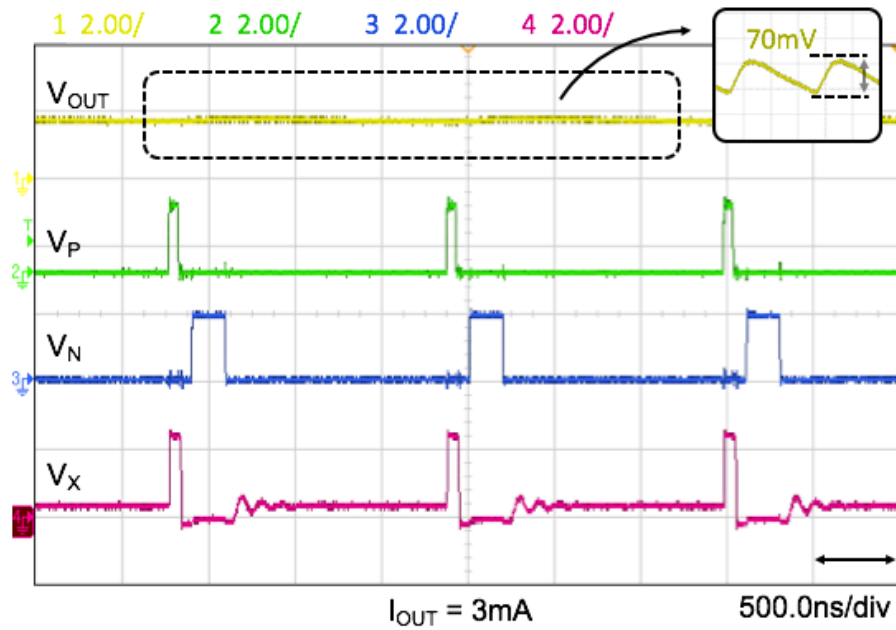
(b)

Fig.4.40. Measured steady-state waveforms of the converter when V_{DDH} is 12V: (a) I_{OUT} = 660uA, and (b) I_{OUT}=3mA.

Fig.4.41. WPT configuration to measure the converter in noisy environments.
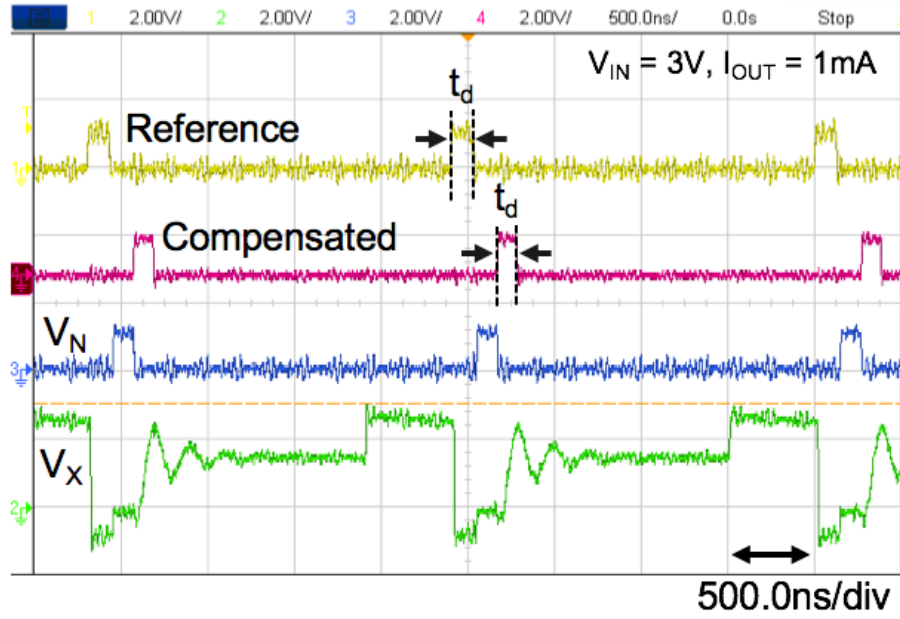
(a)
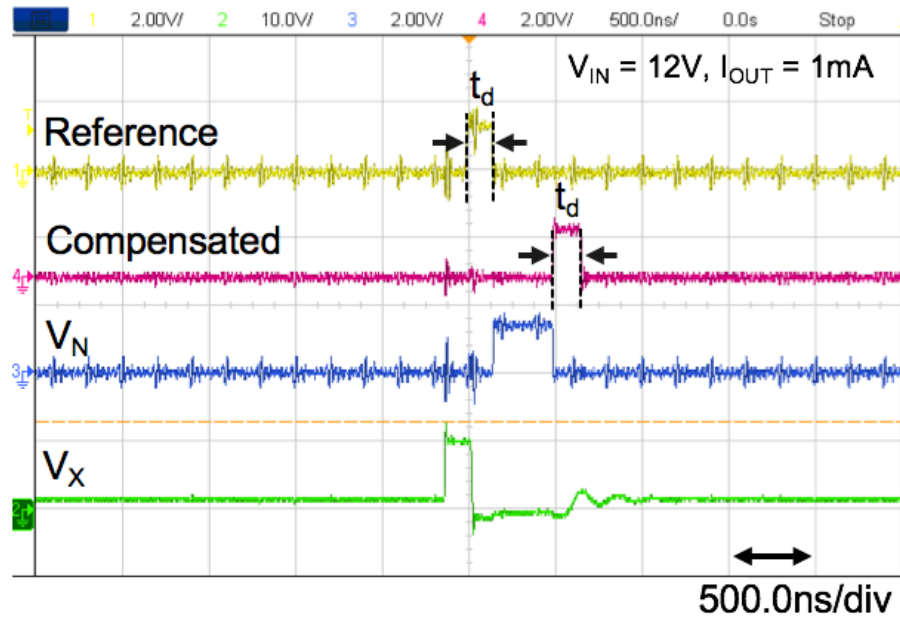
(b)

Fig.4.42. Measured waveforms of DOCC in WPT environments at I_{OUT} =1mA when V_{DDH} is: (a) 3V, and (b) 12V.
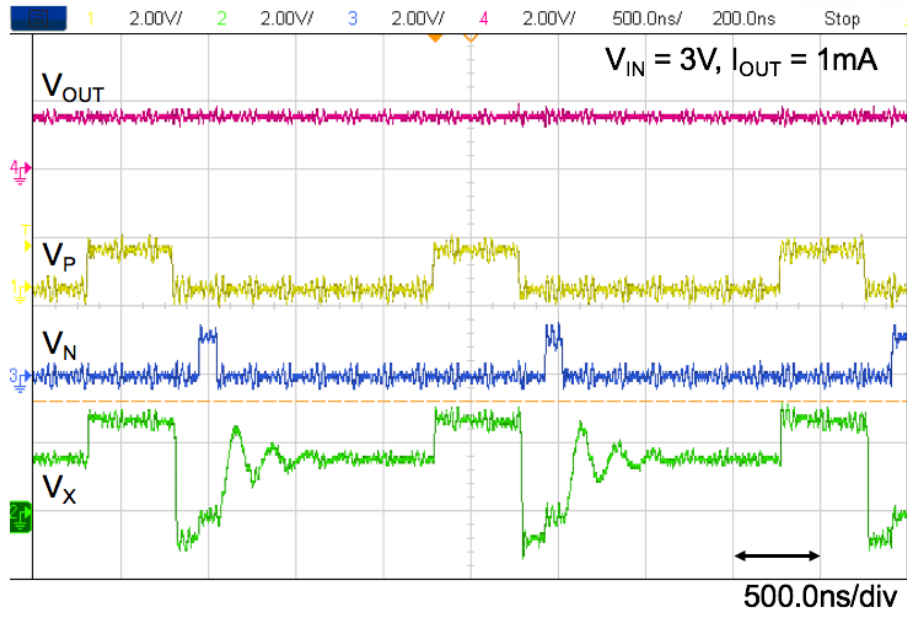
(a)
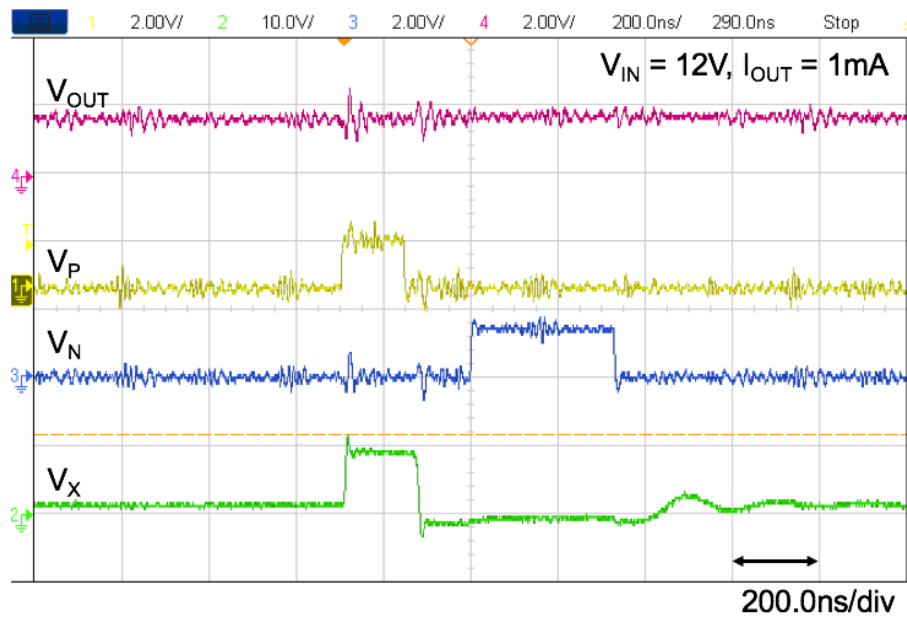
(b)

Fig.4.43. Measured steady-state waveforms of the converter in WPT environments when V_{DDH} is: (a) 3V, and (b) 12V.
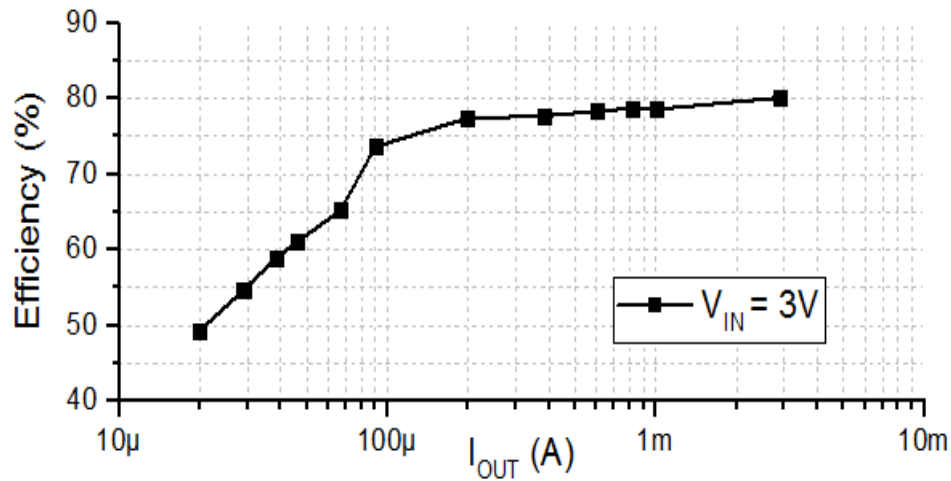
Fig.4.44. Measured efficiencies of proposed converter.

Table 4.3. Performance comparison

	[4.14]	[4.16]	[4.17]	[4.15]	This work
Technology	HV 250nm CMOS	500nm CMOS	55nm CMOS	45nm CMOS	180nm BCD
Operating method	PFM	PFM	DPWM	PFM+PWM	PFM
Input voltage [V]	3-5	1.4-4.2	1.5-3	2.8-4.2	3-12
Output voltage [V]	2.5	0.5	1.2	0.4-1.2	1.8
Output current	1mA-24mA	10mA-300mA	1-10m	20uA-100mA	20uA-3mA
Switching frequency	<350kHz	<200kHz	2MHz	<1.5MHz + 2 MHz	<750kHz
Inductor	10uH	1uH	3uH	10uH	47uH
Output capacitor	2.2uF	20uF	3uF	2uF	100nF
Peak efficiency	94	83	91.5	87.4	80.2
Max efficiency (below Pout=5mW)	75	70	79.3	85	80.2
Bootstrap capacitor	No	No	No	Yes	No

144

Chapter V
Conclusion

In this thesis, techniques to improve performances such as efficiency, size in WPT for BIMD are presented. The most significant property that needs to deal with in WPT for BIMD is the human health hazard with exposure in EM field. Too much exposure in EM field can cause several problems to the human body. In addition, large physical size of implantable devices can give foreign body sensation to the patients. To solve the problems mentioned above, a method to improve the PCE of the system to lower the radiated EM field and a method to reduce the size of the system to alleviate foreign body sensation are proposed. Additionally, a method to charge the Li-ion battery safely and efficiently with WPT is also proposed.

First, techniques that improve the performance of WPT using coils are presented. In 4 coil system, the power transfer efficiency is improved by using the coupling coefficient optimization in the transmitter. A load transformation circuit is used for the implanted receiving coil to improve the power transfer efficiency. The load transformation for efficiency enhancement has the additional effects of reducing the change in voltage gain, which can provide a simplification on the receiver circuit design.

In the receiver circuit, PCE is improved by reducing power losses. For the rectifier, an adaptive compensation technique that reduces the power loss due to the switch operation delay is realized. The realized technique is a method of optimizing the timing of switch operation based on sampling. The technique not only improves the efficiency but also increases voltage conversion ratio by preventing reverse current and maximizing conduction time, respectively. Likewise, the PCE in converter circuit is improved by reducing the power loss by adopting a DOCC circuit that prevents reverse current.

Furthermore, a high-side switch driver that reduces power consumption while eliminating bootstrap capacitors of converters and rectifiers is employed. The employed driver eliminates nF sized bootstrap capacitors, which can dramatically reduce the size of systems. Since the presented high-side driver does not have additional capacitors, the converter operates under wide input range with reduced area occupation. By making the proposed driver operate instantaneously, it reduces power consumption and further contributes to lower the PCE of the converter.

Techniques that are suggested in this thesis increase the power efficiency and reduce the size of the system in MR-WPT for BIMD. These techniques are able to be employed in any applications that use WPT as power supply requiring low power consumption and small size occupation such as internet-of-things.

REFERENCES

[1.1]   S. Y. Lee, C. H. Hsieh, and C. M. Yang, "Wireless Front-End with Power Management for An Implantable Cardiac Microstimulator", *Biomedical Circuits and Systems*, *IEEE Transactions on,* vol. 6, no. 1, pp. 28-38, Feb. 2012.

[2.1]   S.C. Thierauf, "High-speed Circuit Board Signal Integrity", p.56, Artech House, 2004 ISBN 1580538460.

[2.2]   S. Kim, S.A. Kim, G. Jung, K. Kwon, and J. Chun, "Design of a reliable broadband I/O employing T-coil", Journal of Semiconductor Technology and Science, vol. 9, no. 4, pp. 198-204, 2009.

[2.3]   K. A. Grajski, R. Tseng, and C. Wheatley, "Loosely-coupled wireless power transfer: Physics, circuits, standards", IEEE MTT-S International Microwave Workshop Series on Innovative Wireless Power Transmission: Technologies, Systems, and Applications, Kyoto, 2012, pp. 9-14.

[2.4]   P. Morrow, E. Haalaas, and O. McCarthy, " A 20-W Stereo Class-D Audio Output Power Stage in 0.6-um BCDMOS Technology," *Solid-State Circuits*, *IEEE Journal of,* vol. 39 no. 11, pp. 1948-1958, Nov. 2004.

[2.5]   Y. H. Lam, W. H. Ki, and C. Y. Tsui, "Integrated Low-Loss CMOS Active Rectifier for Wirelessly Powered Device," *Circuits and Systems II: Express Briefs, IEEE Transactions on*, vol. 59, no. 12, pp. 1378-1382, Dec. 2006.

[2.6]   S. Guo, H. Lee, "An efficiency-enhanced CMOS rectifier with unbalanced-biased comparators for transcutaneous-powered high current implants," *Solid-State Circuits, IEEE Journal of*, vol. 44, pp. 1796-1804, May 2009.

[2.7]   G. Bawa, M. Ghovanloo, "Active high power conversion efficiency rectifier with built-in dual-mode back telemetry in standard CMOS technology," IEEE Transactions on Biomedical Circuits and Systems, vol. 2, pp. 184-192, Oct. 2008.

[2.8]   H-M. Lee, M. Ghovanloo, "Fully integrated power-efficient AC-to-DC converter design in inductively-powered biomedical applications," Custom Integrated circuits Conference, pp. 1-8, Sept. 2011

[2.9]   H-M. Lee, M. Ghovanloo, "An integrated power-efficient active rectifier with offset-controlled high speed comparators for inductively powered applications," IEEE Transactions on Circuits and System I, vol. 58, pp. 1749-1760, Jan. 2011.

[2.10] S. Atluri, M. Ghovanloo, "Incorporating back telemetry in a full-wave CMOS rectifier for RFID and biomedical applications," IEEE International Symposium on Circuits and Systems, pp. 801-804, June 2007.

[2.11] H-K. Cha, W-T. Park, M. Je, "A CMOS rectifier with a cross-coupled latched comparator for wireless power transfer in biomedical applications," IEEE Transactions on Circuits and Systems II," vol. 59, pp. 409-413, May 2012.

[2.12] H. Park, et al,. "A Design of a Wireless Power Receiving Unit with a High Efficiency 6.78-MHz Active Rectifier using Shared DLLs for Magnetic Resonant A4WP Applications," *Power Electron., IEEE Transactions on*, vol .31, no. 6, pp. 4484-4498, Jun. 2016.

[2.13] X. Li, C. Y. Tsui, and W. H. Ki, "A 13.56 MHz Wireless Power Transfer System with Reconfigurable Resonant Regulating Rectifier and Wireless Power Control for Implantable Medical Devices," *Solid-State Circuits*, *IEEE Journal of,* vol. 50 no. 4, pp. 978-989, Apr. 2015.

[2.14] H. Lee, S. R. Ryu, "An efficiency-enhanced DCM regulator with improved switching timing of power transistors," *Circuit and System II: Express Briefs, IEEE Transactions on*, vol. 57, no. 3 pp. 238-242, Mar. 2010.

[2.15] S. K. Manohar, P. T. Balsara, "94.6% peak efficiency DCM buck converter with fast adaptive dead-time control," *European Solid-State Circuits Conference*, pp. 153-156, Sept. 2013.

[2.16] L. Cheng, Y. Liu, W-H. Ki, "A 10/30MHz fast reference-tracking buck converter with DDA-based type- III comparator," IEEE Journal of Solid-State Circuits, vol. 49, pp. 2788-2799, August 2014.

[2.17] C. F. Lee, P.K.T. Mok, "A monolithic current-mode CMOS DC-DC converter with on-chip current-sensing technique," IEEE Journal of Solid-State Circuits, vol. 39, pp. 3-14, Jan. 2004.

[2.18] M.D. Mulligan, B. Broach, T.H. Lee, "A constant-frequency method for improving light-load efficiency in synchronous buck converters," IEEE Power Electronics Letters, vol. 3, pp. 24-29, April 2005.

[2.19] C. Huang, P.K.T. Mok, "An 84.7% efficiency 100-MHz package bondwire-based fully integrated buck converter with precise DCM operation and enhanced light-load efficiency," IEEE Journal of Solid-State Circuits, vol. 48, pp. 2595-2607, August 2013.

[2.20] M. Al-Shyoukh, H. Lee, "A compact ramp-based soft-start circuit for voltage regulators," *Circuit and System II: Express Briefs, IEEE Transactions on*, vol. 56, pp. 535-539, June 2009.

[2.21] D. Ahn and S. Hong, "Wireless power transmission with self-regulated output voltage for biomedical implant," IEEE Trans. Ind. Electron., vol. 61, no. 5, pp. 2225–2235, May 2014.

[2.22] J. Hou, Q. Chen, Siu-Chung Wong, C. K. Tse, and X. Ruan, "Analysis and control of series/series-parallel compensated resonant converters for contactless power transfer," IEEE J. Emerg. Sel. Topics Power Electron., vol. 3, no. 1, pp. 124–136, Mar. 2015.

[2.23] R. Chen, C. Zheng, Z. U. Zahid, E. Faraci, W. Yu, J.-S. Lai, M. Senesky, D. Anderson, and G. Lisi, "Analysis and parameters optimization of a contactless IPT system for EV charger," in Proc. IEEE Appl. Power Electron. Conf., Mar. 2014, pp. 1654–1661.

[2.24] E. Gati and G. Kampitsis, "Variable frequency controller for inductive power transfer in dynamic conditions," IEEE Trans. Power Electron., vol. 32, no. 2, pp. 1684–1696, Feb. 2017.

[2.25] V. Vu, D. Trans, and W. choi, "Implementation of the Constant Current and Constant Voltage Charge of Inductive Power Transfer Systems With the Double-SidedLCCCompensation Topology for Electric Vehicle Battery Charge Applications," IEEE Trans. Power Electron., vol. 33, no. 9, pp. 7398–7410, Sep. 2018.

[2.26] J. Pan, A. A. Abidi, D. Rozgi´c, H. Chandrakumar, and D. Markovi´c, "An inductively-coupled wireless power-transfer system that is immune to distance and load variations," in IEEE Int. Solid-State Circuits Conf. (ISSCC) Dig. Tech. Papers, Feb. 2017, pp. 382–383.

[2.27] IEEE Standard for Safety Levels with Respect to Human Exposure to Radio Frequency Electromagnetic Fields, 3 kHz to 300 GHz, IEEE Std C95.1^{TM}, 2005.

[3.1] B. Latre, B. Braem, I. Moerman, C. Blondia, and P. Demeester, "A survey on wireless body area networks," Wireless Netw., vol. 17, no. 1, pp. 1–18, Jan. 2011.

[3.2] P. Swain, "Wireless capsule endoscopy," Gut, vol. 52, no. 4, pp. 48–50, Jun. 2003.

[3.3] G. Iddan, G. Meron, A. Glukhovsky, and P. Swain, "Wireless capsule endoscopy," Nature, vol. 405, no. 6785, p. 417, May 2000.

[3.4] A.Moglia, A. Menciassi, M. O. Schurr, and P. Dario, "Wireless capsule endoscopy: From diagnostic devices to multipurpose robotic systems," Biomed. Microdevices, vol. 9, no. 2, pp. 235–243, Apr. 2007.

[3.5] P. Swain, "The future of wireless capsule endoscopy," World J. Gastroenterol., vol. 14, no. 26, pp. 4142–4145, Jul. 2008.

[3.6] K. Na, H. Jang, S. K. Oruganti, and F. Bien, "An improved wireless power transfer system with adaptive technique for Implantable Biomedical Devices," in Proc. IEEE MTT-S IMWS-BIO, Singapore, 2013, pp. 1–3.

[3.7] A. Moglia, A. Menciassi, P. Dario, and A. Cuschieri, "Capsule endoscopy: Progress update and challenges ahead," Nat. Rev. Gastroenterol. Hepatol., vol. 6, pp. 353–362, Jun. 2009.

[3.8] R. Chávez-Santiago, I. Balasingham, and J. Bergsland, "Ultrawideband technology in medicine: A survey," J. Elect. Comput. Eng., vol. 2012, p. 9, 2012.

[3.9] K. C. Kong, J. Cha, D. Jeon, and D. I. D. Cho, "A rotational micro biopsy device for the capsule endoscope," in Proc. IEEE/RSJ Int. Conf. IROS, 2005, pp. 1839–1843.

[3.10] S. Park, K. I. Koo, S. M. Bang, J. Y. Park, S. Y. Song, and D. Cho, "A novel microactuator for microbiopsy in capsular endoscopes," J. Micromech. Microeng., vol. 18, no. 2, p. 9, Feb. 2008.

[3.11] M. Quirini, S. Scapellato, P. Valdastri, A.Menciassi, and P. Dario, "An approach to capsular endoscopy with active motion," in Proc. IEEE Ann. Int. Conf. EMBS, Lyon, France, 2007, pp. 2827–2830.

[3.12] R. Puers, R. Carta, and J. Thone, "Wireless power and data transmission strategies for next-generation capsule endoscopes," J. Micromech. Microeng., vol. 21, p. 15, May 2011.

[3.13] Y. Kaneko and S. Abe, "Technology trends of wireless power transfer systems for electric vehicle and plug-in hybrid electric vehicle," in Proc. IEEE 10th Int. Conf. PEDS, Kitakyushu, Japan, 2013, pp. 1009–1014.

[3.14] A. Kurs, A. Karalis, R. Moffatt, J. D. Joannopoulos, P. Fisher, and M. Soljacic, "Wireless power transfer via strongly coupled magnetic resonances," Science, vol. 317, pp. 83–86, Jul. 2007.

[3.15] J. Payne, K. Song, D. Kyo, S. Yang, J. Kim, Y. Park, and S. Choi, "Wireless power transmission for medical applications," in Proc. Nanosens., Biosens., Info-Tech Sens. Syst., Mar. 2009, 72910X.

[3.16] W. Wei, S. Hemour, and W. Ke, "Coupled resonance energy transfer over gigahertz frequency range using ceramic filled cavity for medical implanted sensors," IEEE Trans. Microw. Theory Tech., vol. 62, no. 4, pp. 956–964, Apr. 2014.

[3.17] T. P. Duong and J. W. Lee, "Experimental results of high-efficiency resonant coupling wireless power transfer using a variable coupling method," IEEE Microw. Wireless Compon. Lett., vol. 21, no. 8, pp. 442–444, Aug. 2011.

[3.18] A. P. Sample, D. A. Meyer, and J. R. Smith, "Analysis, experimental results, and range adaptation of magnetically coupled resonators for wireless power transfer," IEEE Trans. Ind. Electron., vol. 58, no. 2, pp. 544–554, Feb. 2011.

[3.19] H. Hoang, S. Lee, Y. Kim, Y. Choi, and F. Bien, "An adaptive technique to improve wireless power transfer for consumer electronics," IEEE Trans. Cons. Electron., vol. 58, no. 2, pp. 327–332, May 2012.

[3.20] H. Hoang and F. Bien, Maximizing efficiency of electromagnetic resonance wireless power transmission systems with adaptive circuits, wireless power transfer – Principles and engineering explorations, 2012 [Online]. Available: http://www.intechopen.com

[3.21] O. Jonah, S. V. Georgakopoulos, and M. M. Tentzeris, "Orientation insensitive power transfer by magnetic resonance for mobile devices," in Proc. IEEE WPT, Perugia, Italy, May 15–16, 2013, pp. 5–8.

[3.22] K. A. Grajski, R. Tseng, and C. Wheatley, "Loosely-coupled wireless power transfer: Physics, circuits, standards," in Proc. IEEE MTT-S IMWS, Kyoto, Japan, 2012, pp. 9–14.

[3.23] K. Kadota, "Designing wireless power supply systems," ANSYS, Inc., ANSYS Advantage, vol. 5, no. 3, pp. 38–40, 2011.

[3.24] S. Kim, J. S. Ho, L. Y. Chen, and A. S. Y. Poon, "Wireless power transfer to a cardiac implant," Appl. Phys. Lett., vol. 101, pp. 073701-1–073701-4, Aug. 2012.

[3.25] A. S. Y. Poon, "Electromagnetic field focusing for short-range wireless power transmission," in Proc. 6th IEEE Radio Wireless Week Symp., Santa Clara, CA, USA, Jan. 15–18, 2012, pp. 115–118.

[3.26] D. Balaguru, U. Bhalala, M. Haghighi, and K. Norton, "Computed tomography scan measurement of abdominal wall thickness for application of near-infrared spectroscopy probes to monitor regional oxygen saturation index of gastrointestinal and renal circulations in children," Pediatr. Crit. Care Med., vol. 12, pp. E145–E148, May 2011.

[3.27] V. De Santis, P. A. Beeckman, D. A. Lampasi, and M. Feliziani, "Assessment of human body impedance for safety requirements against contact currents for frequencies up to 110 MHz," IEEE Trans. Biomed. Eng., vol. 58, no. 2, pp. 390–396, Feb. 2011.

[3.28] "Guidelines for limiting exposure to time-varying electric, magnetic, and electromagnetic fields (up to 300 GHz)," in Health Phys.. Oberschleissheim, Germany: ICNIRP, 1998, vol. 74, pp. 494–522.

[3.29] "Guidelines for limiting exposure to time-varying electric and magnetic fields (1 Hz to 100 kHz)," in Health Phys. Oberschleissheim , Germany: ICNIRP, 2010, vol. 99, pp. 818–836.

[3.30] IEEE Standard for Safety Levels With Respect to Human Exposure to Electromagnetic Fields, 0–3 kHz, IEEE Standard C95.6, 2002.

[3.31] IEEE Standard for Safety Levels With Respect to Human Exposure to Radiofrequency Electromagnetic Fields, 3 kHz to 300 GHz, IEEE Standard C95.1, 2005.

[3.32] S. Li, and C. Chris, "Wireless power transfer for electric vehicle applications", IEEE J. Emerg. Sel. Topics Power Electron., vol. 3. No. 1, pp. 4-17, Mar. 2015.

[3.33] J. Sallan, J.L. Villa, A. Llombart, and J. F. Sanz, "Optimal design of ICPT systems applied to electric vehicle battery charge", IEEE Trans. Ind. Electron., Vol. 56, no. 6, pp. 2140–2149, Jun. 2009.

[3.34] C. Zheng, J. Lai, R. Chen, W.E. Faraci, Z.U. Zahid, B. Gu, L. Zhang, and G. Lisi, D. Anderson, "High-Efficiency Contactless Power Transfer System for Electric Vehicle Battery Charging Application", IEEE J. Emerg. Sel. Topics Power Electron., vol. 3, no. 1, pp. 65–74, Mar. 2015.

[3.35] W. Li, H. Zhao, S. Li, J. Deng, T. Jan, and C.C. Mi, "Integrated LCC compensation topology for wireless charger in electric and plug-in electric vehicles", IEEE Trans. Ind. Electron., vol. 62, no. 7, pp. 4215–4225, Jul. 2015.

[3.36] S.C. Tang, T.L.T. Lun, Z. Guo, K. Kwok, and N.J. McDannold, "Intermediate range wireless power transfer with segmented coil transmitters for implantable heart pumps", IEEE Trans. Power Electron., vol. 32, no. 5, pp. 3844–3857, May 2017.

[3.37] P. Si, A.P. Hu, S. Malpas, and D. Budgett, "A Frequency Control Method for Regulating Wireless Power to Implantable Devices", IEEE Trans. Biomed. Circuits. Syst., vol. 2, no. 1, pp. 22–29, Mar. 2008.

[3.38] K. Na, H. Jang, H. Ma, and F. Bien, "Tracking Optimal Efficiency of Magnetic Resonance Wireless Power Transfer System for Biomedical Capsule Endoscopy", IEEE Trans. Microw. Theory Tech., vol. 63, no.1, pp. 295–304, Jan. 2015.

[3.39] Y. Jang, and M.M. Jovanovic, "A contactless electrical energy transmission system for portable-telephone battery chargers", IEEE Trans. Ind. Electron., vol. 50, no. 3, pp. 520–527, Jun. 2003.

[3.40] Q. Li, and Y.C. Liang, "An Inductive Power Transfer System with High-Q Resonant Tank for Mobile Device Charging", IEEE Trans. Power Electron., vol. 30, no. 11, pp. 6203–6212, Nov. 2015.

[3.41] M. Galizzi, M. Caldara, V. Re, and A. Vitali, "A novel Qi-standard compliant full bridge wireless power charger for low power devices", in Proc., IEEE WPT, 2013, pp. 44–47, May 2013.

[3.42] G. Buja, M. Bertoluzzo, and K.N. Mude, "Design and experimentation of WPT charger for electric city car", IEEE Trans. Ind. Electron., vol. 62, no. 12, pp. 7436–7447, Dec. 2015.

[3.43] J.T. Hwang, D.S. Lee, J.H. Lee, S.M. Park, K.W. Jin, M.J. Ko, H.I. Shin, S.O. Jeon, D.H. Kim, and J. Rhee, "An all-in-one (Qi, PMA and A4WP) 2.5W fully integrated wireless battery charger IC for wearable applications", IEEE Int. Solid-State Circuits Conf. (ISSCC), pp. 378–380, Jan. 31-, Feb. 4, 2016.

[3.44] "WPC v1.2 wireless power transmitter manager with 15-W power delivery, bq501210". Available at http://www.ti.com/lit/ds/symlink/bq501210.pdf, accessed May 21th, 2018.

[3.45] X. Qu, H. Han, S. Wong, C.K. Tse, and W. Chen, "Hybrid IPT topologies with constant current or constant voltage output for battery charging applications", IEEE Trans. Power Electron., vol. 30, no. 11, pp. 6329–6337, Nov. 2015.

[3.46] R. Mai, Y. Chen, Y. Li, Y. Zhang, G. Cao, and Z. He, "Inductive Power Transfer for Massive Electric Bicycles Charging Based on Hybrid Topology Switching With a Single Inverter", IEEE Trans. Power Electron., vol. 32, no. 8, pp. 5897–5906, Aug. 2017.

[3.47] R.L. Steigerwald, "A comparison of half-bridge resonant converter topologies", IEEE Trans. Ind. Electron., vol. 3, no. 2, pp. 174-182, Apr. 1988.

[3.48] R. Chen, C. Zheng, Z.U. Zahid, E. Faraci, W. Yu, J. Lai, M. Senesky, D. Anderson, and G. Lisi, "Analysis and parameters optimization of a contactless IPT system for EV charger", Proc. IEEE Appl. Power Electron. Conf. Expo., pp. 1654–1661, Mar. 16-20, 2014.

[3.49] R. Bosshard, J.W. Kolar, and B. Wunsch, "Control method for Inductive Power Transfer with high partial-load efficiency and resonance tracking", Proc. Int. Power Electron. Conf., Hiroshima, Japan, pp. 2167–2174, May 18-21, 2014.

[3.50] D. Ahn, and S. Hong, "Wireless Power Transfer Resonance Coupling Amplification by Load-Modulation Switching Controller", IEEE Trans. Ind. Electron., vol. 62, no. 2, pp. 898–909, Feb. 2015.

[3.51] Z. Huang, S. Wong, C.K. Tse, "Design of a Single-Stage Inductive-Power-Transfer Converter for Efficient EV Battery Charging", IEEE Trans. Veh. Technol., vol. 66, no. 7, pp. 5808–5821, Jul. 2017.

[3.52] X. Li, C.Y. Tsui, W.H. Ki, "Wireless Power Transfer System Using Primary Equalizer for Coupling- and Load-Range Extension in Bio-Implant Application", IEEE Int. Solid-State Circuits Conf. (ISSCC), pp. 228–210, Feb. 22-26, 2015.

[3.53] K. Na, H. Jang, H. Ma, and F. Bien, "Tracking optimal efficiency of magnetic resonance wireless power transfer system for biomedical capsule endoscopy," *IEEE Trans. Microw. Theory Techn.*, vol. 63, no. 1, pp. 295-304, Jan. 2015.

[3.54] J. Hao Cheong, S. S. Y. Ng, X. Liu, R.-F. Xue, H. J. Lim, P. B. Khannur, K. L. Chan, A. A. Lee, K. Kang, L. S. Lim, C. He, P. Singh, W.-T. Park, and M. Je, "An Inductively Powered Implantable Blood Flow Sensor Microsystem for Vascular Grafts," *Biomedical Engineering, IEEE Transactions on*, vol. 59, no. 9, pp. 2466–2475, Sep. 2012.

[3.55] R.-F. Xue, K.-W. Cheng, and M. Je, "High-efficiency wireless power transfer for biomedical implants by optimal resonant load transformation," *IEEE Trans. Circuits Syst. I, Reg. Papers*, vol. 60, no. 4, pp. 867-874, Apr. 2013.

[3.56] [online] Available: http://www.wirelesspowerconsortium.com/.

[3.57] S.-Y. Park, J. Cho, K. Lee, and E. Yoon, "A PWM buck converter with load-adaptive power transistor scaling scheme using analog-digital hybrid control for high energy efficiency in implantable biomedical systems," *IEEE Trans. Biomed. Circuits Syst.*, vol. 9, no. 6, pp. 885–895, Dec. 2015.

[3.58] O. Al-Terkawi Hasib, M. Sawan, and Y. Savaria, "A low-power asynchronous step-down DC-DC converter for implantable devices," *IEEE Trans. Biomed. Circuits Syst.*, vol. 5, no. 3, pp. 292–301, Jun. 2011.

[3.59] T. Huang, C. Hsieh, Y. Yang, et al., "A Battery-Free 217 nW Static Control Power Buck Converter for Wireless RF Energy Harvesting With -Calibrated Dynamic On/Off Time and Adaptive Phase Lead Control," *IEEE J. of Solid-State Circuits.*, vol. 47, no. 4, pp. 852-862, Apr. 2012.

[3.60] H. Lee and S.-R. Ryu, "An efficiency-enhanced DCM buck regulator with improved switching timing of power transistors," *IEEE Trans. Circuits Syst. II, Exp. Briefs*, vol. 57, no. 3, pp. 238–242, Mar. 2010.

[3.61] B. S. Cherkauer and E. G. Friedman, "A unified design methodology for CMOS tapered buffers," *IEEE Trans. Very Large Scale Integr. (VLSI) Syst.*, vol. 3, no. 1, pp. 99–111, Mar. 1995.

[3.62] J. Doutreloigne, H. De Smet, and A. Van Calster, "A versatile microp- ower high-voltage flat-panel display driver in a 100-V 0.7-   m CMOS intelligent interface technology," *IEEE J. Solid-State Circuits*, vol. 36, no. 12, pp. 2039–2048, Dec. 2001.

[3.63] V. Vorperian, "Simplified analysis of PWM converters using the model of the PWM switch: Part II—Discontinuous conduction mode," *IEEE Trans. Aerosp. Electron. Syst.*, vol. 26, pp. 497–505, May 1990.

[4.1]   B. Razavi, *RF Microelectronics.* 2nd ed., Pearson, 2012, pp. 62–65.

[4.2]   S.-Y. Lee, C.-H. Hsieh, and C.-M. Yang, "Wireless front-end with power management for an implantable cardiac microstimulator," IEEE Trans. Biomed. Circuits Syst., vol. 6, no. 1, pp. 28–38, Feb. 2012.

[4.3]   J. H. Cheong, S. S. Y. Ng, X. Liu, R.-F. Xue, H. J. Lim, P. B. Khannur, K. L. Chan, A. A. Lee, K. Kang, L. S. Lim, C. He, P. Singh, W.-T. Park, and M. Je, "An inductively powered implantable blood flow sensor microsystem for vascular grafts," IEEE Trans. Biomed. Eng., vol. 59, no. 9, pp. 2466–2475, Sep. 2012.

[4.4]   R.-F. Xue, K.-W. Cheng, and M. Je, "High-efficiency wireless power transfer for biomedical implants by optimal resonant load transformation," IEEE Trans. Circuits and Systems I, vol. 63, no. 1, pp.295-304, Jan. 2015.

[4.5]   S. Guo, and H. Lee, "An Efficiency-Enhanced CMOS Rectifier with Unbalanced-Biased Comparators for Transcutaneous-Powered High-Current Implants", IEEE Journal of Solid-State Circuits, vol. 44, no. 6, June 2009.

[4.6]   H-K. Cha, W-T. Park, and M. Je, "A CMOS Rectifier with a Cross-Coupled Latched Comparator for Wireless Power Transfer in Biomedical Applications", IEEE Transactions on Circuits and System II, Vol. 59, no. 7, July 2012.

[4.7]   Y. Lu, W-H. Ki, and J. Yi, "A 13.56MHz CMOS Rectifier with Switched-Offset for Reversion Current Control", Symposium VLSI circuits design of technical papers.

[4.8]   H. Lee, and M. Ghovanloo, "An Integrated Power-Efficient Active Rectifier with Offset-Controlled High Speed Comparators for Inductively Powered Applications", IEEE Transactions on Circuits and Systems I, Vol. 58, No. 8, August 2011.

[4.9]   C-Y. Wu, X. Qian, M. Cheng, Y. Liang, and W. Chen, "A 13.56 MHz 40 mW CMOS High-Efficiency Inductive Link Power Supply Utilizing On-Chip Delay-Compensated Voltage Doubler Rectifier and Multiple LDOs for Implantable Medical Devices", IEEE Journal of Solid-State Circuits, Vol.49, No. 11, November 2014.

[4.10]   X. Li, et al., "Wireless Power Transfer System Using Primary Equalizer for Coupling- and Load-Range Extension in Bio-Implant Application," ISSCC Dig. Tech. Papers, pp. 228-229, Feb. 2015.

[4.11]   Z. Liu and H. Lee, "A 100V gate driver with sub-nanosecond-delay capacitive-coupled level shifting and dynamic timing control for ZVS-based synchronous power converters," in Proc. IEEE Custom Integrated Circuit Conf., pp. 1-4, Sep. 2013.

[4.12]   J. Doutreloigne, et al., A Versatile Micropower High-Voltage Flat Panel Display Driver in a 100-V 0.7-um CMOS Intelligent Interface Technology." IEEE J. Solid-State Circuits, vol. 36, no. 12, pp. 2039-2048, Dec. 2001.

[4.13]   R. Redl, and J. Sun, "Ripple-based control of switching regulators – an overview", IEEE Trans. Power Electron., vol. 1, no. 3, pp. 2669–2680, Sep. 2009.

[4.14] M. Lee, J. Yang, M. J. Park, S. Y. Jung, and J. Kim, "Design and analysis of energy-efficient single-pulse piezoelectric energy harvester and power management IC for battery-free wireless remote switch applications," IEEE Trans. Circuits Syst. I, Reg. Papers, vol. 65, no. 1, pp. 366–378, Jan. 2018.

[4.15] S. Bandyopadhyay, et al., "20uA to 100 mA DC-DC Converter With 2.8-4.2 V Battery Supply for Portable Applications in 45nm CMOS," IEEE J. Solid-State Circuits, vol. 46, no. 12, pp. 2807-2820, Dec. 2011.

[4.16] B. Sahu, et al., "An Accurate, Low-Voltage, CMOS Switching Power Supply With Adaptive On-Time Pulse-Frequency Modulation (PFM) Control." IEEE Trans. Circuits Syst. I, vol. 54, no. 2, pp. 312-321, Feb. 2007.

[4.17] SangYun Kim et al., "A design of a high efficiency DC-DC buck converter with two-step digital PWM and low power self-tracking zero current detector for IoT applications," IEEE Trans. Power Electron., vol.33, no.2, pp. 1428-1439, Feb. 2018.

Acknowledgement

I would like to express my special appreciation and thanks to my advisor, Prof. Franklin Bien for the continuous support of my research, for his patience, motivation, encouragement, and advisement. I would never have been able to finish my doctoral thesis without his help and guidance.

Besides my advisor, I would like to thank the rest of my thesis committee: Prof. Jaehyouk Choi, Prof. Katherine Kim, Prof. Kyuho Lee, and Prof. Ockgoo Lee, for their insightful comments and encouragement, but also for the hard question which incented me to widen my research from various perspectives.

I would like to thank my fellow lab mates for their continued support. This thesis would not have been possible without the contribution of WPT team members. And, I am thankful to WPT team members and TSP team members in for the stimulating discussions, for the sleepless nights we were working together before deadlines, and for all the fun we had in the last six years. I would also like to thank my other lab mates for making my experience in BICDL exciting and fun.

I would like to thank my family: my parents, my parents-in-laws, and my younger brother for supporting me spiritually throughout writing this thesis and my life in general.

Last but not least, I would like to express my deepest gratitude to my beloved wife for her patience, support, and encouragement.

Curriculum Vitae

Personal Information

Name: Hyunggun Ma (마형근, 馬亨根)

E-mail: hackerd1213@gmail.com

Education

2013.3 – 2019.2 Combined M.S. - Ph.D. in School of Electrical & Computer Engineering
Ulsan National Institute of Science and Technology
Major: Analog circuit design
Thesis Title: Wireless Power Transfer System for Battery-Less Body Implantable Devices
Advisor: Prof. Franklin Bien

2006.3 – 2013.2 B.S. in Department of Electronic Engineering
Gyeongsang National University, Jinju, South Korea

Journal Publications

[1] **H. Ma**, G. Namgoong, E. Choi, and F. Bien, "Instantaneous Power Consuming Level Shifter for Improving Power Conversion Efficiency of Buck Converter", IEEE Transactions on Circuits and Systems II: Express Briefs (T-CAS II), Accepted on Oct. 27th 2018.

[2] **H. Ma*,** K. Na*, G. Namgoong, K. A. Kim, J-H. Jung, and F. Bien, "Step-charging technique for CC/CV mode battery charging with low-cost control components in IPT systems", IET Power Electronics, Accepted on Oct. 4th 2018 - **co-1st Author.**

[3] **H. Ma**, G. H. Nam-Goong, S. Kim, S-I. Lim, and F. Bien, "Differential Difference Amplifier based Parametric Measurement Unit with Digital Calibration", Journal of Semiconductor Technology and Science, Vol. 18, No. 4, pp. 438-444, Aug. 2018.

[4] **H. Ma**, Z. Liu, S. Heo, J. Lee, K. Na, H.B. Jin, S. Jung, K. Park, J.J. Kim, and F. Bien, "On-Display Transparent Half-Diamond Pattern Capacitive Fingerprint Sensor Compatible with AMOLED Display", IEEE Sensors Journal, vol. 16, no. 22, pp. 8124 – 8131, Sep. 2016.

[5] **H. Ma**, S. Heo, J. J. Kim, and F. Bien, "Algorithm for improving SNR using high voltage and differential Manchester code for capacitive touch screen panel," IET Electronics Letters, vol. 50, no. 24, pp. 1813–1815, Nov. 2014.

[6] S. Heo, **H. Ma**, J. Song, K. Park, E. Choi, J. J. Kim, and F. Bien, "72 dB SNR, 240 Hz Frame

Rate Readout IC with Differential Continuous-mode Parallel Architecture for Larger Touch-Screen Panel Applications", IEEE Transactions on Circuits and Systems I: Regular papers (T-CAS I), vol. 63, no. 7, pp. 960 - 971, Jun. 2016.

[7] S. Heo, **H. Ma**, F. Bien, "An excessive current subtraction technique to improve dynamic range for touch screen panel applications", Journal of Semiconductor Technology and Science, vol. 16, no. 3, pp. 375-379, Jul. 2016.

[8] K. Na, **H. Ma**, J. Park, J. Yeo, and F. Bien, "Graphene-Based Wireless Environmental Gas Sensor on PET Substrate," IEEE Sensors Journal, vol. 16, no. 12, pp. 5003 - 5009, Feb. 2016.

[9] K. Na, H. Jang, **H. Ma**, Y. Choi, and F. Bien, "A 200 Mbps Data Rate 3.1-4.8 GHz IR-UWB All-Digital Pulse Generator with DB-BPSK Modulation," IEEE Transaction on Circuit and System: Express Briefs (T-CAS) II, vol. 62, no. 12, pp. 1184 - 1188, Aug. 2015.

[10] S. Oruganti, S. Heo, **H. Ma**, and F. Bien "Wireless energy transfer: touch/hover sensing for large, contoured display and robotic fingers," IEEE Sensors Journal, vol. 15, no. 4, pp.2062-2068, Apr. 2015.

[11] K. Na, H. Jang, **H. Ma**, and F. Bien, "Tracking Optimal Efficiency of Magnetic Resonance Wireless Power Transfer System for Biomedical Capsule Endoscopy", IEEE Transactions on Microwave Theory and Techniques, vol. 63, no. 1, pp.295-304, Jan. 2015.

[12] S.K. Oruganti, S. Heo, **H. Ma,** and F. Bien, "Wireless energy transfer based transceiver systems for power and/or high-data rate transmission through thick metal walls using sheet-like wave-guides", IET Electronics Letters, vo. 50, no. 12, p.886-888, Jun. 2014.

Conference Proceedings

[1] **H. Ma**, J. Lee, W. Seo and F. Bien, "Reduced Detection Time with High Dynamic Range Using Digitally Current Subtraction Technique for Touch Screen Panel", International Conference on Electronics, Information and Communication (ICEIC), Jan. 15 - Jan. 18, 2014, Kota Kinabalu, Malaysia.

[2] S. Heo, **H. Ma**, J. Song, K. Park, E. Choi, and F. Bien, "A 200 atto farad capacitance sensing with a differential signaling method for a mutual capacitive fingerprint sensor", IEEE International Conference on Consumer Electronics-Asia, Oct. 26 - Oct. 28, 2016, Seoul, Korea.

[3] H. Jang, **H. Ma**, K. Na, and F. Bien, "A Stent based Biomedical Wireless Communication Platform for In-Vivo Glucose Sensing System", 2015 IEEE International Microwave Workshop Series on RF and Wireless Technologies for Biomedical and Healthcare Applications (IMWS-bio), Sep. 21-23, 2015, Taipei, Taiwan.

[4] H. Jang, **H. Ma**, D. Seo, J. Lee, H. Lee, and F. Bien, "Low Power Receiver for Medical Implantable Communication System using Delay Locked Loop", 2014 IEEE IMWS-bio, December 8-10, 2014, London, United Kingdom.

[5] S. Heo, **H. Ma**, J. J. Kim, and F. Bien, "Highly Improved SNR Differential Sensing Method using Parallel Operation Signaling for Touch Screen Application", 2014 IEEE Asian Solid-State Circuits Conference (A-SSCC), Nov. 10-12, 2014, Kaohsiung, Taiwan.

[6] S. Heo, **H. Ma**, J. J. Kim, and F. Bien, "Dynamic range enhanced readout circuit for a capacitive touch screen panel with current subtraction technique", 2014 European Solid-State Circuits Conference(ESSCIRC).

Patents

[1] 변영재, 오루간티사이 키란, 허상현, 마형근, 서석태, "무선전력전송 시스템 및 통신 시스템," 10-1810737, Dec. 13, 2017.

[2] 변영재, 김슬기롬, 마형근, "온도 보상을 구비한 차량용 이더넷 통신 이퀄라이저 및 그 제어 방법", 10-1706585, Feb. 8, 2017.

[3] J. Kwon, F. Bien, J. J. Kim, H. Ma, S. Heo, "Touch Sensor and Display Device Including the Same", U.S. Patent, US9563306B2, Feb. 7, 2017..

[4] 변영재, 김재준, 허상현, 마형근, 이지윤, 장희돈, "생체 인식 보안 장치 및 이를 이용한 지문 인식 데이터 관리 방법", 10-1645025, Jan. 27, 2016..

[5] 변영재, 허상현, 마형근, "터치스크린의 병렬 방식 리드아웃 장치", KR101450271B1, Oct. 22, 2014.